An Experimental Study of Pressure- and Electroosmotically-Driven Flows in Microchannels with Surface Modifications

By

Chee Leong Lum

A Dissertation

Submitted to
Michigan State University
in partial fulfillment of the requirements
for the degree of

Doctor of Philosophy

Department of Mechanical Engineering

2005

Abstract

An Experimental Study of Pressure- and Electroosmotically-Driven Flows in Microchannels with Surface Modifications

By

Chee Leong Lum

Researchers investigating pressure-driven flows within microchannels have reported a discrepancy with classical theory. These discrepancies were attributed to various reasons; notably entrance effects, electroviscous effects, early transition to turbulence, surface roughness effects, etc. These measurements were all performed using bulk flow measurement techniques such as pressure drop and flow rate measurements. To investigate if deviations from classical theory do exist, the friction factor obtained from the current study was compared to classical theory for microchannels with a characteristic size of 300μm. The determination of the friction factor in this study differs from other researchers as it is derived from local measurements of the velocity profile using the Molecular Tagging Velocimetry (MTV) technique. This is the first time that a local measurement of the velocity profile has been used to derive the friction factor. Local measurements are advantageous as entrance effects do not affect it and it does not suffer from the high order dependence on diameter (D^4) when relating pressure drop to volume flow rate. The microchannels used in this study were coated with polymer brushes (HEMA) and octadecyl-trichlorosilane (OTS) to investigate if the added hydrophobicity of these coatings would affect the pressure-driven flow.

The second part of this study relates to electroosmotically-driven flows within microchannels. Electroosmotically-driven flows are of interest as pressure-driven flows

become increasingly ineffective in transporting fluid due to the increase in surface to volume ratios in smaller microchannels. The electroosmotic velocity's dependence on temperature and the applied electric potential was studied using a simultaneous velocity and temperature measurement technique (Molecular Tagging Velocimetry & Thermometry, MTV&T). The estimation of the electroosmotic velocity based only on the Helmholtz-Smoluchowski equation was found to be inadequate due to the presence of Joule heating and showcases the need for a simultaneous local measurement of both the velocity and temperature to resolve the flow physics. This local measurement technique is also used to obtain local zeta potential (ζ) measurements of the different surfaces. Zeta potential information is important in designing microfluidic devices to improve mixing characteristics within microchannels. An added capability of the measurement technique to reveal zeta potential dependence on temperature is also presented. To further our understanding of the spatio-temporal evolution of temperature within the microchannel during electroosmosis, a numerical simulation (FLUENT) was employed with boundary conditions similar to our experimental studies.

Dedication

This thesis is dedicated to my parents for all the love and support throughout the years, without which I would not have come so far in my education. I am also eternally grateful to my fiancé for being by my side throughout this journey which made it more bearable at times of difficulties.

Acknowledgements

This work would not have been possible without the help and support of many people. I would first like to thank my primary advisor Dr. Manoochehr Koochesfahani for the excellent guidance that culminated in the work done in this thesis. Throughout the years, it has been a privilege to work under his tutelage. I am also grateful for the kind advice from my other thesis committee members; Dr. Ahmed Naguib, Dr. Merlin Bruening and Dr. Andre Benard. Their help have been instrumental in the completion of this thesis.

I would also like to thank my colleagues for all the assistance and discussions that helped in the work presented in this thesis. I would like to specifically thank Doug Bohl (for the help and guidance when I first came in as a Masters student), Behshad Shafii (for the stimulating discussions on our projects and creating a lively environment in the lab), Laura Hudy (for being there as a friend, basketball and football fan, phD student, all rolled into one), Shahram Pouya (for his dependability and inherent strive for perfection) and Jill Drexler (for her endless enthusiasm and hours of conversation which kept boredom away).

This work would also not have been possible without support from the National Science Foundation (NSF), the Center for Sensor Materials at Michigan State University (Ann Kirchmeier, Darla Conley and Keri Marchand were amazingly helpful) and Mike McClean for his help in creating the experimental setups in this work.

Table of Contents

List of Tables

List of Figures

(Images in this dissertation are presented in color)

Nomenclature

Symbol	Description
a	half width (Y-axis)
A	cross sectional area
b	half width (Z-axis)
c	concentration of ions
C_f	friction factor (Fanning)
$C_{f,exp}$	experimental friction factor (Fanning)
$C_{f,theory}$	theoretical friction factor (Fanning)
C_o	charge distribution
D	Diameter
D	diffusion coefficient
D_H	Hydraulic diameter
Du	Dukhin number
E_x	applied electric potential per unit length
f	friction factor (Darcy)
F	Faraday's constant
g	gravity
I	current
I_{em}	emitted intensity
I_o	Initial intensity
I_p	total phosphorescence signal
J	Joules
K^L	bulk conductivity
K^σ	surface conductivity
l	characteristic length (m)
L	Liter
p	pressure
P	power
Q	volume flow rate
q	heating rate
R	Radius
R	gas constant
Re	Reynolds Number
Re_{CH}	Reynolds Number based on Characteristic Height
Re_{DH}	Reynolds Number based on Hydraulic Diameter
RPE	relative perturbation error
R_{th}	theoretical velocity ratio

S	circumference
t	time
T	temperature
T_f	final temperature
T_o	initial temperature
$\overline{u}$	sectional mean velocity
$\overline{u}_{theory}$	Sectional mean velocity (theory)
$\overline{U}$	microchannel mean velocity
u_{max}	peak velocity
u_r	radial velocity
u_x	axial velocity
u_y	velocity in the Y-axis
u_z	velocity in the Z-axis
u_θ	azimuthal velocity
V	voltage
V_f	final velocity
V_o	initial velocity
W	electric potential energy per mole of counter ions
z_i	charge number
β	slip length
Δp	pressure differential
Δt	delay time
ε	roughness (standard deviation)
ε	permittivity
ε_o	permittivity of vacuum
ε_r	relative permittivity
Z	zeta potential
Θ	angle
λ_D	Debye length
μ	dynamic viscosity
P	density
ρ_E	electric charge density
T	lifetime
τ_{dl}	double layer response time
τ_{eo}	electroosmotic response time
τ_{xy}	shear stress (X-Y)
τ_{yz}	shear stress (Y-Z)
τ_{zx}	shear stress (Z-X)
Φ_w	wall potential

Ω	Line thickness
ω_o	Initial line thickness

Chapter 1 Introduction

For many years, researchers involved in the engineering field were focused on the macro scale as most applications that demanded our attention were macro in size. The need for a wind tunnel to better simulate real world conditions, for example, eventually led to the creation of an 80x120 feet wind tunnel at NASA Ames. Other instances of similar use of macro-sized test facilities can be observed. Biologists and chemists, on the other hand, are mainly interested in cell structures, chemical reactions and the like, which operate at micro or even nano-scales. In recent years, however, miniaturization has become more important for engineers in efforts to build smaller devices that have a smaller footprint with similar or better characteristics compared to their macro-sized counterpart. Miniaturization holds many promises but as yet not fully realized as our understanding of the flow physics within micro scale structures are not fully developed. One of the obvious advantages of miniaturization is size. Smaller sized pumps, engines, chemical detectors, etc. utilize space constraints more efficiently. A miniaturized chemical detector, for example, could in theory be fitted on a wrist watch and help warn the user of chemical exposure. Costs could also be significantly reduced as the use of material decreases. The miniaturization of a heat transfer device increases the surface to volume ratio available for heat transfer thus improving the performance of cooling and heating mechanisms. A cooling performance increase in a small package would benefit the cooling requirements of a personal computer, for example. These advantages and many more have created a need to fully understand the physical implications of miniaturization.

Coinciding with this need, this study specifically investigates methodologies currently used to move fluids within microchannels through experimental study and comparing with known theories. Biologists and chemists have traditionally used pressure driven flows within capillaries for analyte separation analyses. Pressure driven

flows, however, cause the separated analytes to spatially spread out or broaden as they are advected downstream of the capillary for detection due to the presence of shear. Band broadening of the separated analytes causes a reduced detection sensitivity. Electroosmotically driven flows (EOF), conversely, do not cause band broadening due to the uniform flow characteristics across the entire capillary. The surface charge present on most surfaces, coupled with an ionized fluid (e.g. aqueous solutions of an electrolyte) within the capillary and an electric field applied parallel to the surface causes EOF to occur. This technique is essential in capillary electrochromatography (CEC). CEC combines the advantage of chromatography (separating uncharged analytes possessing different adsorption characteristics), and separation of charged analytes through electrophoresis (variation in analyte velocity due to charge differences).

As much as pressure driven flows and EOF have been utilized in biochemistry and engineering, certain issues related to the flow transport within micro- and nano-sized channels need to resolved. Researchers over the years have compiled a large amount of data that showed inconsistencies between experimental results and theory for pressure driven flows within microchannels. A representative data set for friction factor was presented by Sharp et. al. (2002) and replotted in Figure 1-1. Agreement with theory requires that the data in Figure 1-1 have a normalized friction constant of unity. All the data sets showed large variations from theory except data from Sharp et. al. (2000). These anomalies were attributed to surface roughness effects, electroviscous effects, micro-rotational effects of individual fluid molecules, early transition to turbulence, entrance effects, non-local flow measurement techniques and inaccuracies in measuring channel dimensions. Coincidentally, the data sets that showed variations from theory were all acquired with bulk flow measurements like measurement of flow rates and pressure drops. Data from Sharp et. al. (2000) were acquired using a combination of pressure drop measurements and a local measurement technique called Particle Image Velocimetry (PIV) and showed agreement with theory (Reynolds number, Re: 100-2000). Transition to turbulence was observed at Reynolds number (Re) ~ 2000

which is consistent with general flow theory. PIV is a measurement technique that uses particles to track flow movement but care is needed to ensure that the particles used do not interfere with the flow and that flocculation (coalescing of particles) does not occur. Above all, it is important that the particles used for flow tracking do indeed follow the flow field faithfully. Density mismatch with the working fluid or the interaction of the charged surfaces of the particles with the microchannel could cause errors in the measurements.

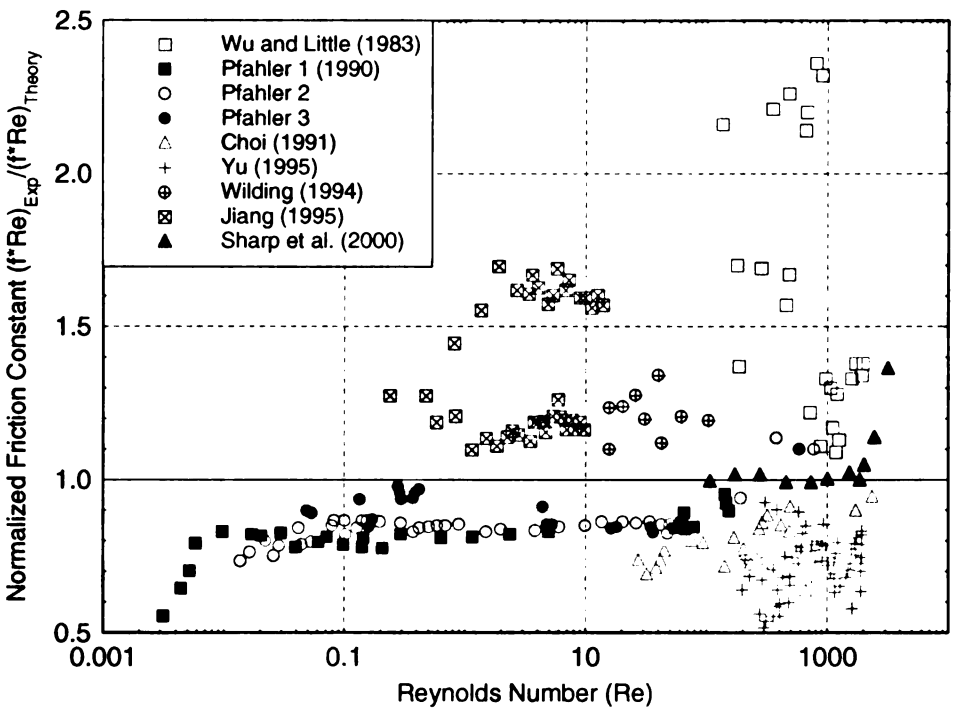

Figure 1-1. Normalized friction constant plot with data from various researchers. (Sharp et. al, 2002)

More recently, Brutin et. al. (2003), through pressure drop measurements, suggested that the observed deviations from classical theory for round glass capillaries (as large as 530μm) in their experiments are due to the fluid's ionic composition and its interaction with the charged microchannel wall to cause an added viscosity near the wall. This phenomenon is called electroviscous effects and is known to only affect the

flow field when the electric double layer (EDL) is comparable in height to the microchannel dimensions (Rice and Whitehead, 1965). This phenomenon will cause an added viscosity-like effect on the bulk flow, thus causing a deviation from classical theory. Phares and Smedley (2004), however, stipulated that electroviscous effects do not affect the flow field for smooth capillaries >100μm in diameter. As the channel size decreases (<50μm), the inconsistencies with theory become more pronounced. Their measurement range was from a Re of 0.0001-1. Other causes of discrepancies with classical theory have also been attributed to surface roughness. Phares and Smedley (2004) measured deviations of up to 17% from classical theory for rough tubes (roughness values (ε/D, roughness in relative to diameter) of 2% were observed). The tubings that were used were made of stainless steel and the roughness characteristics were noticeably higher than that of glass capillaries.

In any experiment, the appropriate use of experimental techniques plays a very important role in determining its effectiveness. Pressure drop and volume flow rate measurements are suitable in providing bulk or averaged flow information across the entire flow setup but entrance effects need to be decoupled from the measurement. An local measurement technique is thus needed to resolve unambiguously the flow physics within microchannels.

In this study, an in-situ technique is utilized to determine the velocity and estimate the wall friction factor. Molecular Tagging Velocimetry (MTV) is a local measurement technique similar in implementation to PIV but uses "tagged" molecules instead of particles to track the flow. The utilization of molecules ensures that some of the constraints (particle density, flocculation, etc.) related to the use of PIV are not present in MTV. A more detailed discussion of the MTV technique is presented in § 2.5. Previous work by Maynes et. al. (2002) used the MTV technique to provide mean flow characteristics within a 0.705 mm circular tube but did not utilize the velocity profiles to derive friction factor information as is being done in this study. For each set of experimental conditions, the velocity profile, the pressure drop and the mass flow rate

were quantified. The velocity profile was measured using the MTV technique but only the mean velocity information was derived from it. Volume flow rate, however, was measured by collecting the fluid at the channel exit over a period of time. The two measurements were compared to determine any discrepancies from theory. These experiments were performed over a Reynolds number range of 500-2500 and the friction factor derived from pressure drop measurements showed agreement with the standard friction factor definition of f=64/Re for a Poiseuille flow in round capillaries. It is intended in the current study to improve upon the measurements made by Maynes et. al. (2002) by focusing on smaller channel sizes (300um) where a deviation from theory (if any) is more likely, lower Reynolds numbers (1-100) and a higher measurement resolution. Also, the friction factor will be derived from in-situ measurements of the velocity profile and not bulk flow measurements as in the case of Maynes et. al (2002) and Sharp et. al. (2000). This is expected to provide higher accuracy measurements as ambiguities like entrance length issues which are related to bulk flow measurement techniques are not present.

Maynes et. al. (2002), Sharp, et. al (2000) and our own experiments to date were all performed using water as the flowing medium but it is worth noting that some of the data from Figure 1.1 was obtained using non-polar fluids. Non-polar fluids like silicon oil and kerosene, for example, do not contain ions and their interactions with surfaces are different from ionic fluids. The difference in molecular forces present in each material or fluid causes surface tension when two different materials come in contact (Adamson, et. al. 1997). An example of surface tension is illustrated in the beading of water droplets into spheres to reduce the surface area exposed to air. Non-polar fluids have a lower surface tension caused by the absence of ions and any purported interaction of ions between the fluid and the microchannel as a source of discrepancy in friction factor (Ren et. al (2001) and Brutin et. al. (2003)) will be a non-issue in this case. Nevertheless, experimental results from Pfahler et. al. (1990) with N-propanol and silicone oil as the flowing medium still showed a consistent deviation from theory which

could be due to other unknown factors or simply an error in measurement. The discrepancies in the literature clearly indicate that there is a need to resolve some of these issues.

Another prevalent issue in fluid flow in microchannels is the possibility of slip. The typical no-slip boundary condition, whereby the fluid flow decelerates to zero velocity at a solid boundary, holds for macro scales as the shear stress is considerably lower than that present within microchannels. Navier, in 1823 proposed a slip boundary condition with the slip velocity proportional to the velocity gradient at a surface and a proportionality constant, β, as the slip length.

$$U = \beta \frac{\partial u}{\partial y} \qquad 1\text{-}1$$

To date, molecular dynamics simulations (Jabbarzadeh, et. al. (1999)) and experiments (Pit et. al. (2000) and Trethaway, et. al. (2002)) have been performed to estimate the slip length with varying results. Slip lengths on the order of nanometers to 1 micron have been reported on treated microchannels. Microchannels are typically treated with octadecyl-trichlorosilane (OTS) to render the channel surface hydrophobic (hydrophobicity is a tendency for a surface to repel water, hence the term *hydro*). An increased hydrophobicity will typically increase slip lengths. Shear stress measurements by itself do not reveal any information about slip as it is not affected by its presence. However, the normalization of the shear stress to obtain friction factor utilizes the mean velocity which increases with the presence of slip. The equations of motion with slip velocity are derived in Appendix L.

Experimental techniques used to measure slip typically measure the increased flow rate within a treated microchannel or zoom in on the solid-liquid interface to locally measure the slip length. The use of bulk flow measuring techniques is usually plagued with uncertainties as it is difficult to attribute a measured increase in flow rate to be

due to the presence of slip alone. An increased flow rate could potentially be caused by a change in channel size, an error in pressure drop measurements, etc. A local measurement of the slip length on the other hand, although appealing since it removes any ambiguities associated with bulk flow measurements, is very difficult since it requires a high resolution measurement technique.

As the dimensions of our flow device become smaller, pressure becomes less effective in moving fluids. The following expression, showing the relation between Δp and Q, illustrates this for flow within capillaries.

$$\Delta p = \frac{128 \mu l Q}{\pi D^4} \qquad 1\text{-}2$$

where Δp is the pressure drop required, μ is the dynamic viscosity, Q is the volume flow rate and, l and D is the length and diameter of the flow device respectively. The pressure drop scales inversely with the 4th power of diameter. As the flow device diameter becomes smaller, the pressure drop needed to move fluid within microchannels becomes very large. For example, a 10X reduction in diameter requires a 10,000X higher pressure drop to maintain the same volume flow rate. Conversely, EOF is an elegant way of transporting fluid within microchannels without the need for high pressure. A byproduct of EOF, however, is heat generation through Joule heating. Excessive heat generation can affect electroosmotic flow and cause problems with analysis of separated analytes. To better comprehend the effects of Joule heating, temperature measurements within the microchannels would be useful. Ross et. al. (2001) managed to measure whole field temperature distributions within acrylic microchannels using a temperature dependent emission of a fluorescent dye. The precision with which the measurements were made were low and the technique did not take into account the spatial inhomogeneity of the excitation laser nor curvature of the microchannel. Thomson et. al. (2001), conversely, used a phosphorescent dye whereby

the emission intensity of the dye alone is used to infer the temperature. An improvement to the techniques used by Thomson et. al. (2001) and Ross et. al. (2001), as documented in Hu et. al. (2003), will be used for the first time to measure temperature and velocity simultaneously within microchannels in EOF. The characterization of both temperature and velocity simultaneously will allow us to draw a direct consequence of temperature change to velocity change due to physical changes of the fluid properties. A temperature gradient that develops along the length of the microchannel as electroosmosis occurs may cause additional errors in measurement of the electroosmotic velocity for bulk flow measurements.

Another aspect of interest in EOF is the determination of the zeta potential of a surface. Oftentimes, a surface is coated to change its charge characteristics (to prevent flocculation of particles, for example). The interaction of the surface coating with the fluid is not directly known and measurements of the zeta potential of the surface need to be made. The zeta potential is a characteristic observed from the combination of the interaction of the surface charge and the fluid characteristics within the channel and is one of the factors that affect electroosmotic velocity. A typical method for determining the zeta potential of a microchannel is to observe the movement of a neutral particle during electroosmosis. The Helmholtz-Smoluchowski equation is then used to calculate the zeta potential from a measured electroosmotic velocity. The use of particles to measure zeta potential within a microchannel, however, is cumbersome as the electrophoretic contribution of the particle has to be taken into account. Sze et. al. (2003) measured the averaged electroosmotic velocity within a microchannel and in turn inferred a zeta potential. Through the in-situ measurement capability of the MTV technique and charge neutrality of the tracers, part of this study addresses the measurement of zeta potentials of various surfaces. Knowledge of the zeta potential will help us in designing flow control within microchannels.

The layout of the rest of this thesis is as follows. Chapter 2 describes in detail the diagnostic techniques and instrumentation used to measure velocity and

temperature. For velocity measurements, the MTV technique (Gendrich et. al., 1997) is utilized while for temperature measurements, the phosphorescence characteristics of the chemicals used for MTV are exploited to yield temperature information (Hu et. al. (2001). This technique is termed Molecular Tagging Thermometry (MTT). The experimental setup for both electroosmotic and pressure driven flows is described next as well as the surface modifications performed on the microchannels. Chapter 3 introduces pressure-driven flows and the various issues pertaining to it with results and discussions at the end of the chapter. Chapter 4 delves into the intricacies of electroosmotic flow. The electric double layer and principles of electroosmosis are initially described followed by the experimental results.

Chapter 2 Experimental Setup & Measurement Techniques

In this chapter, the various experimental setups needed for experiments in pressure-driven and electroosmotically-driven flows are described. The optical setup for MTV and the imaging system are initially presented. Next the construction and surface modifications of the microchannels are described followed by the flow setup. The chapter concludes with presentation of the MTV and MTT techniques.

2.1 Optical Setup

The use of MTV in this study warrants the use of a UV laser and a range of optics to shape the laser beam. Traditionally, a 308nm wavelength laser was used for tagging of the flow. In this study, however, a different wavelength was used due to beam focusing issues. This is the first implementation of the MTV technique with a 266nm wavelength laser. The laser utilized is a Continuum© Powerlite 9030 running at a wavelength of 266nm with peak energy levels of 115mJ/pulse and a repetition rate of 30Hz. The laser beam is circular in shape (~8mm diameter) and has a nearly Gaussian energy distribution. To ensure a symmetric profile of the laser beam, the laser is usually firing at high energy levels. However, due to the low energy requirements of these experiments at micro scales, a large amount of the laser energy has to be removed before allowing the beam to impinge on the experimental setup. A high energy level is known to damage the quartz walls of the microchannels and could also cause excessive bleaching of the MTV chemicals.

The laser energy is initially set to an estimated energy level of 50mJ/pulse. The laser beam is subsequently passed through a 99.9% beam splitter to reduce the energy to 0.1%. At 0.1% of the initial energy, the energy per pulse of the laser beam is estimated at 0.05mJ/pulse. A spatial filter is added to the optical setup to improve the

beam quality. Spatial filtering is achieved by two 50mm spherical lens and a pinhole. Further improvements to the beam quality can be achieved with smaller focal length lens and a smaller pinhole. Eventually, a 12.7mm focal length lens is used to focus the beam into a thin line. All optics used were UV grade synthetic fused silica acquired from CVI Laser LLC with a damage threshold of 10J/cm^2.

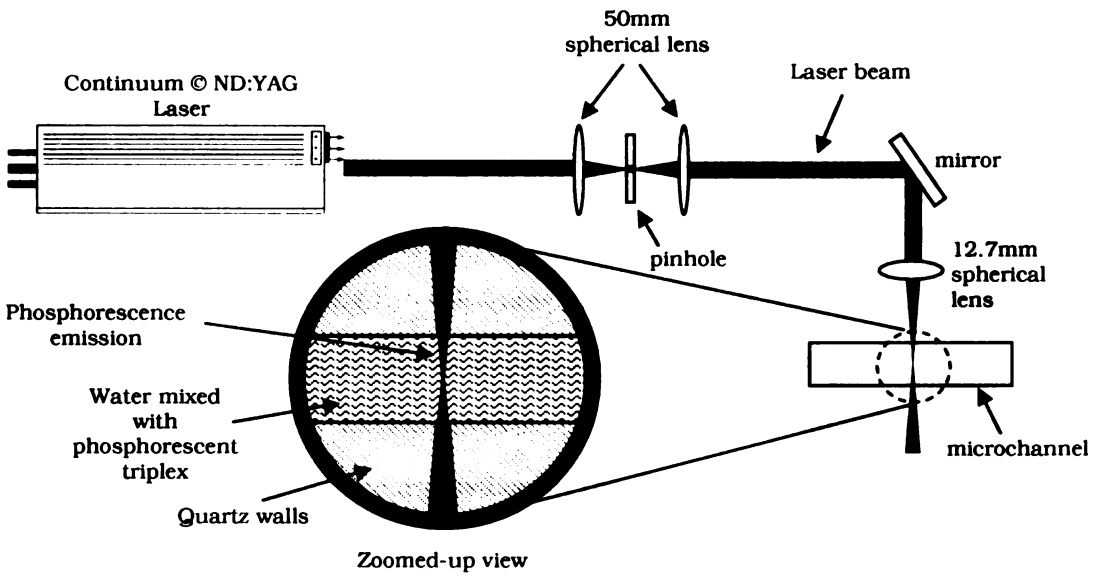

Figure 2-1. Optical setup for experiments

The current setup has been able to create laser lines as thin as 13μm (full width at half maximum, FWHM) although most of the experimental results were obtained with a 25μm line width. The minimum line width is not always achievable depending on how accurately the optics were aligned. At the focal spot size of 13μm, the energy density has increased to 37J/cm^2 which is beyond the damage threshold of the best UV lenses (due to the limits of the damage threshold on the anti-reflection coating) and near the limits of quartz. Through experimentation with the beam energy and the focal spot size, a realizable working condition is achieved for tagging of the MTV triplex. The optical setup described is shown in Figure 2-1. The optical setup is common between the pressure driven and electroosmotic flow experiments.

2.2 Imaging System

Low light levels of phosphorescent chemicals used here for MTV require the use of intensified cameras. Two different cameras were utilized. A Xybion ICCD (Xybion Corp.) camera was used specifically for velocity measurements in the pressure driven flow studies due to its high gain. The image acquisition rate at full frame (640x480 pixels) is 30Hz. A Mutech M-Vision 1000 PCI Bus Frame Grabber was used to acquire images to a PC. For simultaneous measurements of electroosmotic velocity and its corresponding temperature profile, a Dicam Pro (PCO AG) intensified camera was used. An acquisition rate of 7Hz at full frame (1280x1024 pixels) is achievable. This camera has the capability of imaging two full frame images (double-shot mode) successively in a short time frame (as fast as 500ns between 2 frames) and its gain stability makes it suitable for temperature measurements. Gain stability is an added benefit as the charging characteristics of the intensifier on the camera does not need to be accounted for in the temperature measurements. The measurements of gain stability and charging capability of the camera in the double-shot mode are documented in Appendix C. For the Xybion ICCD, the two consecutive images required for velocity measurements were acquired separately under the assumption that the flow field does not change with time. This is a good assumption since the flow is steady, fully developed and laminar. In an electroosmotic flow setup, the temperature and velocity changes with time and the pair of images need to acquired consecutively.

A 10X Mitutoyo (Infinity Corrected M Plan Apo Long Working Distance) objective was used in all the experimental work presented here. This apochromatic lens is aberration corrected for red, blue and yellow. It has a working distance of 33.5mm and a depth of focus of 3.5μm with a numerical aperture of 0.28. Since the objective is infinity corrected, a Mitutoyo tube lens (MT-40) is needed after the objective to focus the image at the imaging plane of the camera. A distance of 170mm between the tube lens and the camera is required for the correct magnification of the image. Further details of

the lens setup are provided in Appendix A. Although the objective is rated at 10X, the effective magnification observed by the cameras is less due to the optical system within the camera. An effective magnification of 6.6X was observed for the Dicam Pro and 5.9X for the Xybion ICCD. The magnification calibration of the camera is provided in Appendix B.

For synchronization of the Xybion ICCD camera to the laser, the internal timing of the camera was used as the trigger source while for the Dicam Pro, an external delay generator was used. Digital delay generators from Stanford Research Systems Inc. (DG-535) and Berkeley Nucleonics (BNC 555) were used in the setup. The full description of the various timing and cable connections are provided in Appendix D.

2.3 Microchannels

2.3.1 Channel Construction

The microchannels used for flow measurement are homemade and are nominally 300μm in height, 25.4mm in width and 63.5mm in length. For electroosmotic flow studies, a 5mm channel width was used instead. The width for EOF was reduced due to the available electric current used to transport fluid in an electroosmotic experiment and the length is designed to allow for a sufficient entrance length and other optical access issues. Beam steering effects and optical distortion due to the curvature when using capillaries can cause a misrepresentation of the results. This is shown in Appendix G for a commercial quartz microchannel. Although software techniques can be used to correct for some of these effects, it is a tedious effort. The microchannels used in this research are all rectangular channels with flat sides to eliminate any of these effects.

Molecular tagging techniques usually require an excitation laser to "excite" the lumophore. In this study, a UV laser is utilized and regular channels made of

borosilicate or Pyrex absorb part of the energy of the incident laser. This is due to reduced optical transmission and higher absorption at deep UV wavelengths and increases the possibility of damage to the channels. The absorption also reduces the amount of energy that is available for excitation of the lumophore. Synthetic fused silica (hereafter referred to as quartz), which has a higher purity than natural fused quartz, is being used throughout this research as it exhibits high transmission and lower UV absorption levels. Figure 2-2 illustrates the transmission spectra of the particular type of quartz (Corning 7980) used in all the channel fabrication. The absorption at 248nm is listed as 0.2% while at 198nm, the absorption is only 1% for a 10mm thick specimen. This material exhibits excellent transmission characteristics in the Deep UV (DUV) range. Since all the microchannels are made of quartz glass thinner than 5mm, absorption is minimal.

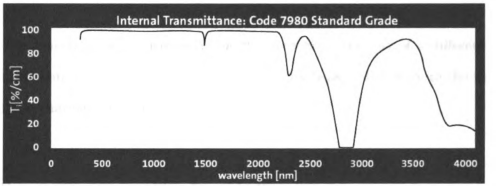

Figure 2-2 Corning 7980 Transmission Spectra (Corning Inc.)

To make a microchannel, 4 pieces of quartz flats are used. For the top and bottom walls of the microchannel, quartz flats 1" x 1/8" x 3" (w x h x l) in size were used and separated by a gauge block to space out the microchannel height. The gauge block (Mitutoyo Corporation) has an uncertainty of 60.96nm and is NIST traceable. This assembly of a gauge block sandwiched between two quartz flats is secured and two additional quartz flats 6.35 x 1 x 76.2mm (w x h x l) are glued in place as the side walls.

The glue used is RTV Silicone. The silicone glue is allowed to cure for 24 hours before the microchannel is handled.

For the pressure driven flow setup, the microchannels are mated to Plexiglas adapters which are fitted with hose barbs. The hose barbs are connected with tubing to the constant head reservoirs or the syringe pump. This is shown in Figure 2-3. The materials chosen for the setup is known to be inert to the working fluid and the chemicals slated for use in this research.

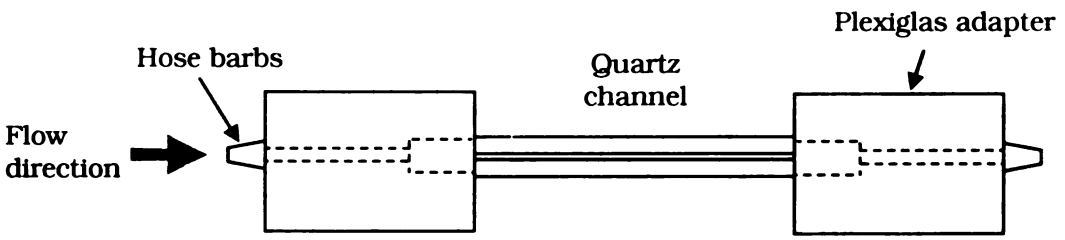

Figure 2-3. Schematic of a completed rectangular quartz channel.

The investigation of electroosmotic flows requires the use of a different setup. The quartz channels are still used but reservoirs are attached directly to the inlet and outlet of the channels. The setup is shown in § 2.4.3.

2.3.2 Preconditioning and Surface Modifications

Glass surfaces usually exhibit a negative surface charge when exposed to aqueous solutions. The adsorption of impurities on the surface, however, creates non-uniformities in this surface charge. Quartz channels which are untreated have varying levels of uniformity of surface charge and this can cause experiments to be inconsistent and surface coatings to be non-uniform. To eradicate this problem, preconditioning of quartz channels is crucial.

Methods employed by other researchers (Faller et. al., 1999, Raber et. al., 2000, Dabek-Zlotorzynska et. al., 2001) for preconditioning channels essentially reduces to

the rinsing of the channels in either an acid or a basic solution for an amount of time, followed by a rinse in water and a buffer solution. Different methods of pretreatment were used for detection of different chemicals. The use of hydrochloric acid for preconditioning, for example, caused problems for detection of certain chemicals as trace amounts of chloride ions remain in the channel. This resulted in spurious results due to cross contamination. The method utilized here, since we are not concerned with cross contamination, involves exposing the microchannels to a 1M solution of NaOH and 1M solution of HCl separately for 1 hour each and then rinsing with deionized water. The technique described here is similar to that described in Hau et. al. (2003) and further details of the chemical reaction that deprotonates the silanol groups are explained in the paper.

In this study, the microchannels are coated with different surfaces and the flow physics within these microchannels are then studied. The treated microchannel with a uniform surface charge is coated with polymer brushes or a hydrophobic monolayer. Surface modifications with OTS increases the hydrophobicity of quartz channels, while growing polymer brushes modifies the surface charge and the morphology of the quartz channels. These surface modifications can affect the flow field within channels and it is these affects that would be studied in this research. The OTS monolayer is typically prepared by immersing the channel within a 2mM solution of OTS in dicylcohexyl for a few hours. The channels are then rinsed with chloroform and dried. The channel is baked at 100°C overnight to crosslink the OTS molecules to form a robust layer. The polymer brush derivatization on a silicon surface is complicated and involves many steps and the details are provided in Huang et. al. (2002) and Kim et. al. (2000). A brief description of the technique is provided in Appendix I. All surface modified channels used in this research were made by Dr. Matt Miller at the Department of Chemistry at Michigan State University.

Surface characteristics of channels are expected to affect the flow field due to a change of zeta potential. The flow may exhibit a higher flow rate or a deviation from

standard fully developed flow profiles under different surface conditions. Hydrophobicity is the tendency for a surface to repel fluid due to surface tension. Material that has a tendency to attract fluid and causes a blob of water to spread out when placed on the surface is considered hydrophilic while the opposite is true for hydrophobic surfaces. Figure 2-4 below shows the relative surface tension of the polymer brush coating compared to the OTS-coated and uncoated quartz. These images show that the OTS treated surface exhibited the highest surface tension while an untreated quartz surface is more hydrophilic than quartz treated with polymer brushes. The polymer brushes can be grown to increase or decrease the hydrophobicity of the surface.

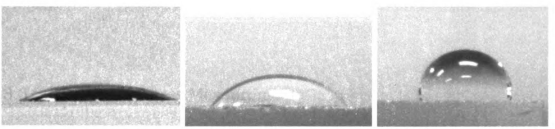

Uncoated quartz Surface | Quartz coated with polymer brushes | OTS-coated Surface (hydrophobic surface)

Figure 2-4. Comparison of hydrophobicity between uncoated, polymer brushes and OTS coated quartz surfaces (liquid used is water).

The use of the MTV technique requires the use of a high energy laser to tag the fluid within the channel. The amount of energy used to tag the fluid may also ablate the surface modifications performed on the quartz surfaces. This is a concern if the treated surface is damaged due to the tagging laser. The typical beam size (diameter) currently used is approximately 25μm, focused down from an original beam size of approximately 8mm. This translates to an energy density of ~10J/cm^2. Tests with a 100mJ/pulse laser with an energy density of ~0.2 J/cm^2 did not indicate any damage to the polymer brushes coating. Considering that 9000 pulses of the laser beam irradiated the sample, this energy density is deemed sufficient to investigate the possible damage on the

coatings. The following figure illustrates a scanning electron microscope (SEM) image of the quartz channel coated with polymer brushes before and after laser irradiation.

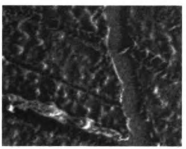

Before Laser Irradiation

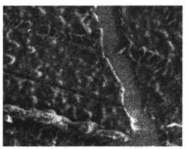

After Laser Irradiation

Figure 2-5. Scanning electron microscope (SEM) images of polymer brushes before and after laser irradiation (after ~9000 laser pulses).

2.3.3 Surface Roughness Measurements

Surface roughness of the various surfaces used in this work is quantified with atomic force microscopy (AFM) scans. All the scans were performed at the W.M. Keck Microfabrication Facility (Michigan State University) with the assistance of Dr. Baokang Bi. A Dimension 3100 Scanning Probe Microscope (SPM) with an active AFM probe (Veeco Instruments Inc.) was used in the measurements. Three circular quartz samples (1 inch diameter); one coated with OTS, one with polymer brushes (hereafter referred to as HEMA) and one left uncoated were scanned. Figure 2-6, Figure 2-7 and Figure 2-8 illustrate the surface scans of the various surfaces and their corresponding roughness values. The uncoated quartz surface illustrated in Figure 2-6 has a relatively low surface roughness at 0.87nm. The surface roughness values are presented in Table 2-1. Relative roughness values are usually quoted relative to the characteristic length of the microchannel. For round capillaries, the diameter is used but in this case, the 300μm height (H) or the hydraulic diameter (D_H) can be used interchangeably.

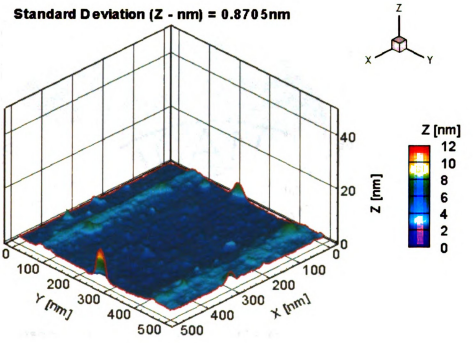

Figure 2-6. AFM scan of uncoated quartz

Surface	Surface Roughness (nm)	Relative roughness, ε/H (10^{-6})	Relative roughness, ε/D_H (10^{-6})
Quartz	0.8705	2.9	1.47
OTS	4.743	15.81	7.99
HEMA	5.949	19.83	10.03

Table 2-1. Surface roughness values for various surfaces

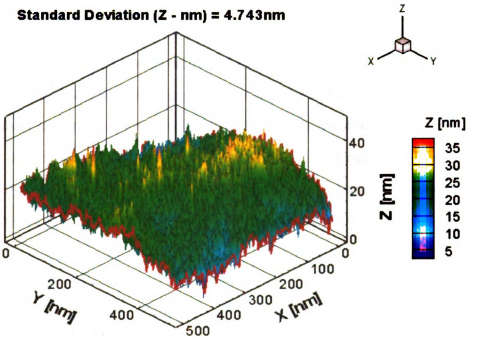

Figure 2-7. AFM scan of OTS coated quartz.

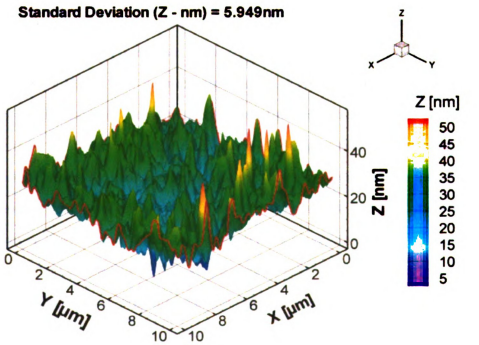

Figure 2-8 AFM Scan of HEMA Coated Quartz

From the figure, the roughness in the HEMA coated quartz is of a lower spatial frequency than the OTS coated quartz although the roughness values are higher. The high frequency roughness displayed in OTS coated quartz may be the reason slip occurs due to a higher probability of trapped bubbles and the reduction in contact between the moving fluid and the microchannel surface. Even with the different coatings (OTS and HEMA), the roughness values are about 3 orders of magnitude lower than that measured by Phares and Smedley (2004). Thus the experimental results presented in this work can be considered to be in the limit of a smooth surface.

2.4 Flow Setup

2.4.1 Pressure-Driven Flows

The first experimental setup was initially created to provide for very accurate control of flow rates with minimum costs. Two constant head reservoirs were placed at the inlet and outlet of the microchannel and the vertical traverse of one of these reservoirs would vary the pressure drop across the microchannel. This setup is shown in Figure 2-9. The reservoirs were each made of Plexiglas and connected to the quartz microchannel assembly through Teflon tubing. For each reservoir, a pump is used to continuously provide an overflow to maintain a constant head on each end of the microchannel. The overflow from the two reservoirs is channeled into a larger reservoir. Some of the data presented in this study were obtained with this experimental setup. One disadvantage to varying the pressure gradient with this technique is the large range of height needed to create different flow rates (the velocity is proportional to the square root of height).

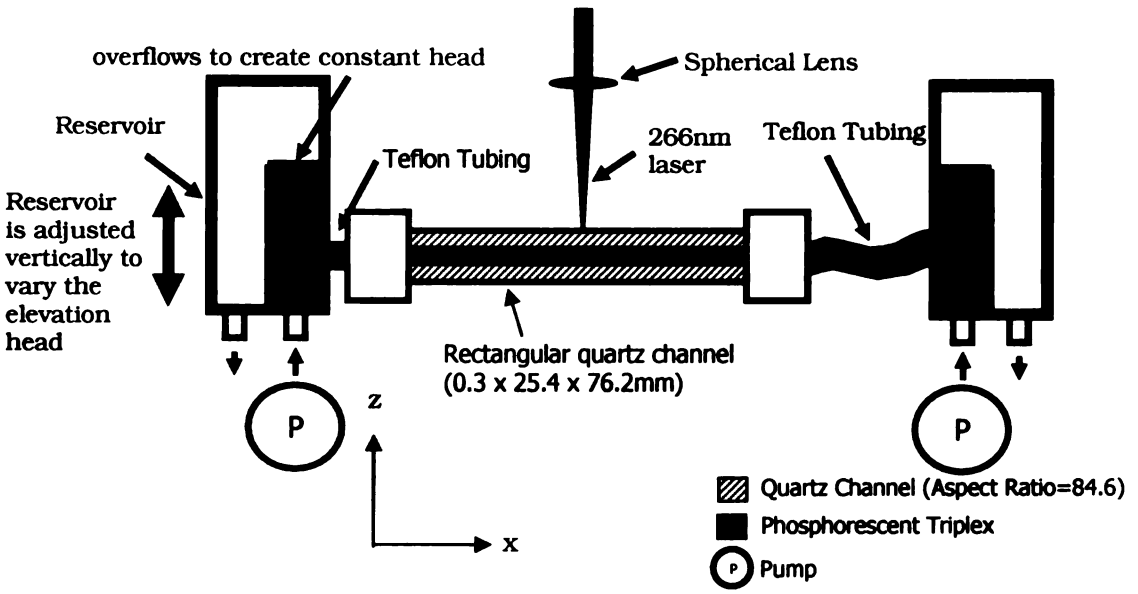

Figure 2-9 Experimental Setup for Pressure Driven Flow (side view, x-z plane)

To circumvent this difficulty while still maintaining flow rate accuracy, a syringe pump (Harvard Apparatus pHD 22/2000) is utilized to provide a larger range of flow rates. The syringe pump is rated with an accuracy of $\pm$ 0.35% of the reading with a reproducibility of 0.05% and a minimum achievable flow rate of 0.0001μL/hour. For the flow rates in this study (0-310mm/s peak velocity), the syringe pump causes a maximum fluctuation of only $\pm$ 0.35ml/s.

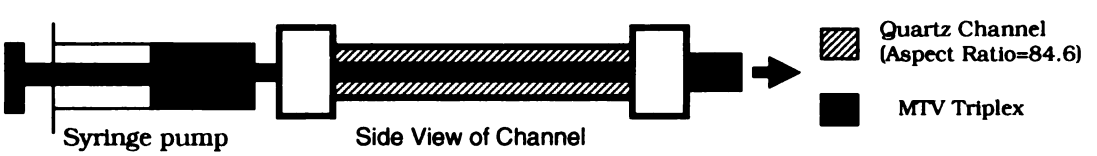

Figure 2-10. Setup for Pressure Driven Flows with Syringe Pump (x-z Plane)

The syringe pump is initially preloaded with the phosphorescent triplex solution before the start of an experiment. The syringe pump is preprogrammed for a particular flow rate and a given time for any flow transients to dampen out before the start of any

experiments. At the other end of the experimental setup (Figure 2-10), the flow discharges into a beaker. The syringe used is a 100ml stainless steel syringe which is refilled from a beaker after each run. In both experimental setups, care is taken to ensure that while the microchannel is filled, no bubbles are trapped. Any trapped bubbles could potentially cause the flow field to be affected. An illustration of the general experimental setup for pressure-driven flows is provided in Figure 2-11.

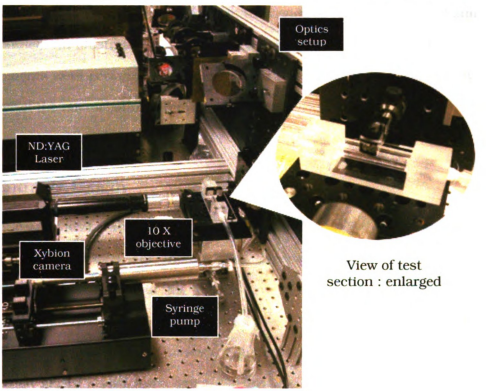

Figure 2-11 Illustration of test section (syringe pump setup)

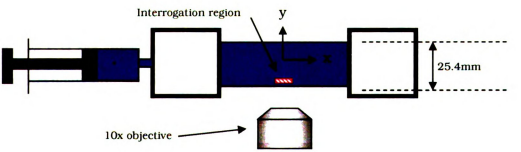

Figure 2-12 Schematic of experimental interrogation location (top view, x-y plane)

All the measurements were performed near the edge of the side walls (-11.2 < y < -9.7mm, -5mm < x < 5mm) where the signal to noise of the acquired images is better compared to the center of the channel. The determination of the interrogation region is based on calculations of the entrance length and the analytical solution of the flow field within a rectangular microchannel at the x and y location selected for the experiments. The velocity profile and its corresponding shear stress are found to be insensitive towards changes in Y-axis locations (only in the region of -12.2mm < y < 12.2mm in the microchannel). An illustration of the interrogation region is provided in Figure 2-12. All measurements were performed in the range of 1.5-3mm away from the wall (y-axis) in the center of the microchannel (-5mm < x < 5mm).

2.4.2 Entrance Length

The analytical results used to compare with the experiments are computed for the fully-developed region. For any duct flow experiments, it is important to establish the entrance length to obtain the propagation length of inviscid behavior. This is important so that the interrogation region for any experiments is in the fully-developed region. For micro scaled flows, however, the characteristic lengths involved are much smaller than macro scaled flows and it is expected that the entrance length be short. This is estimated by the following equation (White, 1991).

$$l_E = 0.04 * H * \mathrm{Re}_{CH} \qquad 2\text{-}1$$

where l_E is the entrance length, H is the characteristic height of the microchannel and the Reynolds number is based on the characteristic height. For the maximum Reynolds number considered in this study, the entrance length for a 2-D microchannel is < 1mm. For our experiments, the measurement location is in the region of x = $\pm$5mm which is well beyond the entrance region.

2.4.3 Electroosmotic Flow Setup

Two Plexiglas cylinders with a diameter of 84mm were used as reservoirs and mated to the microchannel. The large diameter of the reservoirs was needed to minimize the formation of an elevation head which would cause a pressure gradient to contaminate the electroosmotic flow field. The consideration of this problem is outlined in Appendix E. Platinum wires were placed in each cylindrical reservoir near the channel inlet and outlet to act as electrodes. A high voltage potential is applied across these electrodes. A schematic of the electroosmotic flow setup is illustrated in Figure 2-13. The fluid used as the flowing medium is the phosphorescent chemical mix added with sodium phosphate as an electrolyte and buffer. More details on the use of sodium phosphate are discussed later.

A Wavetek Programmable Function Generator (Model 275) was used to provide a DC signal to a high voltage DC amplifier (Trek Model 609C-6) which amplifies the input by 1000x before applying it to the electrodes. This creates an electric potential across the length of the microchannel needed for electroosmosis. The high voltage setup fixes the voltage but the electric current may vary due to changes in conductivity of the fluid within the microchannel. The actual current is monitored during the experiment by measuring the voltage drop across the inline resistor as shown in Figure 2-14.

For the setup shown in Figure 2-14, the resistor contributes to the overall current of the circuit. Experiments with a voltage of 2000V have yielded a current of 2mA. This essentially indicates a resistance of 1MΩ present in the fluid circuit through Ohm's Law. At this resistance level, the relative perturbation error (RPE) of the added resistor is computed and shown in equation 2-2. This level of perturbation will only increase the current within the circuit by 0.328%. For the range of voltages (560V-1963V) and current (0.5-2mA) in this experiment, the perturbation error from the current monitoring resistor is negligible.

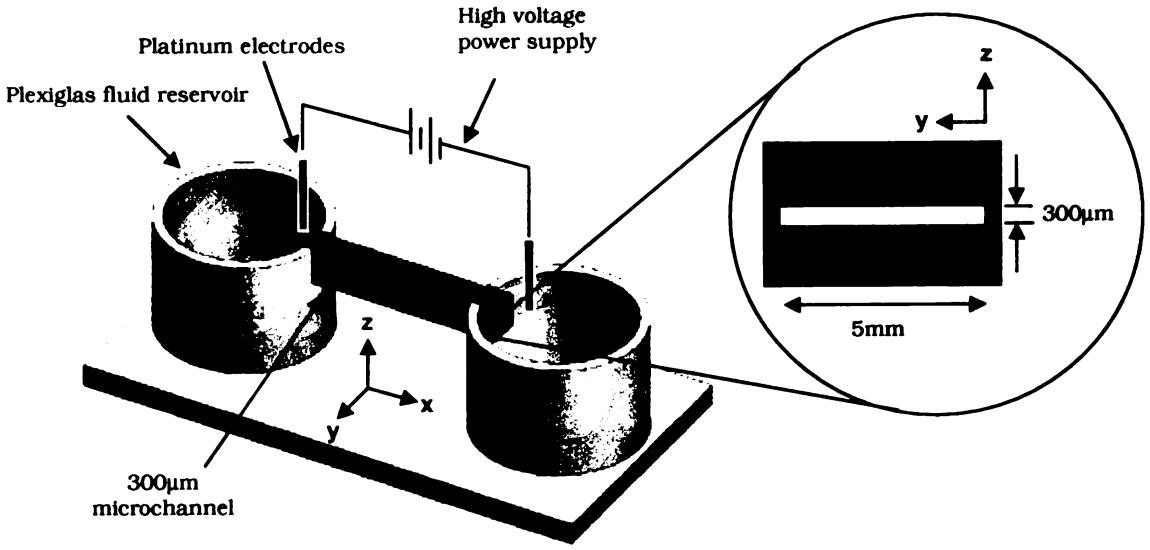

Figure 2-13 Schematic of EOF setup

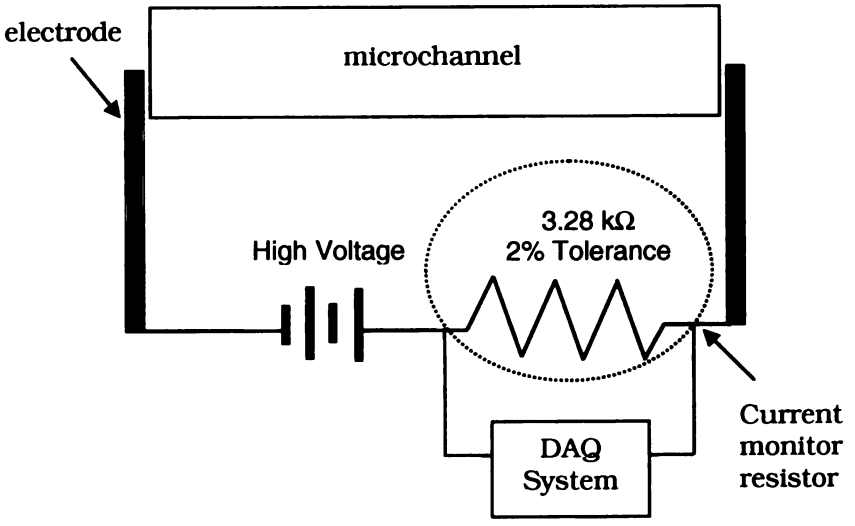

Figure 2-14. Current measurement setup

$$\% \text{ RPE} = \frac{R_1}{R_C + R_1} x100 = \frac{3280}{1x10^6} x100 = 0.328\% \qquad 2\text{-}2$$

2.5 Molecular Tagging Velocimetry

Molecular Tagging Velocimetry (MTV) is an optical technique for obtaining whole field velocity information in a plane. The current implementation of the technique is based on excitation of long lifetime molecular tracers that phosphoresces, flowing within the experiment of interest, by a laser at a suitable wavelength. These molecular tracers move with the flow and continue to emit light after the laser is turned off. The tracking of these tracers would then yield velocity information.

The long lifetime tracers used in this implementation of MTV is a phosphorescent chemical triplex, $1-BrNp\cdot M\beta CD\cdot ROH$, with typical molar concentrations of $1x10^{-4}$M Maltosyl-β-cyclodextrin, 0.055M neopenthanol and a saturated amount of 1-bromonaphtalene (approx $1x10^{-5}$ M). Figure 2-15 illustrates the schematic of the chemical configuration that allows the tracer to achieve long phosphorescent lifetimes (The particular capping alcohol used in this figure is tert-butyl).

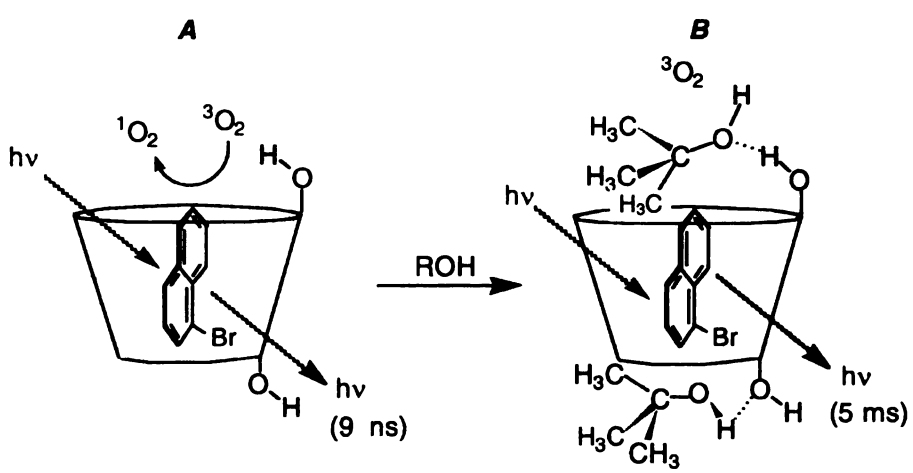

Figure 2-15 Chemical structure of Phosphorescent Supramolecule used here for MTV

Bromonaphtalene is the chemical that luminesces upon excitation by a UV laser. This chemical goes into the "cup" structure of cyclodextrin in a dynamic way and

while it is interspersed within cyclodextrin, cyclohexanol attaches to the "lip" of the "cup". The capping efficiency of cyclohexanol determines the degree of oxygen quenching. As oxygen, among others, quenches the phosphorescence emission of the chemical, a reduction in quenching causes an increase in lifetime of the emission. Figure A in Figure 2-15 illustrates the reduced lifetime (9ns) when dissolved oxygen is allowed to enter the "cup" structure of cyclodextrin. Figure B illustrates how alcohol attaches to the "lip" of the "cup" to shield bromonaphtalene from being quenched by oxygen to yield a resultant increase in lifetime to 5ms. The addition of these chemicals to water, due to the low concentration used, does not affect the general characteristics of water as the viscosity and density of water remains the same.

These long lifetime tracers are "excited" to a higher quantum state by an ultraviolet laser and the subsequent decay to a lower state produces emission in the visible wavelength. Typically, a pulsed laser (20ns or less pulse width) in the UV wavelength range is used to "tag" or "excite" the molecules in the region of interest. These "tagged" molecules are imaged at two successive instances, one right after the laser pulse and the second within the lifetime of the emission.

The delay time between the two images is dependent on the signal level of the intensified camera and the time required for a sufficient amount of pixel displacement between the tagged lines. The pair of images is then correlated to obtain velocity information. The measured Lagrangian displacement vector provides the estimate of the velocity vector. In Figure 2-16, two sets of laser lines were aligned orthogonally and used to excite the chemicals to form a grid pattern of "tagged" fluid.

The MTV technique has been continuously varied based on the nature of the problem involved to suit the application at hand. Single line tagging is by far the easiest implementation of MTV. This method provides a single component of velocity within the flow field. The drawback to this method is that knowledge of the flow field is needed *a priori* as single line tagging can only resolve 1 component of velocity perpendicular to the tagged line. For example, single line tagging was applied to the measurement of the

initial velocity within a plume during a solidification process due to its unidirectional velocity field (Figure 2-17).

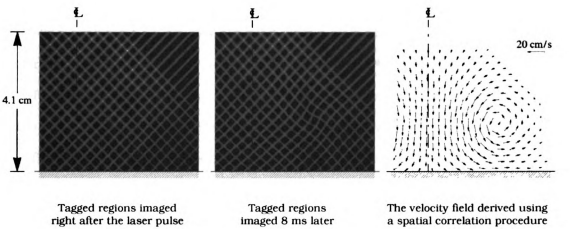

Figure 2-16 : Typical MTV image pairs and the corresponding correlated velocity vector field. (Gendrich, et. al., 1997) After 8ms, the tagged regions are imaged again to yield a distorted image due to the velocity of the fluid. Correlation of these images resulted in a velocity vector field as shown in the last image.

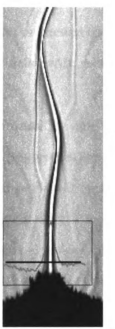

Figure 2-17. Image of plume during uni-directional solidification (red line indicates single component velocity profile, Lum et. al., 2001)

Laser line tagging, as illustrated in Figure 2-16, is commonly used to obtain 2 components of velocity in a plane and has been applied to the measurement of velocity very near the surface of a stalling airfoil (Gendrich, 1998), among others. In this same multi-line configuration, images obtained from a pair of cameras aligned at an angle with respect to the tagged line allow us to obtain the 3rd component of velocity in the out of plane direction. This technique, called stereoscopic imaging, was recently applied to the study of the 3-dimensional structure of a concentrated line vortex array (Bohl et. al., 2001). Detailed discussions of the planar 2-D technique applied to various flows are provided in Koochesfahani et. al. (1996), Gendrich and Koochesfahani (1996), Gendrich et. al. (1997) and Koochesfahani (1999).

In this research, single line tagging is utilized as it is expected that the flow field within microchannels would be unidirectional and fully developed. The assumption of fully developed flow is acceptable within microchannels as long as the interrogation region is sufficiently downstream of the channel inlet to avoid any entrance length issues. Only one component of velocity is needed to resolve the flow physics under these conditions. Flows within microchannels with recirculating features, however, would require the use of 2-component MTV.

The reduced area of laser illumination and the imaged field of view causes the amount of light collected by the imaging system to decrease compared to macro-scaled flows. The lower amount of light limits the delay between the two images needed for detection of slow moving flows. Neopenthanol is used to replace cyclohexanol (typically used due to its low cost) as the capping efficiency of neopenthanol is higher and causes a further reduction in oxygen quenching resulting in a higher emission. The relative intensity of phosphorescence emission by using neopenthanol compared to cyclohexanol and other available alcohols is provided in Figure 2-18. The use of a different laser wavelength in this study (266nm) compared to the typical 308nm wavelength also improves the absorption of the MTV chemicals which in turn should help increase the phosphorescence emission. Figure 2-19 illustrates the relative

absorption spectra of bromonaphtalene at different wavelengths. The relative absorption at 266nm is 7 times higher than at 308nm.

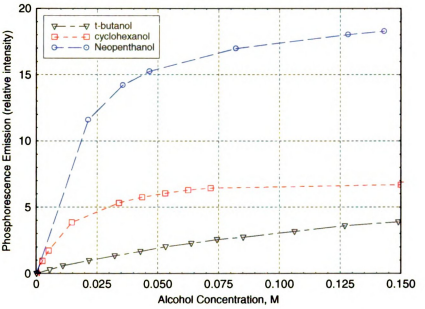

Figure 2-18. Total phosphorescence emission from 1-BrNp.Gβ-CD.ROH for three different types of alcohol at fixed concentrations of 1-BrNP and Gβ-CD and at 308nm wavelength laser excitation. (Plotted from Gendrich et. al., 1997)

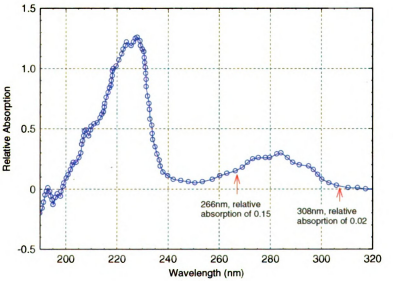

Figure 2-19. Spectraphotometer Scan of Relative Absorption of Bromonapthalene

2.5.1 Velocity Correlation Technique

Previous procedures for correlating a single tagged line (Lum et. al., 2001) utilized a peak detection algorithm. At the peak, a 2nd order fit is used to obtain subpixel accuracy of the measured displacement. The use of a peak detection algorithm, although simple in implementation, is vulnerable to noise contamination. Sharp noise spikes may affect the detection of the true line center and a high signal to noise is required to obtain accurate results. A higher order fit may also be necessary whenever the line profile does not appear to be Gaussian. In the current research, the accuracy of the single line velocity correlation technique was improved upon by using a spatial correlation technique and a 7th order polynomial fit to locate the center of the displaced lines. This is the 1-D implementation of the original 2-D correlation technique used for processing 2-component MTV data (Gendrich et. al., 1997)

The image pair obtained from the MTV technique, one imaged right after the laser pulsed and the other after a given delay, is spatially correlated, row by row, to give velocity profile information. Each row of pixel from each image is extracted and a convolution procedure applied to obtain the position of highest spatial correlation coefficient. The spatially correlated peak is fitted with a 7th order polynomial to obtain subpixel position accuracy. The spatial correlation technique is more impervious to noise spikes in the tagging line and would provide a better control on the accuracy of the correlations. The correlation program was written in Labview due to its friendly graphical user interface (GUI) and flexibility. The program was written to accommodate correlation of the whole image, or regions of interest only, in order to reduce processing time. The correlation data set is exported to a text file and subsequently read into a plotting program for data analysis. A description of the source code and the graphical user interface is provided in Appendix H.

The program was tested with images of known signal to noise ratios to determine the accuracy of the correlation procedure. Typical results yielded a displacement RMS

of < 0.1pixels. Figure 2-20 illustrates the RMS from the correlation of single tagged lines with different signal to noise (S/N) ratios at different line thicknesses.

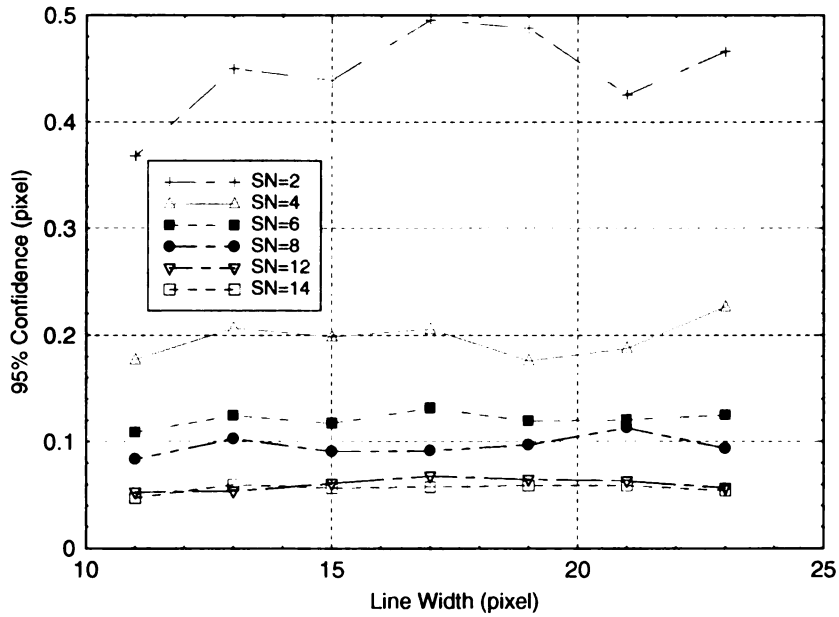

Figure 2-20. Uncertainties of correlated single tagged lines at different signal to noise ratios and line widths (full width at $1/e^2$).

2.5.2 Taylor Dispersion

Taylor dispersion can be induced by a combination of molecular diffusion and flow convection and is a phenomena that manifests itself in this study by broadening the tagged fluid. In a capillary, a dispersion coefficient is used to describe the extent of dispersion and is given to be proportional to the ratio of the axial convection to the radial molecular diffusion. This effectively represents the rate at which material spreads out axially in the system. For MTV experiments, if broadening of the tagged fluid occurs, the signal to noise ratio could decrease in the delayed image and may cause a higher RMS error in the correlation. Thus it is of interest to estimate the level of dispersion.

At the small time scales utilized in this study, however (which usually translates to low convective velocities), dispersion is dominated by molecular diffusion only and the convective velocity is not an issue. Longer time scales would cause the convective term

to dominate. The effects of diffusion can be estimated by calculating the broadening of the tagged line over time. This is represented by equation 2-3. (Miles et. al. 2000)

$$\omega^2 = \omega_o^2 + 8\ln(2)D\Delta t \qquad 2\text{-}3$$

where ω is the resultant thickness of the line, ω_o is the original width of the tagged line, D is the diffusion coefficient and Δt is the time delay across which the broadening is calculated for. For a representative diffusion coefficient of $5x10^{-6}$ cm^2/s (fluorescein), a line width, ω_o, of 25μm and a delay time, Δt, of 4ms, the eventual line width becomes 25.22μm. Thus a negligible amount of broadening is brought upon by molecular diffusion.

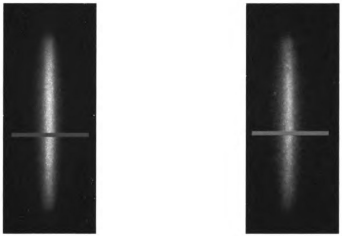

Figure 2-21 Undelayed (left) and delayed (right) images with line profiles drawn across the center of the image for electroosmotic flow

To further investigate the effects of dispersion, a line profile is drawn across an undelayed and a delayed image (average of 30 images) and is shown in Figure 2-21 and Figure 2-22. Again, the results illustrate that over a timescale of 4ms, the broadening of the tagged line is negligible.

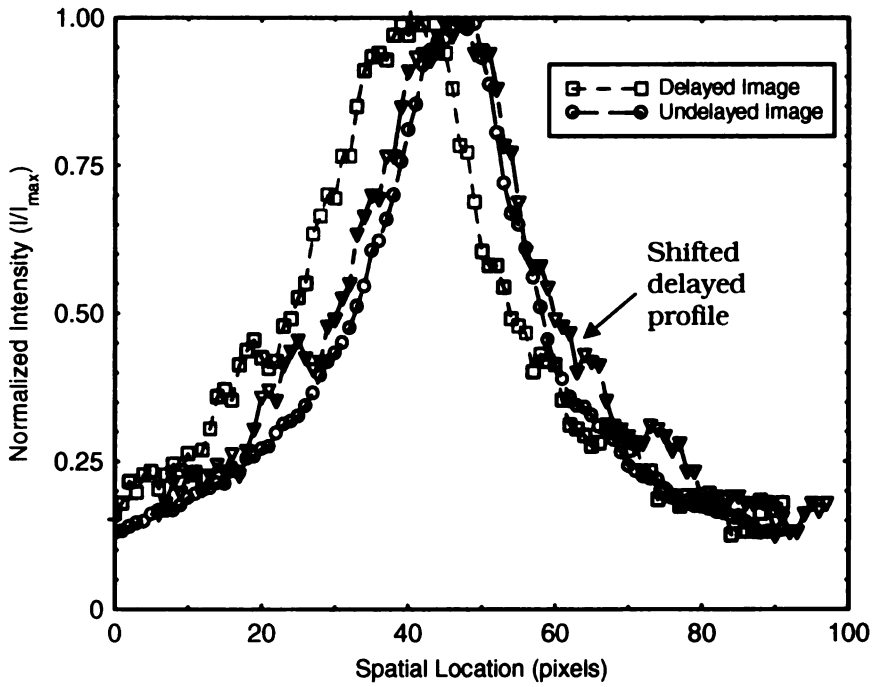

Figure 2-22 Comparison of line profile for undelayed and delayed images.

2.6 Molecular Tagging Thermometry

The original implementation (Thomson et. al., 2001) of Molecular Tagging Thermometry (MTT) was based on the intensity decay of the phosphorescent emission of the tagged molecules. This, however, could not correct for non-uniformities of the laser beam which could introduce errors into the measurement. Hu et. al. (2003) improved upon this technique by relying on the temperature dependence of the phosphorescence lifetime of the triplex instead. Through a ratiometric method, any non-uniformities of the laser beam or background are corrected for. The lifetime of the phosphorescent triplex are calibrated and is used to provide temperature information.

For a typical MTV application, the laser is used to create a 2-dimensional grid pattern and two images are taken in quick succession. These images are spatially correlated to obtain velocity information. The same images can yield temperature

information since the lifetime can be calculated from knowing the emission intensity decrease at a spatial location at two different times.

According to quantum theory, the emission decay of first-order photoluminescence is exponentially based. This is expressed by the following equation.

$$I_{em} = I_o e^{-t/\tau} \qquad 2\text{-}4$$

where τ is the time constant used to define a 37% drop from the initial intensity or the emission lifetime, I_o and I_{em} is the emitted intensity. The region of interest S_1 and S_2 in Figure 2-23 represents an area averaged to yield temperature information.

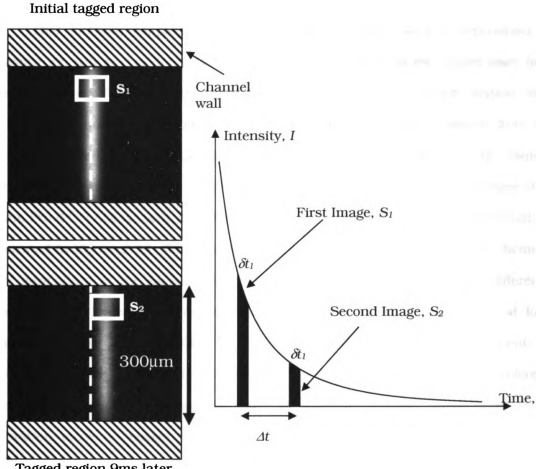

Figure 2-23 Exponential decay of phosphorescence intensity

The phosphorescence emission decays exponentially and is depicted in the plot. It turns out that the division of the intensity integrals at these two instances in time only depends on the time delay between images and the phosphorescence lifetime. This is shown in equation 2-5. Note that it is important to integrate the intensity of the same molecules in both images for this relation to be true.

$$\frac{S_2}{S_1} = e^{-\frac{\Delta t}{\tau}} \qquad 2\text{-}5$$

where Δt is the time delay between the two images. For the current work, both undelayed and delayed images have the same exposure times to yield equation 2-5. The exposure times can be set differently to increase the dynamic range of the measurements.

This method, coupled with the calibrated phosphorescence dependence on temperature, will give us temperature profile information along the tagged laser lines. This temperature field is obtained simultaneously with velocity field information. Since the chemicals used by Hu and Koochesfahani (2004) are slightly different from that used in this research (difference in the alcohol used) a recalibration of the chemical lifetime dependence on temperature was performed.Using the double shot feature of the Dicam Pro (PCO AG) camera, the lifetime variation with temperature was measured and illustrated in Figure 2-24. When the calibration results for the two different chemicals were normalized at the same temperature, the data points showed slight differences accentuated at lower temperatures due to less sensitivity of the technique at lower temperatures (Hu et. al. (2005)). To apply the technique during an experiment, the initial temperature of the fluid is recorded with a thermocouple. This gives a reference point for the measured lifetime at room temperature which is used to fit to the calibration curve to obtain temperature information. Another important aspect in implementing MTT is background correction of the images. Since the technique is based on intensity, any spurious contribution from the background could cause errors in the

measurements. All the measurements performed in this study were background corrected to avoid this error.

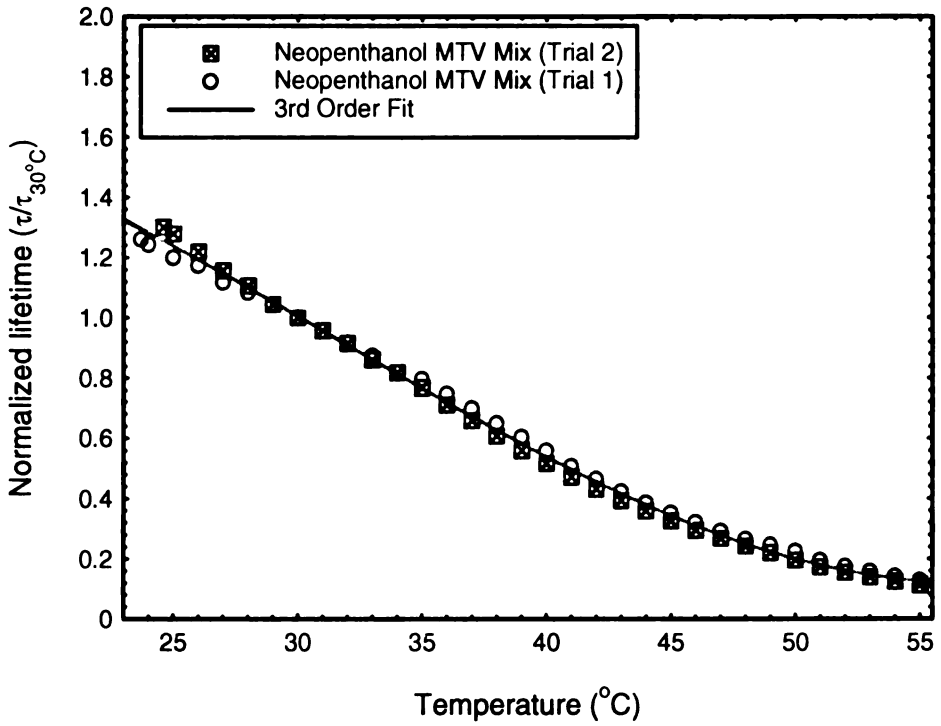

Figure 2-24. Normalized lifetime of both chemicals

Chapter 3 Pressure-Driven Flows

The solution for pressure driven flows within round capillaries are well-known and available in most fluid mechanics textbooks. In this chapter, the equations of motion for capillary flows are initially introduced and contrasted to the series solution for rectangular channels. The three-dimensional velocity profile for a rectangular channel is numerically computed to illustrate the differences. A measure of deviation from classical theory is the friction factor and this is computed for comparison with other researchers. The derivation of the friction factor for rectangular channels is presented along with the required experimental measurements to obtain the normalized friction factor. The "Results and Discussion" section first explores the errors involved in pressure drop measurements due to uncertainties in the channel dimensions and moves on to presenting the experimental results used to calculate the friction factor for uncoated, OTS or HEMA-coated microchannels. The friction factor results are then compared with theory and results from other researchers. Other factors that could affect the friction factor are also presented.

3.1 Equations of Motion

The exact solution for a fully-developed pressure driven laminar flow within a capillary (i.e. Poiseuille flow) is well known. The Navier-Stokes equations in combination with the conservation of mass equation, fully characterizes the flow of incompressible Newtonian fluids. The full Navier-Stokes equation in cylindrical polar coordinates can be written as follows, using (u_r, u_θ, u_x) as the three components of velocity.

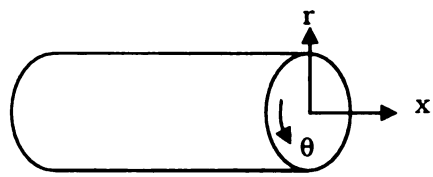

Figure 3-1. Coordinate system for capillary

$$\rho\left(\frac{\partial u_r}{\partial t}+u_r\frac{\partial u_r}{\partial r}+\frac{u_\theta}{r}\frac{\partial u_r}{\partial \theta}-\frac{u_\theta{}^2}{r}+u_x\frac{\partial u_r}{\partial x}\right)$$
$$=-\frac{\partial p}{\partial r}+\mu\left[\frac{1}{r}\frac{\partial}{\partial r}\left(r\frac{\partial u_r}{\partial r}\right)-\frac{u_r}{r^2}+\frac{1}{r^2}\frac{\partial^2 u_r}{\partial \theta^2}-\frac{2}{r^2}\frac{\partial u_\theta}{\partial \theta}+\frac{\partial^2 u_r}{\partial x^2}\right] \qquad 3\text{-}1$$

$$\rho\left(\frac{\partial u_\theta}{\partial t}+u_r\frac{\partial u_\theta}{\partial r}+\frac{u_\theta}{r}\frac{\partial u_\theta}{\partial \theta}-\frac{u_r u_\theta}{r}+u_x\frac{\partial u_\theta}{\partial x}\right)$$
$$=-\frac{1}{r}\frac{\partial p}{\partial \theta}+\rho g_\theta+\mu\left[\frac{1}{r}\frac{\partial}{\partial r}\left(r\frac{\partial u_\theta}{\partial r}\right)-\frac{u_\theta}{r^2}+\frac{1}{r^2}\frac{\partial^2 u_\theta}{\partial \theta^2}+\frac{2}{r^2}\frac{\partial u_r}{\partial \theta}+\frac{\partial^2 u_\theta}{\partial x^2}\right] \qquad 3\text{-}2$$

$$\rho\left(\frac{\partial u_x}{\partial t}+u_r\frac{\partial u_x}{\partial r}+\frac{u_\theta}{r}\frac{\partial u}{\partial \theta}+u_x\frac{\partial u_x}{\partial x}\right)$$
$$=-\frac{\partial p}{\partial x}+\rho g_x+\mu\left[\frac{1}{r}\frac{\partial}{\partial r}\left(r\frac{\partial u_x}{\partial r}\right)+\frac{1}{r^2}\frac{\partial^2 u_x}{\partial \theta^2}+\frac{\partial^2 u_x}{\partial x^2}\right] \qquad 3\text{-}3$$

where ρ is density, t is time and p is pressure. Equations 3-1, 3-2 and 3-3 are representations of the Navier Stokes equations along the different axes. For a steady, incompressible, fully-developed laminar flow within capillaries, the velocity profile is characterized by an exact solution to the Navier-Stokes equations. Under these conditions, the three equations of motion simplify to

$$0=-\frac{\partial p}{\partial r} \qquad 3\text{-}4$$

$$0=-\frac{1}{r}\frac{\partial p}{\partial \theta} \qquad 3\text{-}5$$

$$0=-\frac{\partial p}{\partial x}+\mu\left[\frac{1}{r}\frac{\partial}{\partial r}\left(r\frac{\partial u_x}{\partial r}\right)\right] \qquad 3\text{-}6$$

Integrating Equation 3-6 results in a paraboloid velocity distribution

$$u_x = \frac{1}{4\mu}\left(\frac{\partial p}{\partial x}\right)\left(r^2 - R^2\right) \qquad 3\text{-}7$$

where R is the radius of the capillary. Physically, the velocity distribution within a capillary is a paraboloid and the volume flow rate is given by

$$Q = 2\pi \int_0^R u_x \, r \, dr \qquad 3\text{-}8$$

In order to obtain a relationship between volume flow rate, Q, and pressure gradient, Equation 3-8 is integrated to give

$$Q = \frac{\pi D^4}{128\mu}\left(-\frac{\partial p}{\partial x}\right) \qquad 3\text{-}9$$

Note that flow rate scales with the 4th power of diameter. This condition has a significant impact on the accuracy of measurements of friction factor using bulk flow measurement techniques. An uncertainty of 2% in determination of the diameter, D, results in an uncertainty of 8% in the flow rate.

The fully-developed flow within a rectangular channel is also based on the solution of the Poisson's equation ($\nabla^2 u_x = 1/\mu(\partial p/\partial x)$ but its solution is complicated by the geometry. This is provided in the form of a series solution. The series solution is depicted in the following equation for a rectangular section: -a $\leq$ y $\leq$ a, -b $\leq$ z $\leq$ b. (White, 1991).

$$u_x(y,z) = \frac{16a^2}{\mu\pi^3}\left(-\frac{dp}{dx}\right)\sum_{i=1,3,5\ldots}^{\infty}(-1)^{(i-1)/2}\left[1 - \frac{\cosh(i\pi z/2a)}{\cosh(i\pi b/2a)}\right]\frac{\cos(i\pi y/2a)}{i^3} \qquad 3\text{-}10$$

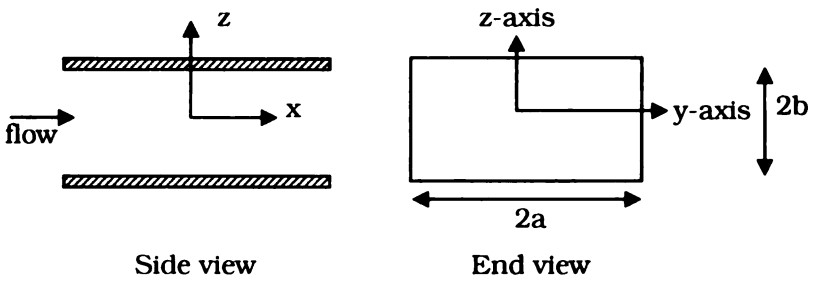

Figure 3-2. Schematic of channel geometry

where $u(y,z)$ is the velocity profile within the rectangular channel, a and b are the half width and half height respectively, dp/dx is the pressure gradient along a specified length of the channel and μ is the dynamic viscosity. Integration of this equation over the channel cross section yields the overall volume flow rate equation.

$$Q = \frac{4ba^3}{3\mu}\left(-\frac{dp}{dx}\right)\left[1 - \frac{192a}{\pi^5 b}\sum_{i=1,3,5\ldots}^{\infty}\frac{\tanh(i\pi b/2a)}{i^5}\right] \qquad 3\text{-}11$$

At any given y-location, the mean velocity is needed for comparison of the experimental results to theory. This is given in the following equation by integrating equation 3-10 in the z-axis.

$$\bar{u}_x(y) = \frac{32a^2}{\mu\pi^3}\left(-\frac{dp}{dx}\right)\sum_{i=1,3,5..}^{\infty}(-1)^{(i-1)/2}\left(b - \frac{2a\sinh(i\pi b/2a)}{i\pi}\right)\frac{\cos(i\pi y/2a)}{i^3} \qquad 3\text{-}12$$

3.2 Friction Factor

Friction factor is a non-dimensionalized representation of wall shear stress. For any viscous fluid flow, once the flow is fully developed (i.e. no acceleration), the shear stress counterbalances the pressure force. The shear stress for incompressible Newtonian fluids is linearly related to the rate of deformation and can be expressed in

Cartesian coordinates (refer to Figure 3-2 for axes designation) as shown in the following equations.

$$\tau_{xy} = \tau_{yx} = \mu\left(\frac{\partial u_x}{\partial y} + \frac{\partial u_y}{\partial x}\right) \qquad 3\text{-}13$$

$$\tau_{yz} = \tau_{zy} = \mu\left(\frac{\partial u_y}{\partial z} + \frac{\partial u_z}{\partial y}\right) \qquad 3\text{-}14$$

$$\tau_{zx} = \tau_{xz} = \mu\left(\frac{\partial u_z}{\partial x} + \frac{\partial u_x}{\partial z}\right) \qquad 3\text{-}15$$

where μ is the dynamic viscosity, u_x, u_y and u_z are velocity components in the x, y and z directions respectively. For a fully-developed flow within a rectangular duct, equations 3-13, 3-14 and 3-15 simplify to

$$\tau_{xy} = \tau_{yx} = \mu\left(\frac{\partial u_x}{\partial y}\right), \quad \tau_{zx} = \tau_{xz} = \mu\left(\frac{\partial u_x}{\partial z}\right) \qquad 3\text{-}16$$

It will be shown later that only τ_{xz} needs to be considered as the experimental data were obtained in the central region of the microchannel. The friction factor or sometimes referred to as the *Fanning* friction factor is defined as a normalized shear stress in Equation 3-17.

$$C_f = \frac{\tau_{xz}\big|_{wall}}{\frac{1}{2}\rho\bar{u}_x^2} \qquad 3\text{-}17$$

where $\bar{u}_x$ is taken to be the local mean velocity at any given x-z plane in our measurements. For laminar round capillary flows, it can be shown that the *Darcy*

friction factor is defined by f=64/Re (the *Fanning* friction factor, C_f, only differs from the *Darcy* friction factor, f, by a factor of 4).

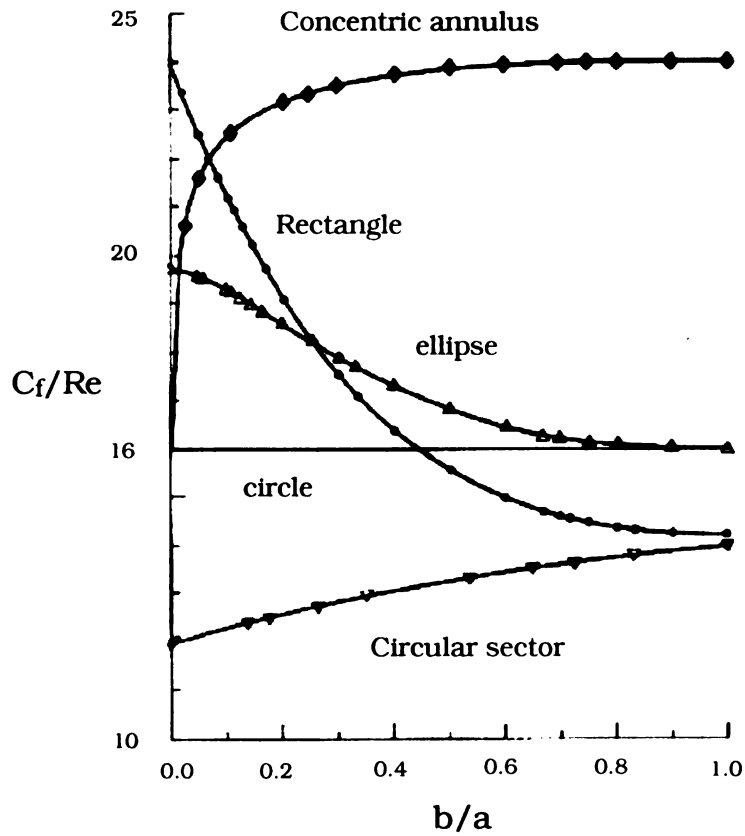

Figure 3-3. Fanning friction factor for different geometries
(White, 1991; data from Shah and London, 1978)

The Fanning friction factor for various geometries are shown in Figure 3-3 where b/a is the aspect ratio and Re is based on the hydraulic diameter. For a rectangular channel, as the aspect ratio increases, the ratio b/a decreases and approaches a strictly 2-D flow with a C_f shown in Equation 3-18.

$$f = \frac{96}{\mathrm{Re}} \qquad 3\text{-}18$$

To calculate the friction factor for a rectangular channel with a different aspect ratio, the series solution needs to be employed. The derivative of Equation 3-10, evaluated at the wall gives

$$\frac{\partial u_x}{\partial z}(y) = \frac{16a^2}{\mu\pi^3}\left(-\frac{dp}{dx}\right)\sum_{i=1,3,5\ldots}^{\infty}(-1)^{(i-1)/2}\left[\tanh(i\pi b/2a)*\frac{i\pi}{2a}\right]\frac{\cos(i\pi y/2a)}{i^3} \qquad 3\text{-}19$$

Substitution into Equation 3-17 yields the friction factor at the wall for a given x-z plane for rectangular channels with an arbitrary aspect ratio.

$$C_f(y) = \frac{32a^2}{\rho\bar{u}^2\pi^3}\left(\frac{dp}{dx}\right)\sum_{i=1,3,5\ldots}^{\infty}(-1)^{(i-1)/2}\left[\tanh(i\pi b/2a)*\frac{i\pi}{2a}\right]\frac{\cos(i\pi y/2a)}{i^3} \qquad 3\text{-}20$$

Investigation of flow physics and friction factor within microchannels are typically performed through the determination of the overall volume flow rate, Q, and pressure drop (Δp) measured across the length of the entire microchannel. Equation 3-18 is used to represent the theoretical friction factor with the Reynolds number derived from the volume flow rate measurements. Equation 3-21 is typically used by other researchers to derive the experimental friction factor from pressure drop and flow rate measurements, where l and D represents the length and hydraulic diameter of the channel respectively, ρ is density of the fluid and $\overline{U}$ is the mean velocity averaged over the entire cross section of the microchannel.

$$\Delta p = f\frac{l}{D}\frac{\rho\overline{U}^2}{2} \qquad 3\text{-}21$$

One major drawback to using the pressure drop to measure friction factor, apart from measuring bulk flow quantities, is the difficulty in accounting for the contribution of entrance effects (multiple experiments have to be performed to estimate the

contribution of entrance effects for a particular channel geometry). Recall that entrance effects cause a higher pressure drop to occur. Also, as noted previously (Equation 3-9), the D^4 dependence of volume flow rate, Q, could cause significant errors in the measurement of bulk flow quantities due to uncertainties in knowing the actual value of D (errors as large as 20% in friction factor due to a 5% uncertainty in channel dimensions). The combination of all these factors has motivated the current in-situ measurements for friction factor. In this study, the MTV technique is utilized to obtain local measurements of friction factor within a rectangular quartz microchannel with a nominal height of 300μm. The ability of the technique to measure spatially resolved velocity profiles across the height of the microchannel result in the determination of the local friction factor.

The measured experimental friction factor (equation 3-17) is then compared with the theoretical friction factor (equation 3-20) to illustrate any deviations from classical theory. This is illustrated in Equation 3-22 where the pressure drop, dp/dx, is substituted with the experimental mean velocity (equation 3-12).

$$\frac{C_{f,\exp}}{C_{f,theory}} = \frac{2\bar{u}_{theory}}{\bar{u}^2_{\exp}}\left(\frac{\partial u}{\partial z}\right)_{\exp}\left[\frac{\sum_{i=1,3,5..}^{\infty}(-1)^{(i-1)/2}\left(b-\frac{2a\sinh(i\pi b/2a)}{i\pi}\right)\frac{\cos(i\pi y/2a)}{i^3}}{\left(\sum_{i=1,3,5...}^{\infty}(-1)^{(i-1)/2}\left[\tanh(i\pi b/2a)*\frac{i\pi}{2a}\right]\frac{\cos(i\pi y/2a)}{i^3}\right)}\right] \qquad 3\text{-}22$$

The series in equation 3-22 is numerically computed for a given height and width of the microchannel although computation of $\bar{u}_{theory}$ requires the peak velocity measured from the experiments. The velocity gradient, $\left(\frac{\partial u}{\partial z}\right)_{\exp}$, and the mean velocity, $\bar{u}_{\exp}$, are all obtained from experiments. The velocity profiles obtained from the experiments are integrated and the local mean velocity calculated. The theoretical mean velocity, $\bar{u}_{theory}$, is obtained from integration of a parabolic profile at the interrogation location. This will

be shown in § 3.3 where the experimental results are presented. The parabolic profile matches the theoretical solution of flow in the central region (-12.2mm < y < 12.2mm) of a rectangular microchannel (25.4mm wide in the y direction) and is thus used for fitting of the velocity profiles obtained from the experiments.

3.3 Results & Discussion for Pressure-Driven Flows

To better illustrate the fully developed flow field within a rectangular channel, a computation of the series solution (Equation 3-10) was performed for various aspect ratios. Figure 3-4 illustrates the computational results obtained from the exact solution of the series solution for a channel of aspect ratio of 1. The color bar represents the normalized velocity, u/u_{max} where u_{max} is the overall maximum velocity across the cross section). Notice that the velocity profile resembles a paraboloid except near the wall boundaries where it tapers out to conform to the square boundaries of the channel.

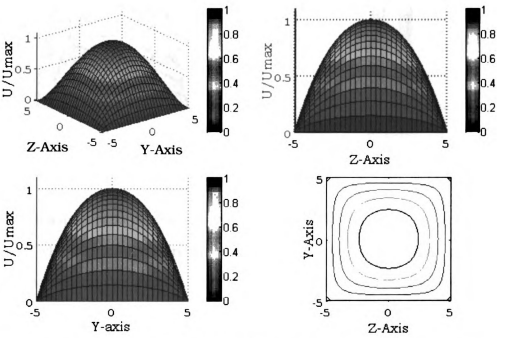

Figure 3-4. Series solution of velocity profile, u(y,z), within a square channel (refer to Figure 3-2 for axes designation)

With the current experimental setup, the width of the channel is 25.4mm and the height is 0.3mm. This translates to an aspect ratio of 84.667. For this aspect ratio, the flow field is parabolic only in the X-Z axis while in the Y-Z axis, the velocity profile is flat over most of the channel. To visualize the velocity profile within a channel of high

aspect ratio, Figure 3-5 is illustrated for a channel of aspect ratio of 5. The differences between the velocity profile within a microchannel with an aspect ratio of 5 and 84.667 lies only in the length of the central flat region.

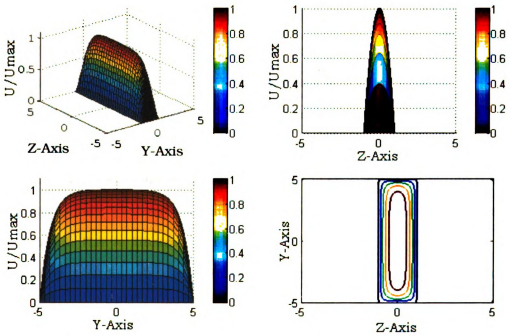

Figure 3-5 Series solution of velocity profile, u(y,z), within a 5:1 channel.

For the high aspect ratio channels used in this research, the profile along the Y-axis is almost flat while the profile along the Z-axis still maintains a parabolic profile across most of the width of the channel. This is in contrast to Figure 3-4 where a parabolic profile was observed along both axes of the channel. The computation of the series solution (Equation 3-10) allows us to predict *a priori* the expected flow field for our experimental tests and is the basis for our comparisons with classical theory. The comparisons with experiments were made at specific y-locations selected by the optical requirements of the imaging system.

Digressing, it is of interest to investigate the errors that may be involved in our comparisons to theory due to uncertainty in the exact y-location of the experimental interrogation regions. The normalized velocity computed from the series solution is

shown in Figure 3-6 for a microchannel with an aspect ratio of 84.67 (this is the microchannel used in the experiments). The data points are plotted along the y-axis in the center of the channel (Z=0). The velocity at different y-locations is normalized with the peak velocity at the center of the microchannel and the distance from the wall refers to the side walls of the microchannel in the Y-axis. The figure shows that the normalized velocity is close to unity as close as 0.5mm from the wall. Close inspection of this figure at 0.5mm reveals that the discrepancy in velocity from the center of the channel is less than 0.1%. Figure 3-6 illustrates that for a microchannel width of 25.4mm, $u(y, z = 0)$ does not deviate significantly in the range of -12.04 < y < +12.04mm. As long as the interrogation regions of the experiment are within this range, the velocity can be considered a constant. The velocity gradients at the wall also show the same trend. This is illustrated in Figure 3-7. This allows the experiments to have more flexibility given that the range of interrogation locations is not too constrained.

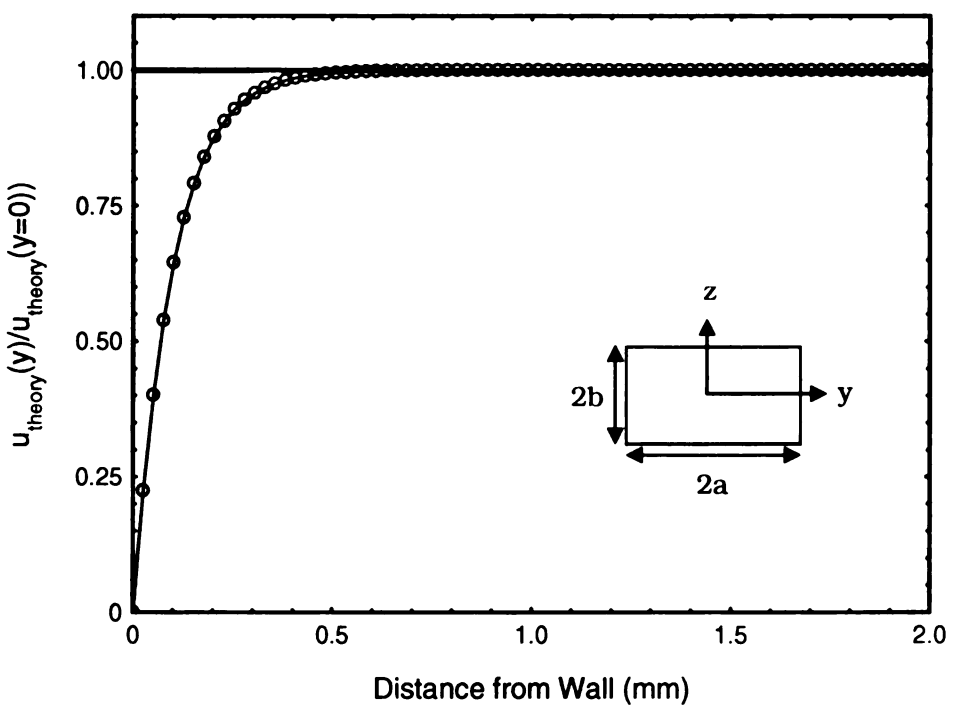

Figure 3-6. Change of velocity near the channel wall (Y-axis); aspect ratio of 84.67

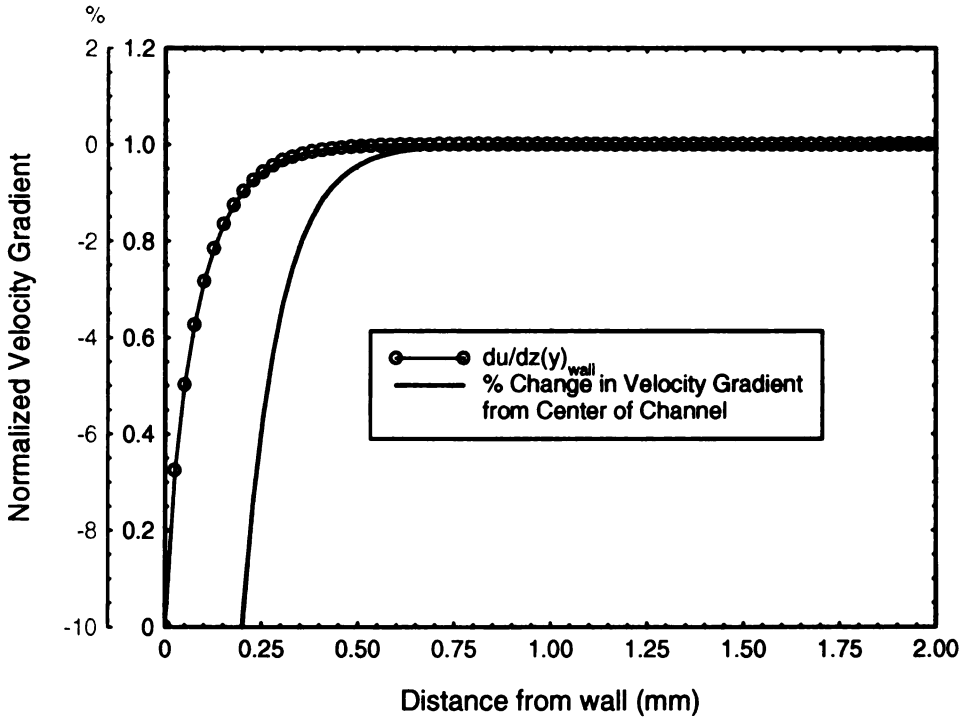

Figure 3-7. Normalized velocity gradients (du/dz) as a function of distance from walls

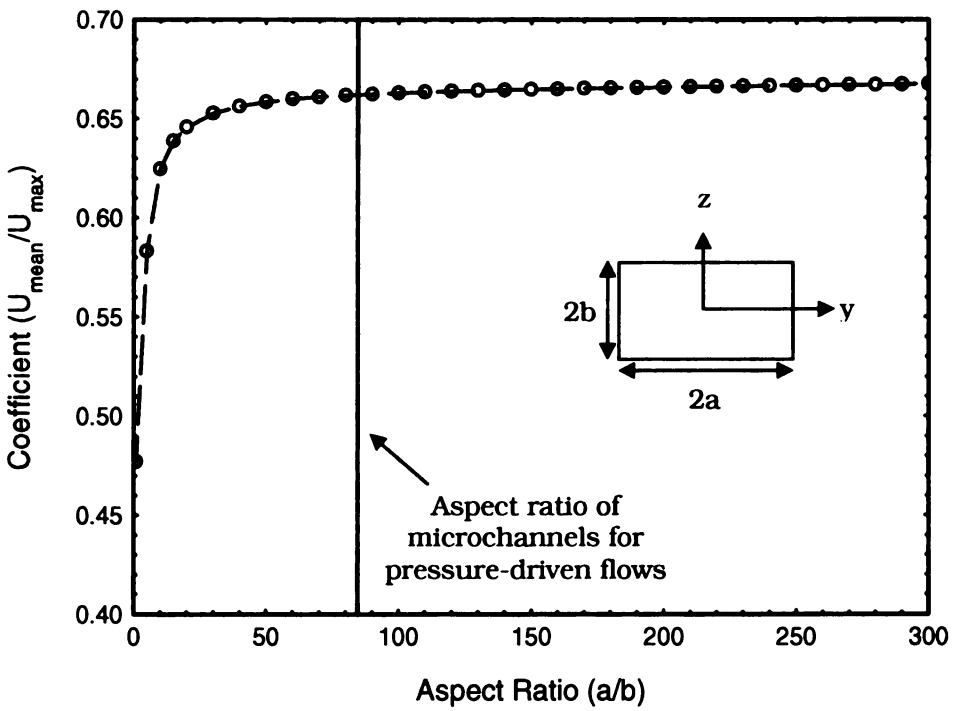

Figure 3-8 U_{mean}/U_{max} for different channel aspect ratios

An interesting observation of the series solution is that in order to achieve a strictly 2-D flow, a very high aspect ratio for a rectangular channel is needed. This is shown in Figure 3-8. As the aspect ratio becomes large enough, the flow field becomes more two-dimensional and thus yield a ratio of U_{mean}/U_{max} that asymptotically approaches a constant value where U_{mean} is the overall channel mean velocity and U_{max} is the maximum velocity. For a 2-D flow, the ratio U_{mean}/U_{max} would be 2/3. The microchannel used in this study (aspect ratio of 84.667) would not yield a strictly 2-D flow geometry.

3.3.1 Comparison of the Rectangular Channel Series Solution to the 2-D Flow Parabolic Solution

For pressure driven flows within round capillaries, a steady, laminar and fully-developed flow would produce a paraboloidal flow field. If a cross section of the flow is taken along the diameter of the capillary, a parabolic velocity profile results. For flow in rectangular channels, cross sections of the flow field along the X-Z plane (refer to Figure 3-2) also produce parabolic profiles but as the side walls ($y=\pm 12.7$mm) are approached, the velocity profile starts to deviate. This causes a change in the velocity gradient (slope, 1/s) at the wall. This is shown in Figure 3-9 where around 0.2mm from the edge of the microchannel, the series solution starts to deviate from the parabolic profile. It is worth noting that the the numerical computation of the series solution is the exact solution of the flow field within a rectangular channel. However, since the series solution in the "central" region ($-12.2\text{mm} < y < 12.2\text{mm}$) of the microchannel matches the parabolic profile so well, the parabolic profile is used to obtain the friction factor in our experimental data sets. All the experimental data in this study were obtained from this "central" region. At 1mm from the side wall, the percentage change in slope is only 0.03% from the centerline. Another technique of obtaining the friction factor without the assumption of a parabolic profile is also employed and is described later. If the

experimental data were obtained closer to the walls (< 1mm), the actual numerically computed velocity profile at that interrogation location would be used instead.

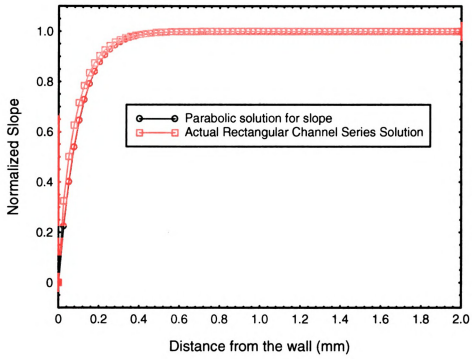

Figure 3-9 Comparison of parabolic profile solution to the numerical computation of the series solution

3.3.2 Determination of Friction Factor from Experiments

Experiments with pressure driven flows were performed with a microchannel fabricated from quartz flats resulting in a channel width of 25.4mm and a channel height of approximately 300μm. The flow facility was shown in Figure 2-9. Using the MTV technique, a single laser line was used to "tag" the MTV chemical across the 300μm height of the microchannel and its phosphorescence is tracked in time to obtain velocity information. The images in Figure 3-10 illustrate the initial phosphorescence image and the corresponding delayed image 3ms later (images are averages of 100

images). The width of the laser line in this case is 30μm (full width at half maximum) and the interrogation region is y = 3mm from the side wall (y-axis, refer to Figure 3-2). A correlation procedure, as described previously was used to process the images and obtain velocity information. The central region of the tagged fluid is thicker due to the higher velocities present in the center of the channel and the long exposure times. This could be reduced by lowering the exposure time at the expense of lower intensities in the images. The size of the microchannel can be accurately determined because of the reflection of the tagged fluid.

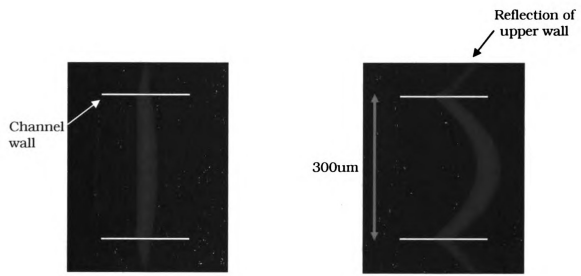

Figure 3-10. Images of tagged molecules for pressure driven flows.

Figure 3-11 illustrates the velocity profile obtained from the correlation of Figure 3-10. The data points near the wall are seen to deviate from zero velocity as the poor signal to noise near the walls resulted in 2-4 (~2μm/pixel) pixels of unreliable data. However, by curve fitting the rest of the data to a parabolic curve, and extrapolating based on the channel height, a nominally zero velocity was obtained at the walls.

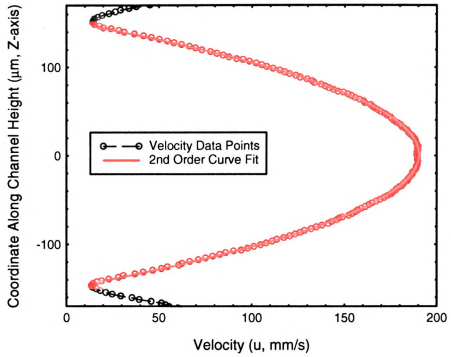

Figure 3-11 Velocity profile from correlation of initial and delayed images

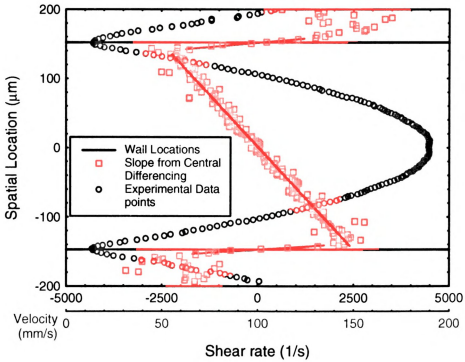

Figure 3-12 Central Differencing Technique for obtaining Slope

There are two ways to obtain the local friction factor from the experimental data set. The first technique involves fitting a parabolic curve and obtaining the velocity gradient at locations of zero velocity. This however assumes the no-slip condition at the wall. The derivation of slip velocity and the limitations of the current technique to measure slip will be described in a later section. The second technique involves determining the slope directly from the data. A 1st order central differencing procedure was performed on the data points to obtain the slope. The key idea of this technique is to utilize the reflection at the walls to determine the location of the walls and hence the slope at that location. This is illustrated in Figure 3-12.

Linear curves (blue lines) are fitted to the data points near the reflection and the location of zero slope (change of sign) is taken to be the location of the wall; illustrated by the green horizontal lines in Figure 3-12. Another linear curve (black line) is fitted to the central region of the slope data and is extrapolated to intersect with the green horizontal lines to obtain the slope at the walls. One advantage of this technique is that no assumption about wall slip needs to be made *a priori*. The two techniques were compared and differences of less than 0.5% in the friction factor resulted. A discussion of the uncertainties in the measurements is provided in Appendix M.

3.3.3 Experimental Results for Non-Coated Quartz Microchannels

The first data set for pressure driven flows was obtained with the setup as shown in Figure 2-9 where the pressure gradient is varied by gravitational forces. This resulted in measurements with Reynolds numbers in the range of 11.23 - 84.12 where the Reynolds number was determined from the mean velocity at the interrogation location and the hydraulic diameter as the characteristic length.

Re #: 11.23
Undelayed (0.3ms Exposure)

Re #: 11.23
Delayed 2ms (0.3ms Exposure)

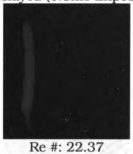

Re #: 22.37
Undelayed (0.3ms Exposure)

Re #: 22.37
Delayed 2ms (0.3ms Exposure)

Re #: 32.84
Undelayed (0.3ms Exposure)

Re #: 32.84
Delayed 2ms (0.3ms Exposure)

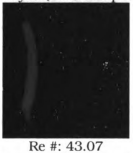

Re #: 43.07
Undelayed (0.3ms Exposure)

Re #: 43.07
Delayed 2ms (0.3ms Exposure)

Re # 53.22
Undelayed (0.3ms Exposure)

Re #: 53.22
Delayed 2ms (0.3ms Exposure)

Re #: 63.89
Undelayed (0.2ms Exposure)

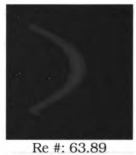

Re #: 63.89
Delayed 1ms (0.2ms Exposure)

Re #: 74.11
Undelayed (0.2ms Exposure)

Re #: 74.11
Delayed 1ms (0.2ms Exposure)

Re #: 84.12
Undelayed (0.2ms Exposure)

Re #: 84.12
Delayed 1ms (0.2ms Exposure)

Figure 3-13. Images of tagged fluid for different flow velocities for uncoated microchannels

For the Reynolds number range of 11.23 – 53.22, the images were taken with an exposure time of 0.3ms and a delay of 2ms. From Reynolds number of 63.89 - 84.12, a 0.2ms exposure and a 1ms delay was used. The use of shorter delays is warranted to minimize the amount of pixel displacement while the lower exposure time is used at higher velocities to minimize broadening of the tagged fluid. Note that the thicker central region of the tagged fluid is not caused by dispersion but by the long exposure time and the higher velocities in the center of the microchannel. Blemishes apparent on the images are caused by dead pixels and dirt on the front face of the microchannel.

This affected the correlation procedure as apparent in the red curve (Re #: 43.07) in Figure 3-14 where a bump in the profile can be seen (highlighted by an arrow). This caused a slight under prediction of the velocity for all the curves in the figure at the approximate wall location of -70μm. This is illustrated by an arrow in the figure.

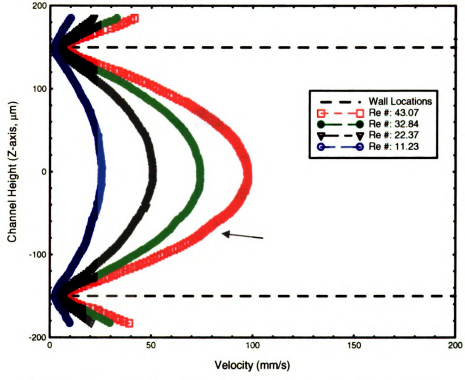

Figure 3-14. Velocity profiles at different Reynolds numbers (Re #: 11.23 - 43.07)

However, when a parabolic curve was fitted to the data points, the general trend of the curve is negligibly affected by the anomaly. The velocity profiles for all the different flow rates are shown in Figure 3-14 and Figure 3-15.

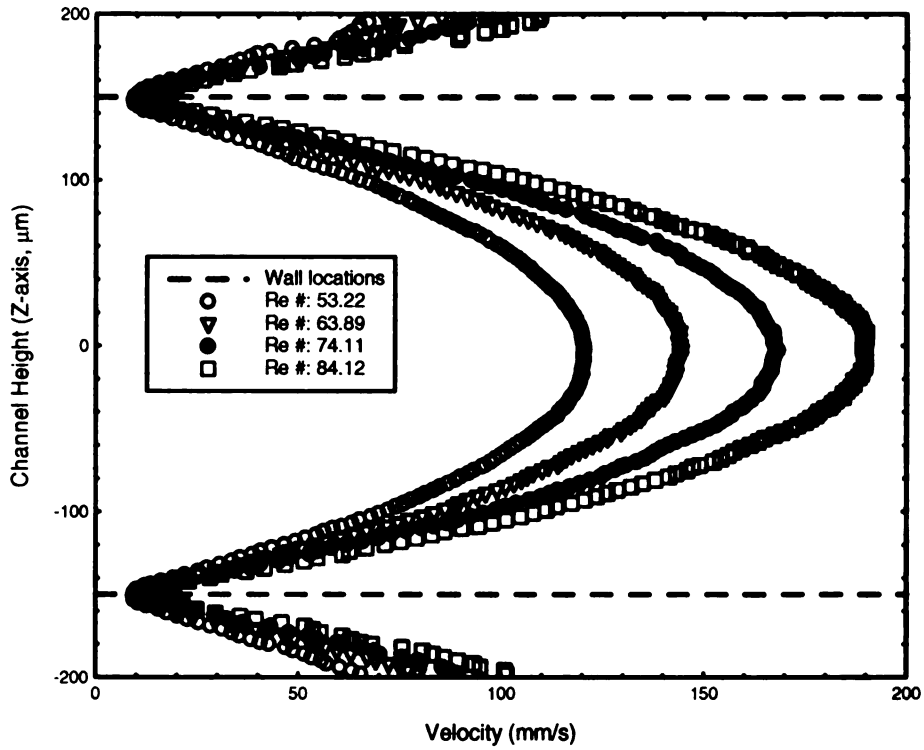

Figure 3-15. Velocity profiles at different Reynolds numbers (Re #: 53.22-84.12)

The imaging system has difficulties resolving the fine detail near the wall due probably to parallax issues. This causes the velocity to have an apparent non-zero value at the walls. As the velocity increases, the data points at the walls seem to measure a higher non-zero velocity. This is an artifact of the imaging issues and could potentially be improved upon by using a higher magnification objective for imaging near the walls. A parabola is curve fitted to the rest of the data points away from the wall and extrapolated to the location of the walls to obtain the slope and thus the friction factor.

Table 3-1 details the experimental results obtained from the correlated images. The fit coefficients for the parabolic curve fit for all the data sets are shown and the "lower" and "upper" positions designate the wall locations. The two techniques described in § 3.3.2 are then used to obtain the slope (shear rates) at the wall locations. Minimal deviations were observed and the easier technique of fitting a parabolic curve to the data points is henceforth used.

Experimental data														
		Coefficients of Parabolic Fit			Wall Position		Channel Thickness (μm)	Slope		Location of Umax	Umax (mm/s)	mean vel(m/s)	$C_{f,exp}/C_{f,theory}$	Uncertainty in $C_{f,exp}/C_{f,theory}$
Re_{CH} (hydraulic diameter)	Re_{DH} (hydraulic diameter)				Lower Position (mm)	Upper Position (mm)		Lower Wall	Upper Wall					
5.66	11.23	-1113	404	-11.2	0.0302	0.3327	302.5	336.7	-336.7	0.181	25.46	0.017	0.995	0.00725
7.07	14.04	-1401	510	-14.6	0.0313	0.3327	301.4	422.2	-422.2	0.182	31.81	0.021	0.998	0.00582
8.43	16.73	-1672	605	-16.8	0.0303	0.3315	301.2	503.7	-503.7	0.181	37.93	0.025	0.999	0.00488
9.86	19.57	-1942	706	-19.8	0.0306	0.3329	302.3	587.1	-587.1	0.182	44.37	0.029	0.995	0.00416
11.27	22.38	-2221	806	-22.4	0.0303	0.3326	302.2	671.3	-671.3	0.181	50.72	0.034	0.996	0.00364
12.61	25.05	-2515	912	-25.9	0.0311	0.3316	300.5	755.8	-755.8	0.181	56.78	0.038	1.001	0.00327
13.96	27.72	-2760	1002	-28.1	0.0306	0.3324	301.8	832.9	-832.9	0.182	62.84	0.042	0.997	0.00294
15.23	30.24	-3036	1100	-31.1	0.0309	0.3314	300.5	912.3	-912.3	0.181	68.54	0.045	1.001	0.00271
17.84	35.43	-3550	1289	-36.7	0.0311	0.3320	300.8	1067.9	-1067.9	0.182	80.31	0.053	1.000	0.00231
19.12	37.96	-3803	1382	-39.5	0.0313	0.3321	300.9	1144.1	-1144.1	0.182	86.05	0.057	1.000	0.00216
20.35	40.42	-4050	1474	-42.5	0.0316	0.3324	300.8	1218.3	-1218.3	0.182	91.62	0.061	1.000	0.00203
21.69	43.07	-4310	1567	-44.8	0.0313	0.3323	301.0	1297.4	-1297.4	0.182	97.63	0.065	1.000	0.00190
24.35	48.36	-4803	1749	-49.6	0.0310	0.3331	302.2	1451.2	-1451.2	0.182	109.62	0.073	0.996	0.00168
25.5	50.64	-5071	1841	-52.3	0.0311	0.3320	300.9	1525.9	-1525.9	0.182	114.79	0.076	1.000	0.00162
26.8	53.22	-5317	2078	-82.4	0.0448	0.3460	301.3	1601.7	-1601.7	0.195	120.63	0.080	0.999	0.00154
28.1	55.79	-5616	2199	-88.8	0.0457	0.3458	300.1	1685.5	-1685.5	0.196	126.46	0.084	1.003	0.00147
30.79	61.15	-6117	2400	-96.8	0.0456	0.3467	301.1	1841.6	-1841.6	0.196	138.61	0.092	1.000	0.00134
22.48	66.48	-6625	2603	-105	0.0456	0.3473	301.6	1998.3	-1998.3	0.196	150.68	0.100	0.998	0.00123
24.86	69.21	-6890	2707	-109	0.0455	0.3473	301.8	2079.4	-2079.4	0.196	156.89	0.104	0.997	0.00118
36.17	71.83	-7177	2819	-114	0.0458	0.3470	301.2	2162.0	-2162.0	0.196	162.81	0.108	0.999	0.00114
38.55	76.54	-7610	2989	-120	0.0454	0.3474	302.0	2298.1	-2298.1	0.196	173.50	0.115	0.996	0.00107
39.54	78.51	-7863	3097	-127	0.0465	0.3474	300.9	2365.8	-2365.8	0.197	177.95	0.118	1.000	0.00104
42.36	84.12	-8350	3288	-133	0.0458	0.3480	302.2	2523.6	-2523.6	0.197	190.68	0.126	0.996	0.00097
44.74	88.85	-8887	3504	-144	0.0466	0.3477	301.1	2675.7	-2675.7	0.197	201.39	0.133	1.000	0.00092

Table 3-1. Experimental data for pressure driven flows in non-coated microchannels with Reynolds number based on hydraulic diameter

One disadvantage of using a high aspect ratio microchannel is that the hydraulic diameter, D_H, is biased by the width of the channel and the Reynolds number computed from the hydraulic diameter (Re_{DH}) may not be representative. Table 3-1 adds a column for Reynolds number computed from the characteristic height (Re_{CH}, 301.4μm) and this results in a Reynolds number range that is about a factor of 2 lower than that computed previously. The differences are illustrated in Figure 3-16.

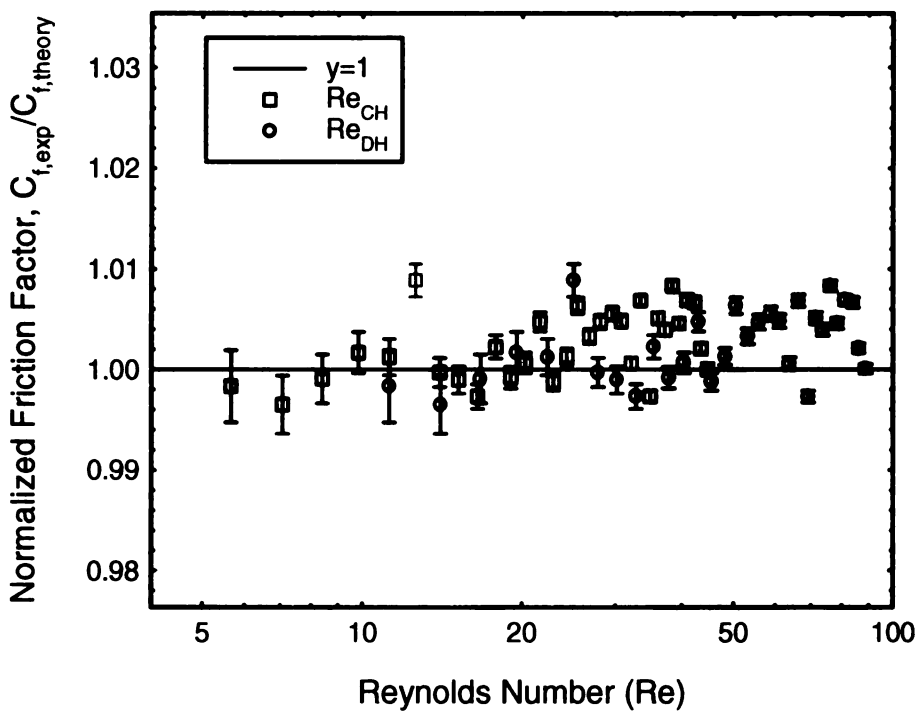

Figure 3-16 Normalized friction factor based on definitions of Reynolds number.

3.3.4 Extended Range of Re # for Non-Coated Microchannels

More experiments were performed with the non-coated microchannels to try and extend the range of the Reynolds number. From our experiments, as the Reynolds number becomes lower, the amount of displacement achievable while maintaining sufficient signal to noise becomes smaller. Due to the reduced signal to noise at long

delay times, a Reynolds number, Re_{DH} lower than 0.32 was not achievable. A representative set of images is shown in Figure 3-17 and by correlating the images, the velocity profiles are obtained. The velocity profiles for the lowest Reynolds numbers are shown in Figure 3-18. Note that from Figure 3-17, the images for a Reynolds number of 0.32 had very small displacements (1 pixel or less) and this contributed to the level of noise when the images were correlated. This effect is demonstrated in the normalized friction factor shown in Table 3-2. Comparing the normalized friction factor in Table 3-2 to Table 3-1, a noticeable difference in friction factor is present. At the lowest Reynolds number, the deviation from a normalized friction factor of 1 is higher.

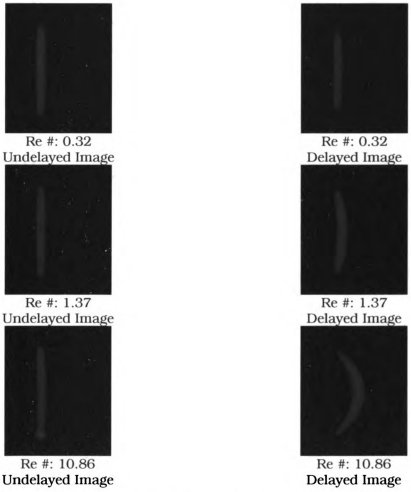

Figure 3-17. Images of tagged fluid for different flow velocities (Re # : 0.32-10.86)

Velocity profiles obtained from the different images in Figure 3-17 are shown in Figure 3-19. One of the differences with this set of data is the interrogation location (1mm from the side wall) and the shorter reflection at the upper and lower walls. The closer the interrogation region is to the side walls, the shorter the reflection will be. However, the intensity of the images increases due to a shorter path length.

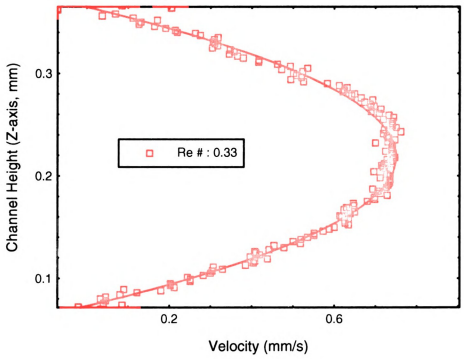

Figure 3-18 Plot of velocity at different pressure gradients (Re #: 0.33)

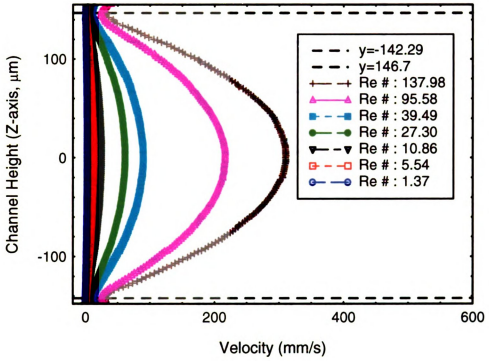

Figure 3-19. Plot of velocity at different pressure gradients (Re #: 1.37-137.98)

	Experimental data											
	Coefficients from Parabolic Fit			Wall Position from Fit		Channel Thickness (μm)	Slope		Location of Umax	Umax (mm/s)	Umax (m/s)	mean vel(m/s)	$C_{f,exp}/C_{f,theory}$
Re_{DH}	a	b	c	Lower Position (mm)	Upper Position (mm)		Lower Wall	Upper Wall					
0.32	-33.2	14.6	-0.88	0.0721	0.3677	295.6	9.81	-9.81	0.220	0.725	0.0007	0.00048	0.9960
0.33	-35.3	15.4	-0.934	0.0728	0.3635	290.7	10.26	-10.26	0.218	0.746	0.0007	0.00050	1.0128
1.37	-139	61.5	-3.72	0.0723	0.3701	297.8	41.40	-41.40	0.221	3.083	0.0031	0.00205	0.9884
5.54	-565	249	-15	0.0720	0.3687	296.7	167.63	-167.63	0.220	12.434	0.0124	0.00827	0.9922
10.86	-1104	486	-29.1	0.0715	0.3687	297.2	328.16	-328.16	0.220	24.386	0.0244	0.01622	0.9904
27.30	-2790	1231	-74.5	0.0724	0.3688	296.4	827.01	-827.01	0.221	61.285	0.0613	0.04075	0.9931
39.49	-4001	1765	-106	0.0717	0.3694	297.7	1191.13	-1191.13	0.221	88.653	0.0887	0.05895	0.9888
95.58	-9882	4354	-265	0.0729	0.3677	294.7	2912.46	-2912.46	0.220	214.592	0.2146	0.14270	0.9989
137.98	-14200	6300	-389	0.0741	0.3695	295.4	4194.62	-4194.62	0.222	309.768	0.3098	0.20598	0.9966

Table 3-2 Experimental data for pressure driven flows in non-coated microchannels with extended Reynolds number range based on hydraulic diameter.

3.3.5 Experimental Results for HEMA coated Quartz Microchannels

The experimental results for HEMA coated microchannels echo the results from the non-coated microchannels.

Re # : 2.19
Undelayed Image (1ms exposure)

Re # : 2.19
Delayed Image (5ms delay)

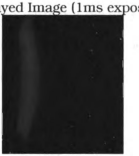

Re # : 12.93
Undelayed Image

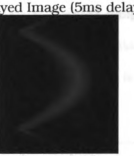

Re # : 12.93
Delayed Image

Re # : 32.59
Undelayed Image (0.5ms exposure)

Re # : 32.59
Delayed Image (2ms delay)

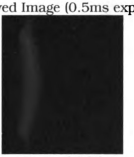

Re # : 65.05
Undelayed Image (0.2ms exposure)

Re # : 65.05
Delayed Image (1ms delay)

Figure 3-20. Images of tagged fluid for different flow velocities for HEMA coated microchannels (Re # : 2.19-65.05).

The image pairs obtained from the experiments are illustrated in the Figure 3-20.

The images in Figure 3-20 are slightly different in appearance from previous line tagging images. Due to the different intensity variations, some images illustrate a thicker tagged line in the middle due to the higher exposure times. Another aspect of the tagged lines which is also inherent in the previous set of images is the curvature present in the undelayed images. The curvature becomes more apparent as the flow velocity increases. This is caused by the amount of delay between the firing of the laser and the time when the image was taken. If the delay is reduced, this effect will also be reduced. However, since the velocity correlation technique is based on the correlation of the undelayed with the delayed image, the curvature of the undelayed image did not cause any problems with the correlation technique. The velocity profiles obtained from the pair of images are shown in Figure 3-21. The full experimental data set is shown in Table 3-3.

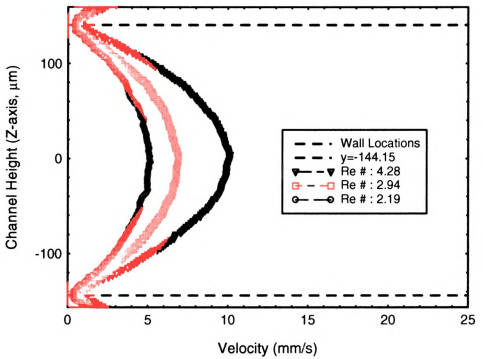

Figure 3-21 Plot of velocity at different pressure gradients for HEMA coated microchannels (Re #: 2.19-4.28).

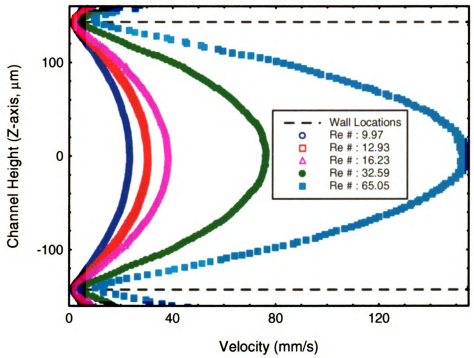

Figure 3-22. Plot of velocity at different pressure gradients for HEMA coated microchannels (Re #: 9.97-65.05).

Experimental data for HEMA Coated Microchannel													
				Wall Position			Slope						
Re_{DH}	Coefficients of Parabolic Fit			Lower Position (mm)	Upper Position (mm)	Channel Thickness (μm)	Lower Wall	Upper Wall	Location of Umax	Umax (mm/s)	Mean velocity (m/s)	$C_{f,exp}/C_{f,theory}$	Uncertainty in $C_{f,exp}/C_{f,theory}$
65.05	-7359	3431	-247	0.0890	0.3773	288.3	2121.57	-2121.57	0.233	152.910	0.101	1.0033	0.00024
32.59	-3685	1711	-122	0.0880	0.3763	288.4	1062.66	-1062.66	0.232	76.611	0.051	1.0031	0.00047
16.23	-1845	855	-60.9	0.0879	0.3755	287.6	530.64	-530.64	0.232	38.155	0.025	1.0057	0.00094
12.93	-1465	654	-42.6	0.0792	0.3672	288.1	422.00	-422.00	0.223	30.389	0.020	1.0042	0.00118
9.97	-1132	506	-33.1	0.0796	0.3674	287.8	325.82	-325.82	0.223	23.445	0.016	1.0050	0.00154
4.28	-477	212	-13.5	0.0770	0.3674	290.4	138.51	-138.51	0.222	10.056	0.007	0.9961	0.00355
2.94	-321	141	-8.57	0.0729	0.3664	293.5	94.22	-94.22	0.220	6.914	0.005	0.9855	0.00511
2.19	-243	107	-6.63	0.0746	0.3657	291.1	70.74	-70.74	0.220	5.149	0.003	0.9936	0.00691

Table 3-3. Experimental data for pressure driven flows in HEMA coated microchannels with extended Reynolds number range based on hydraulic diameter.

3.3.6 Experimental Results for OTS coated Quartz Microchannels

For the OTS coated quartz microchannels, a similar experimental procedure was performed. Notice that the tagged fluid in Figure 3-23 and Figure 3-24 exhibits a thinner region in the middle of the microchannel. The laser beam is at its focal point in the middle of the microchannel which caused the narrower beam. An artifact of a more focused beam is the higher energy levels present which cause bleaching effects.

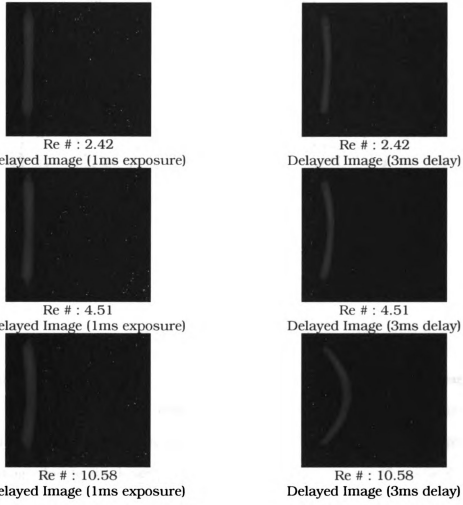

Figure 3-23. Images of tagged fluid for different flow velocities for OTS coated microchannels (Re # : 2.42-10.58).

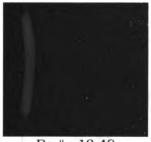

Re # : 13.48
Undelayed Image (1ms exposure)

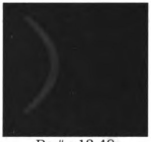

Re # : 13.48
Delayed Image (3ms delay)

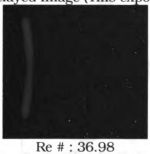

Re # : 36.98
Undelayed Image (0.3ms exposure)

Re # : 36.98
Delayed Image (1ms delay)

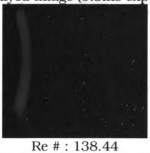

Re # : 138.44
Undelayed Image (0.1ms exposure)

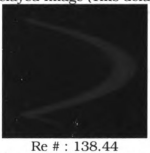

Re # : 138.44
Delayed Image (1ms delay)

Figure 3-24. Images of tagged fluid for different flow velocities for OTS coated microchannels (Re # : 13.48-138.44).

This is illustrated in Figure 3-24 where the central region of the tagged fluid has a lower intensity. The intensity levels, however, were sufficient in performing the velocity correlation. The last image set in Figure 3-24 illustrates a thicker central region in the delayed image due to the longer exposure time necessary for a good signal to noise ratio. This is not caused by dispersion.

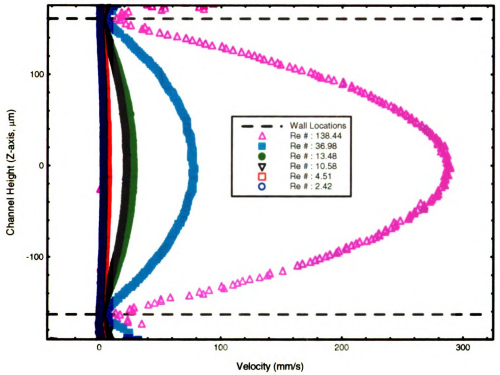

Figure 3-25. Plot of velocity at different pressure gradients for OTS coated microchannels (Re #: 2.42-138.44).

The images from Figure 3-24 are correlated to obtain the velocity profile for each individual syringe pump setting. These velocity profiles are shown in Figure 3-25 and illustrate a representative set of the data taken for this experimental setup. The full experimental data set is provided in Table 3-4 and illustrates similar results obtained for the non-coated and HEMA coated microchannels. The normalized friction factor displays excellent agreement with classical theory. The normalized friction factor for all the different surfaces is plotted against the results from other researchers and is shown in Figure 3-26. A zoomed-up view of the experimental results is provided in Figure 3-27 along with the calculated error bars. The error bars signify the uncertainties in determining the friction factor.

Experimental data for OTS Coated Microchannel													
	Coefficients of Parabolic Fit			Wall Position From Fit		Channel Thickness (μm)	Slope		Location of Umax	Umax (mm/s)	Mean velocity (m/s)	$C_{f,exp}/C_{f,theory}$	Uncertainty in $C_{f,exp}/C_{f,theory}$
Re_{DH}	a	b	c	Lower Position (mm)	Upper Position (mm)		Lower Wall	Upper Wall					
138.44	-10800	5229	-344	0.0785	0.4056	327.1	3532.9	-3532.9	0.242	288.927	0.191	0.999	0.0003
69.82	-5470	2848	-225	0.0971	0.4235	326.4	1785.5	-1785.5	0.260	145.709	0.096	1.001	0.0006
36.98	-2897	1500	-117	0.0957	0.4221	326.4	945.6	-945.6	0.259	77.166	0.051	1.001	0.0011
17.36	-1349	697	-54	0.0945	0.4222	327.8	442.2	-442.2	0.258	36.231	0.024	0.997	0.0024
13.48	-1058	544	-42	0.0940	0.4201	326.1	345.0	-345.0	0.257	28.128	0.019	1.002	0.0031
10.58	-833	428	-33	0.0941	0.4197	325.6	271.2	-271.2	0.257	22.077	0.015	1.003	0.0039
7.63	-597	308	-24	0.0946	0.4213	326.7	195.0	-195.0	0.258	15.925	0.011	1.000	0.0054
4.51	-352	180	-14	0.0922	0.4192	327.0	115.1	-115.1	0.256	9.411	0.006	0.999	0.0091
3.10	-244	125	-9.6	0.0934	0.4189	325.4	79.4	-79.4	0.256	6.459	0.004	1.004	0.0134
2.42	-188	95.9	-7.2	0.0912	0.4189	327.8	61.6	-61.6	0.255	5.050	0.003	0.997	0.0170
1.62	-126	63.7	-4.7	0.0887	0.4168	328.1	41.3	-41.3	0.253	3.391	0.002	0.996	0.0253

Table 3-4. Experimental data for pressure driven flows in OTS coated microchannels with extended Reynolds number range based on hydraulic diameter.

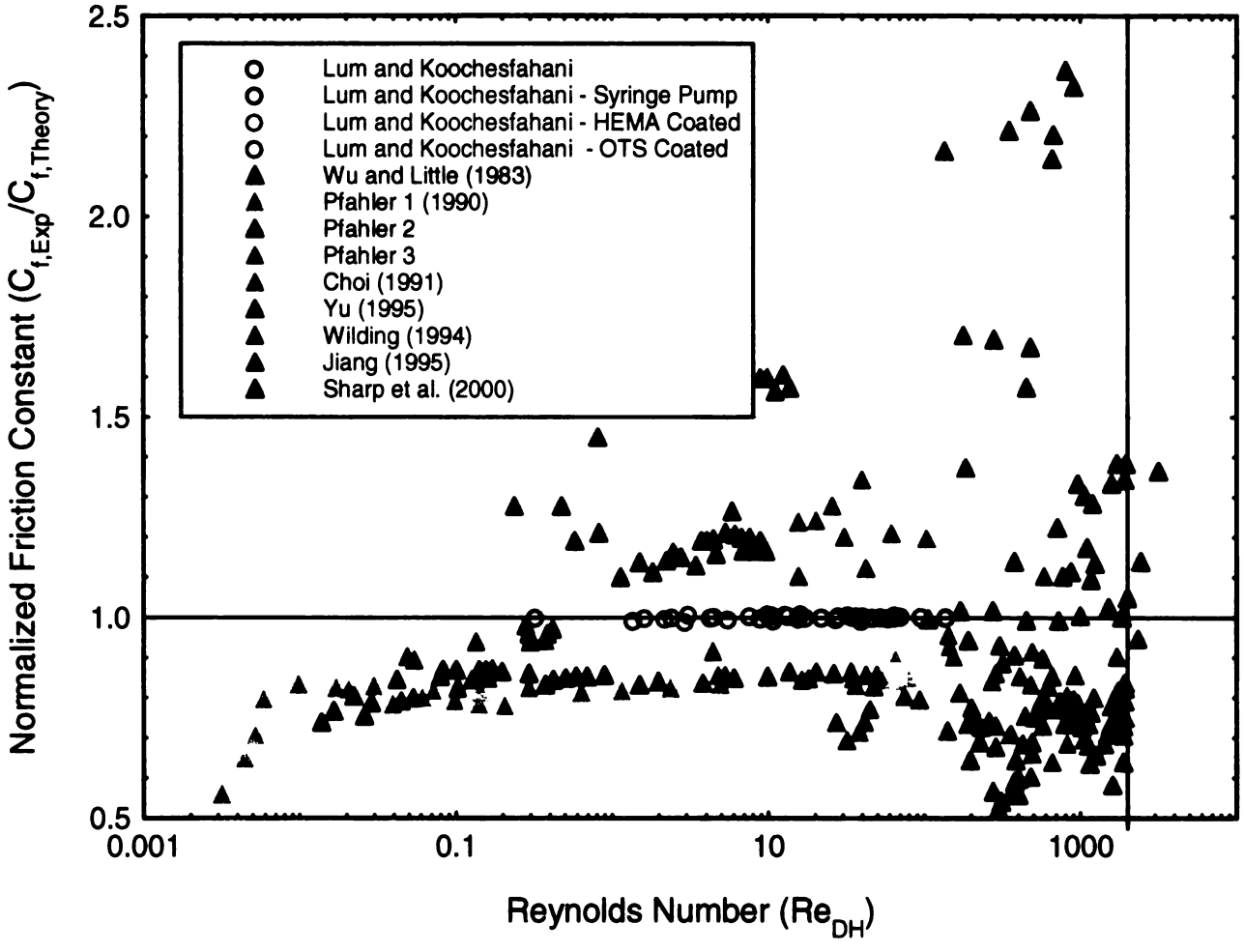

Figure 3-26. Comparison of normalized friction factor (Sharp et. al., 2000) to friction factor obtained from experimental results for uncoated, OTS-coated and HEMA-coated quartz.

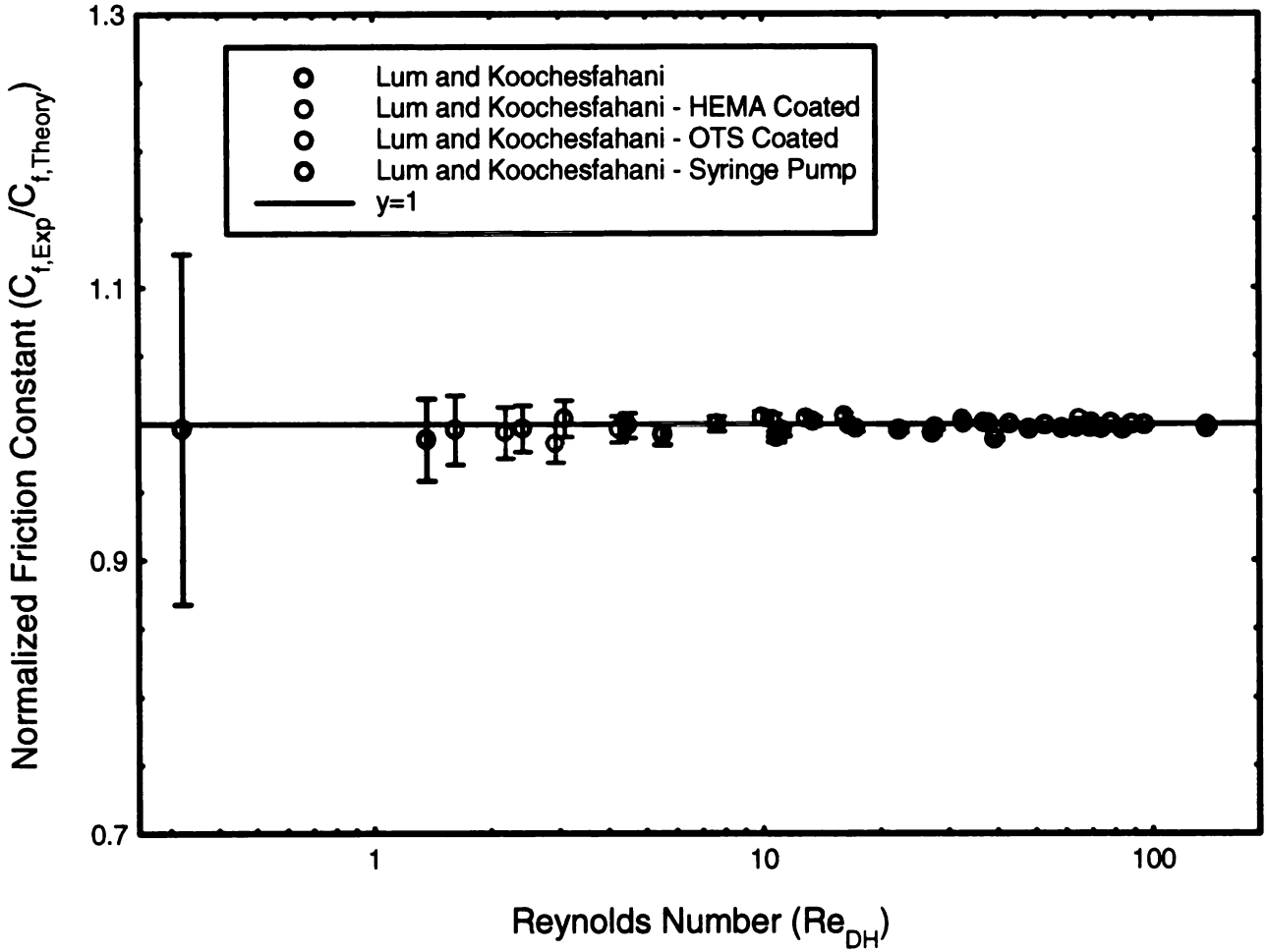

Figure 3-27. Zoomed-in view of normalized friction factor

3.3.7 Limit of Slip Detection

The possibility of fluid slip at a boundary was proposed by Navier in 1823. The slip velocity at the boundary is assumed to be proportional to the shear stress at the surface. This is shown in equation 3-23 where β is the slip length and u_x is the slip velocity.

$$u_x = \beta \frac{du_x}{dz} \qquad 3\text{-}23$$

Results from Tretheway et. al. (2002) reported a slip length as large as 1μm for fluid flows within a 30μm x 300μm microchannel coated with OTS. The measurements were made using fluorescent particles 300nm in diameter with the velocity profile measured along the 300μm height of the microchannel with an integrated depth of 30μm. From the experimental results presented in previous sections for pressure driven flows within microchannels with different coatings, the normalized friction factor yielded a deviation from theory of only $\pm$ 0.5%. It is thus of interest to investigate the slip detection limit of the in-situ measurement techniques that were applied in comparison with the reported 1μm slip length.

In the presence of slip within a microchannel an offset is imposed on the parabolic flow profile (derivation of the equations are presented in Appendix L). For a 1μm slip length, a wall velocity with a magnitude of 1.325% of peak velocity is observed (Figure 3-28). In order to understand the slip detection limit of the in-situ measurement technique, the error margin from the experimental results is used as a starting point. Although the errors were obtained for the normalized friction factor measurements (the slip imposes an offset and there is no change in shear stress although the friction factor will decrease due to a higher mean velocity), the errors from the measurements are an indication of how well the technique can resolve differences in velocity near the wall.

Figure 3-29 is a more detailed version of Figure 3-12 and is used to illustrate how the error margin is utilized to obtain the slip detection limit.

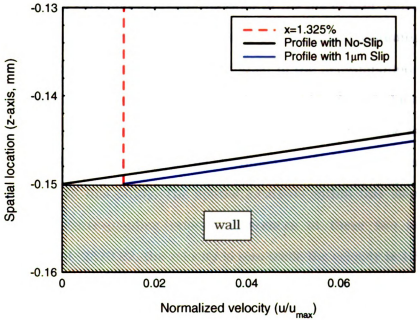

Figure 3-28. Comparison of theoretical velocity profiles near the wall with and without slip

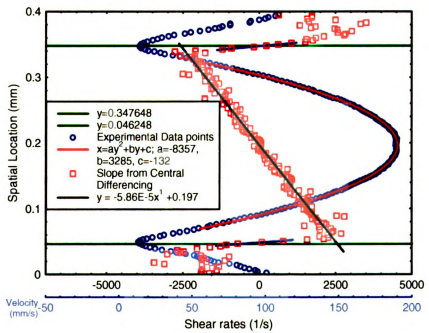

Figure 3-29. Central differencing technique for obtaining slope

The linear curve fit (black line) in Figure 3-29 is used to obtain the slope at the wall and the upper wall is taken as an example. The wall location (347.7μm) is plugged into the linear curve fit equation to obtain the slope at the upper wall. Since the friction factor measurements typically yield an uncertainty of < 0.5% and assuming that in the worst case scenario that all the errors are attributed to the determination of the slope (although in reality, the uncertainty of 0.5% is cause by the combination of the uncertainty in determination of the wall locations and the fit), the slope at the wall is determined to be -2570.82 ± 12.85 1/s. The shearing rate of 2570.82 1/s is the highest shear rate measured in this study. The spatial locations within this slope range are determined and the corresponding velocity differences at these two locations are compared. At a slope of -2570.82, the velocity is zero while the velocity is 1.897mm/s at a slope of (-2570.82+12.85). Note that this uncertainty in velocity is dependent on the gradients at the wall (higher gradients will result in a higher uncertainty in velocity). Since the minimum shift in velocity that can be measured is 1.897mm/s in this case, it translates to a minimum detectable slip length of 752nm. This value, however, is close to the reported value of 1μm by Trethaway et. al. (2002) and it is inconclusive if the present technique will be able to resolve the slip lengths.

3.3.8 Electroviscous Effects

The electroviscous effect is based on the presence of ions in a fluid made to move relative to a charged surface by an induced pressure gradient. For a charged surface, ions of opposite charge to the surface are preferentially attracted to it. A pressure gradient within the microchannel would tend to move the ions near the walls and thus create a streaming potential. This potential opposes the motion of the fluid in the direction of the pressure gradient by inducing back conduction by ion diffusion and

electroosmotic flow (Probstein, 1994). The resultant pressure driven flow would effectively demonstrate a higher 'viscosity' due to this added resistance.

The streaming potential created is limited to the interaction between the Debye layer and the charged surface. The Debye layer is a layer primarily composed of ions opposite in charged to the surface (more details in § 4.3.1) and is usually on the order of less than 100nm. Rice and Whitehead (1965) consider the electroviscous effect to be negligible when $k >> 1$ where k is the ratio of the capillary radius to the Debye layer thickness. Brutin and Tadrist (2003), however, measured discrepancies with classical Poiseuille flow for capillaries as large as 539.69μm and attributed it to electroviscous effects. Note that the k value is 13,500 which is expected to have negligible electroviscous effects. The experimental data illustrated in the present study for pressure driven flows have been shown to be highly consistent with classical theory and no discrepancies have been found for microchannels 300μm in height. This further proves that discrepancies from classical theory at this level are highly unlikely.

3.3.9 Contributions and Conclusions

The present study illustrates a marked improvement over previous diagnostic techniques used by other researchers (Maynes et. al. (2002) and Sharp et. al. (2000)) to measure flow characteristics within microchannels. Maynes et. al (2002) utilized the MTV technique to measure the velocity profile within a 705μm diameter capillary but the quality of the images were not sufficient to resolve the velocity gradients at the walls. Surface curvature issues of the round capillaries used in their study also impeded the measurements at the walls. Multiple smoothing algorithms were needed to improve the signal to noise characteristics of the images but were only used to yield flow rate information. Sharp et. al (2000) also measured the flow rate but utilized a particle

tracking technique instead. Although these measurement techniques were local in nature, it was used to measure bulk flow properties. The implementation of the MTV technique in this study, however, managed to resolve the velocity profiles near the channels walls to provide a local measurement of friction factor that is not contaminated by entrance effects.

Apart from an improvement in the measurement technique, one obvious discrepancy between local measurements (Maynes et. al. (2002), Sharp et. al. (2000) and the present study) and bulk flow measurements are deviations from classical theory. Other researchers (Wu and Little (1983), Pfahler (1990), Choi (1991), Wilding (1994), Yu (1995), Jiang (1995)) have advocated a deviation from classical theory within microchannels as large as 500μm in size under high shearing rates (~2000 1/s). Various reasons for the deviations that were proposed include increased roughness, electroviscous effects, entrance effects, an early transition to turbulence and inaccuracies in measuring the dimensions of the channel.

This study, however, has proven conclusively that at similar shearing rates and even with hydrophobic microchannels 300μm in size, classical theory still holds. One of the primary advantages in this study is the ability of the experimental technique to measure the velocity profiles locally. This essentially removes the contribution of entrance effects and any uncertainties of the dimensions of the microchannel. Thus more accurate measurements of the velocity gradients are possible. The accuracy of this measurement is also utilized to determine the limit of slip detectability. The analysis showed that a minimum slip length of 752nm is detectable. It is concluded that slip lengths of > 752nm were not measured in the present study. Previously reported slip lengths of 1μm by Trethaway et. al. (2002) may have been caused by the interaction between the tracer particles used for velocity measurements and the microchannel walls.

3.3.10 Future Work

Currently, the measured velocity profiles have unreliable data points near the walls. This is due to the combination of the large physical size of a pixel and the thickness of the laser line. To be able to use a higher magnification objective to resolve the velocity profile close to the walls, a diffraction grating can be used to create fringes and use it for tagging the fluid. The fringes are expected to be much thinner than the tagging lines used in the present study. This is expected to provide a more resolved velocity profile. Another plausible technique for measuring slip lengths at these scales is a combination of the MTV technique with total internal reflection (TIR).

As the mean velocity of the measured velocity profiles increases, the "measured" velocity at the wall seems to increase accordingly. This is an artifact of the measurement technique as it is not able to resolve at sub-pixel levels. However, this value may be an indication of the increase in shearing rates as the mean velocity increases. A closer look at this problem may yield a novel way of measuring shearing rates.

Chapter 4 Electroosmotic-Flow in Microchannels

Microchannels experience large pressure drops as the large surface to volume ratio causes an increased frictional resistance to fluid movement. To create a flow speed comparable to macro flow phenomena within microchannels would require a prohibitive amount of pressure. Microchannels in the tens of microns in diameter would require an alternative method of fluid transport. An elegant way of moving fluid within microchannels, albeit not without its own challenges, is through electroosmosis. Electroosmosis is the movement of an ionized fluid relative to a charged channel due to an induced electric potential. The Helmholtz-Smoluchowski equation is used to relate the electric potential, E_x, to the resultant velocity field, u_x, and is given in the following equation.

$$u_x = \frac{\varepsilon_o \varepsilon_r \zeta E_x}{\mu} \qquad 4\text{-}1$$

where ε_o is the permittivity of vacuum given by a constant, ε_r is the relative permittivity of the fluid, ζ is the zeta potential and μ is the viscosity. For a given fluid temperature, the electroosmotic velocity linearly increases with electric potential. A by-product of moving fluid with electroosmosis, however, is Joule heating. As electroosmosis progresses, the temperature of the fluid increases which causes the relative permittivity and viscosity to change (the temperature dependence of these properties will be discussed later). A higher electric potential also causes a higher heating rate. This causes a non-linear increase in electroosmotic velocity. To correctly determine the electroosmotic velocity dependence on electric potential, the temperature and velocity of the flow needs to be measured simultaneously to account for changes of the fluid properties. Thus, the Molecular Tagging Velocimetry and Thermometry (MTV&T) technique is simultaneously applied to the measurement of electroosmotic flows within microchannels. The time evolution study of electroosmotic velocity is

presented in § 4.3.4. An added advantage of being able to measure temperature and velocity simultaneously is the determination of the zeta potential dependence on temperature. This is illustrated in § 4.3.5.

Due to the constraints of the experimental setup, the imaging system can only image the center of the channel. As electroosmosis causes heating of the fluid within the microchannel, it is of interest to determine the temperature profile within the entire microchannel as it undergoes a gradual increase. This was investigated through a computational solution (FLUENT).

In the coming sections, the surface charge of quartz is initially discussed followed by its effect on the fluid adjacent to its surface. This sets the basis for discussion of the principles of electroosmosis and the variables that affect it. The equation of motion for electroosmosis is subsequently presented. This chapter concludes with results and discussions from the present work, focusing on the importance of measuring electroosmotic velocity and temperature simultaneously and the ability to indirectly measure zeta potential and its temperature dependence. The computational solution will provide further details on the temperature characteristics of electroosmosis within a microchannel.

4.1 Electric Double Layer

Most surfaces exhibit a charged surface when exposed to an aqueous polar medium (electrolyte). In the case of glass or quartz, deprotonated (lacking in protons) silanol groups (Figure 4-1) naturally occur and cause the surface to assume a negative charge. The presence of the surface charge, however, affects the ionic distribution within the electrolyte because the negatively charged surface preferentially attracts positively charged ions (counter-ions) within the fluid. Coupled with the random thermal motion of the ions, an exponential distribution of ions is exhibited near the

surface (Probstein, 1994). Figure 4-2 illustrates the distribution of counter-ions and co-ions and the corresponding potential distribution at the surface.

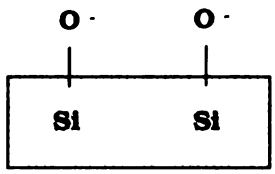

Figure 4-1. Schematic of deprotonated silanol groups

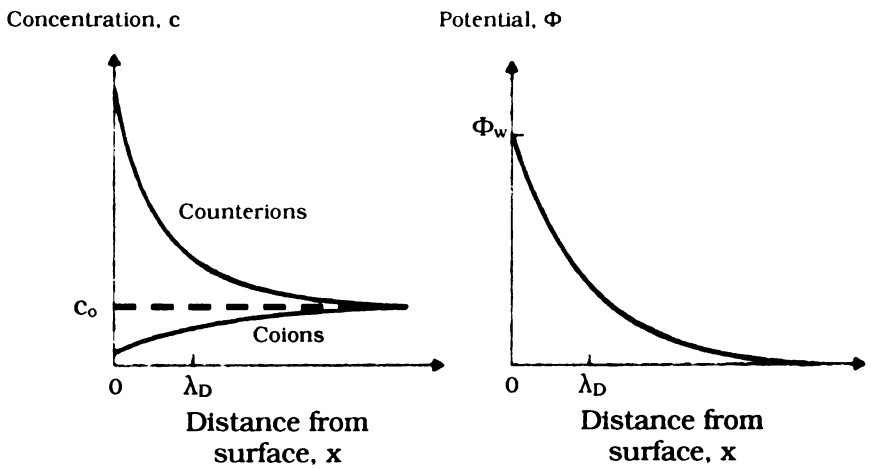

Figure 4-2. The diffuse electric double layer (Probstein, 1994)

One defining feature of the ion distribution is the Debye length (λ_D). The thickness of this layer can be estimated through the application of the Poisson equation. The electrodynamic problem may be considered electrostatic assuming that there are no magnetic fields induced by the current. The Poisson equation (equation 4-2) can thus be utilized to relate the spatial variation of the charge distribution for a medium of constant permittivity. (Probstein, 1994)

$$\nabla^2 \phi = -\frac{\rho_E}{\varepsilon} \qquad 4\text{-}2$$

where ϕ is the electric potential, ε is the permittivity and ρ_E is the electric charge density defined as

$$\rho_E = F\sum z_i c_i \qquad 4\text{-}3$$

where F is Faraday's constant, z is the charge number (valency), c is the concentration of ions and i is summed for all the ionic species in the solution. Assuming that there are no co-ions present near the surface, the Poisson equation can be simplified to equation 4-4.

$$\frac{d^2\phi}{dx^2} = \frac{Fzc}{\varepsilon} \qquad 4\text{-}4$$

where x is defined as the distance from the surface. Integrating the equation twice, the electric potential is given as

$$\phi = \frac{Fzcx^2}{2\varepsilon} \qquad 4\text{-}5$$

Note that the concentration, c is the concentration of the bulk fluid. To obtain the Debye length, the electric potential is equated to the electric potential energy per mole of counter-ions which is defined to be

$$W = -Fz\phi \qquad 4\text{-}6$$

As mentioned before, the random thermal motion of the ions caused a decaying distribution of counter-ions near the surface. At the Debye distance, the electric potential energy is approximately equivalent to the thermal energy (RT/2 per mole per degree of freedom; where R is the gas constant and T is the temperature). In a strictly 2-dimensional setting (assuming that the other dimension is uniformly distributed), the thermal energy needed to overcome the potential energy (ΔW) is RT.

$$\begin{aligned} \Delta W &= -\frac{F^2 z^2 c x^2}{2\varepsilon} \\ RT &= \frac{F^2 z^2 c x^2}{2\varepsilon} \\ x = \lambda_D &= \sqrt{\frac{2\varepsilon RT}{F^2 z^2 c}} \end{aligned} \qquad 4\text{-}7$$

In equation 4-7, it is shown that the Debye length is proportional to the square root of temperature and inversely proportional to valency and the square root of concentration. As the electrolyte increases in valency or concentration, the Debye length becomes shorter due to the increased amount of ions present to neutralize the effects of the surface charge.

4.1.1 Debye-Hückel Approximation

The estimation of the Debye length presented in the previous section from a thermal energy stand point does not yield the ion distribution near the walls. If the distribution at the wall is taken into account, the Poisson's equation would look slightly different. The ions near the surface have a Boltzmann distribution given as

$$c_{\pm} = c_o e^{\frac{\mp zF\phi}{RT}} \tag{4-8}$$

where $c \rightarrow c_o$ as $\phi \rightarrow 0$. From equation 4-3, the charge density is modified to become

$$\rho_E = zFc_o\left[e^{-\frac{zF\phi}{RT}} - e^{\frac{zF\phi}{RT}}\right]$$
$$\rho_E = -2Fzc_o \sinh\left(\frac{zF\phi}{RT}\right) \tag{4-9}$$

substituting the charge density back into equation 4-2, the Poisson equation becomes

$$\frac{d^2\phi}{dx^2} = \frac{2zFc_o}{\varepsilon}\sinh\left(\frac{zF\phi}{RT}\right) \tag{4-10}$$

For small potentials, $zF\phi << RT$ and Equation 4-6 can be simplified to become

$$\frac{d^2\phi}{dx^2} = \frac{\phi}{\lambda_D{}^2} \tag{4-11}$$

This is the *Debye-Hückel* approximation which is applicable for surfaces with small potentials. The integration of equation 4-11 with the boundary conditions of $\phi = \phi_w$ at $x=0$ and $d\phi/dx = 0$ as $x \rightarrow \infty$ results in

$$\phi = \phi_w e^{-\frac{x}{\lambda_D}} \qquad 4\text{-}12$$

This equation illustrates that the electric potential is exponentially decaying from the charged surface and the Debye length, λ_D, is the 1/e decay distance of the potential.

4.2 Principles of Electroosmosis

At the ionic level (see Figure 4-3), a single layer of ions with an opposite charge to that of the surface, called the Stern layer, is strongly attracted to the surface charge (opposite charges attract) and largely remains immobile. Beyond this layer, the Debye layer, which is a layer consisting on average of ions opposite in charge to the surface charge is present. This layer, depending on the concentration of the ionized fluid present, could range in the order of angstroms to nanometers. When an electric field is applied parallel to the negatively charged surface, the positively charged Debye layer is attracted to the negative electrode. This induces motion and through the action of viscous forces, this motion is transferred from the Debye layer to the bulk fluid (ionized but neutral). One can perceive the Stern layer as a no-slip surface and the movement of fluid above this layer to resembles a boundary layer type flow. The flow profile is described in diagram (a) of Figure 4-3. The induced motion caused by the movement of ions at the shear surface (between the Stern and Debye layers) results in a perceived "plug" flow as the Debye layer is so thin (refer to equation 4-1 for the uniform plug flow velocity). Plug flow is characterized by a uniform velocity profile across the whole microchannel. This is illustrated in Figure 4-4.

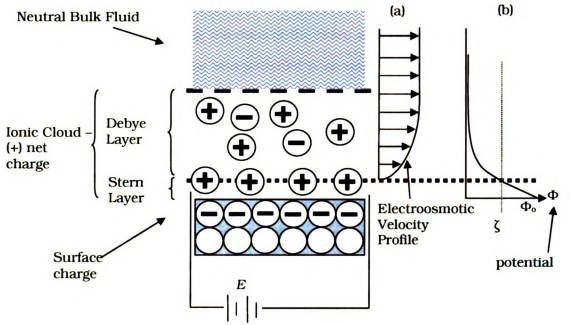

Figure 4-3. Schematic of a typical ion distribution in the vicinity of a charged surface and the resultant electroosmotic velocity profile and surface potential (Probstein, 1994)

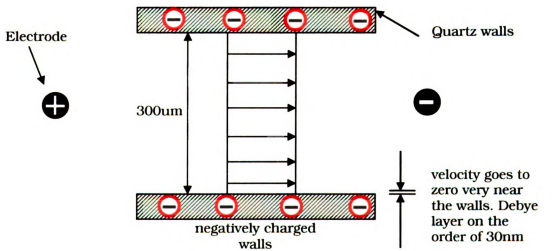

Figure 4-4. Schematic of velocity profile within microchannel for electroosmosis

Diagram (b) in Figure 4-3 illustrates the change in potential with distance from the surface. The surface potential, Φ_0, is dictated by the amount of deprotonated silanol

groups that are present. The potential drops at the Stern layer due to the presence of ions of opposite charge. At the interface of the Stern and Debye layer, the potential is called the zeta potential, ζ The zeta potential is an important aspect of electroosmosis because it is this potential that the rest of the ions within the fluid are affected by.

4.2.1 Factors Affecting Zeta Potential

The uniformity of the formation of deprotonated silanol groups and thus the consistency of surface charge for different microchannels, however, depends on the pH value of the aqueous solution it is exposed to. At a lower pH, less silanol groups are deprotonated which causes a reduction in surface charge. Figure 4-5 illustrates the zeta potential for various surfaces at different pH values. The potential at the shear surface is defined as the net addition of the surface charge and the charge present in the Stern layer. At a particular electrolyte concentration, reducing the pH causes a reduction in zeta potential. The reduction in zeta potential is due to the reduced presence of deprotonated silanol groups. The zeta potential can even be made to change sign at very low pH (sapphire, for example). When an electric field is applied within the microchannel over time, positive ions tend to accumulate at the anode and negative ions at the cathode. Positive ions contribute to the basicity whereas negative ions to the acidity of the solution. This essentially creates a pH gradient within the electroosmotic flow setup and may ultimately affect the uniformity of the zeta potential. One way to limit the change of pH is by using a buffer solution which is discussed further in § 3.3 when results for electroosmotic flows are presented.

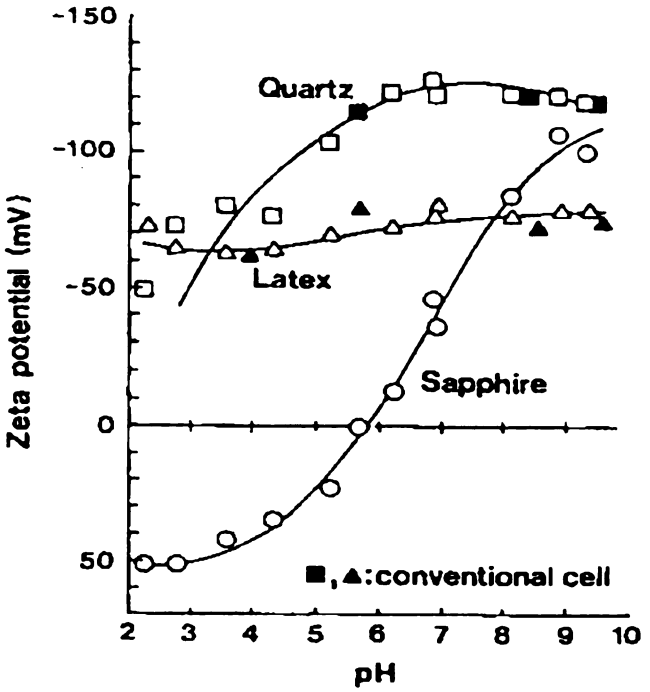

Figure 4-5. Plot of zeta potential for various surfaces at different pH values. (Ohshima, et. al., 1998)

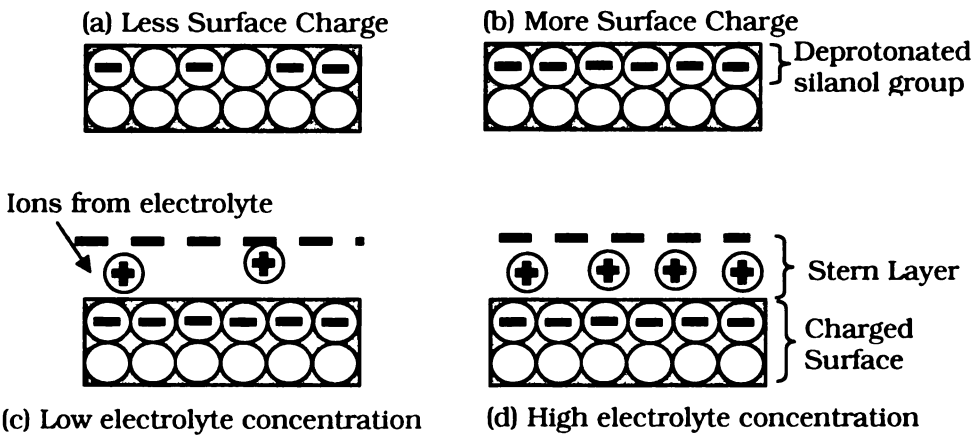

Figure 4-6. Schematic of a charged surface illustrating factors that affect zeta potential

Figure 4-6 further explores other factors that affect the zeta potential of a surface. For a surface that has less deprotonated silanol groups as in Figure 4-6(a), the zeta potential will be less compared to Figure 4-6(b) which has a higher surface charge.

Figure 4-6(c) on the other hand illustrates a high surface charge but a low concentration of electrolytes. Since the zeta potential is the net addition of the surface charge and the charge in the Stern layer, Figure 4-6(c) would have a higher zeta potential compared to Figure 4-6(d).

4.2.2 pH Stability

During electroosmosis, when fluid is transported within the channel, electrolysis is occurring simultaneously. The electrolysis of water causes a pH gradient to form. The following reaction balance details electrolysis of water and the formation of ions which causes the pH gradient (Skoog et. al., 1997).

$$\begin{aligned} 2H_2O &\rightarrow O_2 + 4H^+ + 4e^- \\ 4H_2O + 4e^- &\rightarrow 2H_2 + 4OH^- \end{aligned} \qquad 4\text{-}13$$

As electrolysis of water progresses, oxygen and hydrogen gases are created at the anode and cathode respectively but the amount of hydrogen gas created is two times that of oxygen gas. Positive ions and negative ions are also created and this causes a pH imbalance. To counter this, a phosphate buffer solution is used to buffer the additional ions present at each electrode and maintain the pH level. The following reaction balance details the workings of the buffer. (Skoog et. al., 1997)

$$\begin{aligned} H_2PO_4^- + OH^- &\rightarrow HPO_4^{2-} + H_2O \\ HPO_4^{2-} + H_3O^+ &\rightarrow H_2PO_4^- + H_2O \end{aligned} \qquad 4\text{-}14$$

Phosphate ions ($H_2PO_4^-$) react with hydroxide ions to form a different phosphate ion (HPO_4^{2-}) and water when there is an excess of hydroxide ions. The converse occurs when there are excess hydronium ions. Hydroxide and hydronium ions cause a change

in pH and by balancing the amount present in the fluid through the use of a buffer, the pH stays essentially constant.

Figure 4-7 illustrates the measured change of pH with an increased volume of sodium hydroxide within the sodium phosphate buffer solution. The plot illustrates plateaus of nearly constant pH values and once the buffering capability of the buffer solution is exceeded, a sudden jump to the next plateau is observed. The electroosmotic experiments will be conducted at a pH of 7 where any addition of pH contributing ions should not affect the overall pH significantly.

During the course of an electroosmotic experiment, the amount of additional ions accumulated at each electrode is assumed to be small. The amount of sodium hydroxide added to the buffer to cause the pH to cross the plateaus of almost constant pH is considerably larger than what is expected from a short electroosmotic experiment. Thus an essentially constant pH value can be assumed.

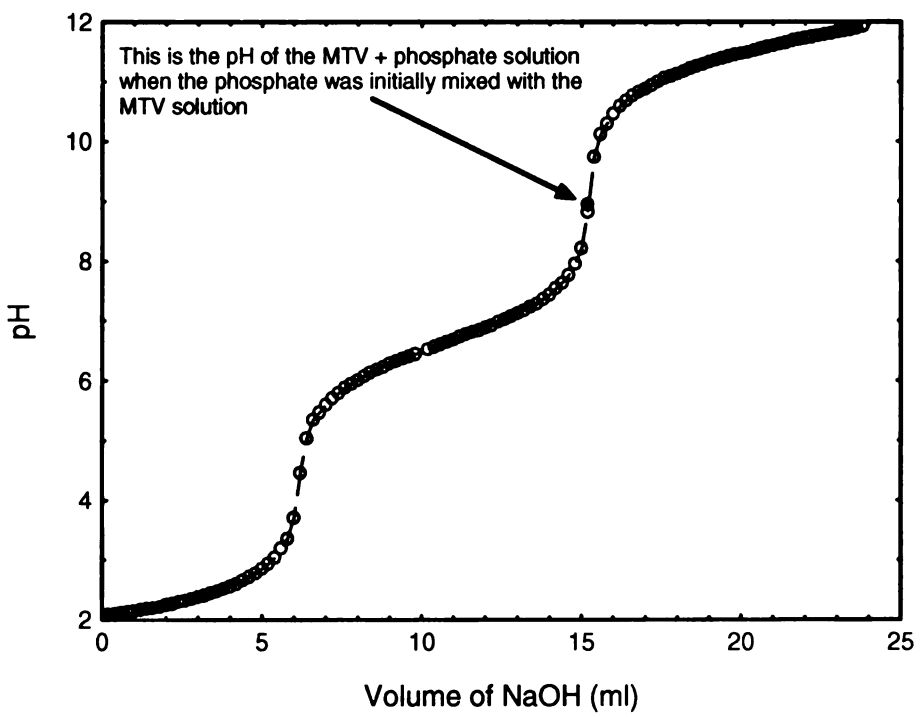

Figure 4-7. Change of pH of MTV Solution and Sodium Phosphate Buffer Solution with increasing volume of Sodium Hydroxide.

An essentially constant pH also translates to a constant zeta potential (refer to section 2.3). The zeta potential, as explained previously, is also affected by the concentration of the electrolyte. At a higher concentration, the amount of ions within the Stern plane increases and neutralizes the surface charge further. This creates a lower zeta potential.

4.2.3 Equation of Motion for EOF

The equation of motion for electroosmosis is based on the momentum equation with modifications to include the Lorentz forces caused by the presence of an electric field. The Lorentz relation is used to relate the forces on the ions and the bulk fluid flow in the system. This relation is shown in equation 4-15 (Probstein, 1994).

$$\vec{f} = \rho_E \vec{E} \qquad 4\text{-}15$$

where $\vec{f}$ is the force on an ion, ρ_E is the charge density (equation 4-3) and $\vec{E}$ is the electric field. It is worth noting that since equation 4-3 sums the valence number and concentration of each ion species, an electrolyte is necessarily electrically neutral unless an electric field is present. The momentum equation is shown in equation 4-16.

$$\rho \frac{Du_i}{Dt} = -\nabla p + \mu \nabla^2 \vec{u} + \rho \vec{g} \qquad 4\text{-}16$$

Assuming steady, fully developed unidirectional flow, neglecting any pressure gradients and gravitational effects while adding the contribution of the Lorentz forces, the momentum equation becomes

$$\mu \nabla^2 \vec{u} = -\rho_E \vec{E} \qquad 4\text{-}17$$

Substituting the Poisson equation (equation 4-2) for the charge density and integrating twice, the resultant electroosmotic velocity is

$$u_x = -\frac{\varepsilon_o \varepsilon_r \zeta E_x}{\mu} \qquad 4\text{-}18$$

where ζ is the zeta potential, μ is the viscosity of the electrolyte and E_x is the applied electric potential. This is the Helmholtz-Smoluchowski equation used to characterize

electroosmotic velocity. This equation, however is valid only when the Debye length is significantly smaller than the size of the channel. For a Debye length that is comparable to the channel size, the Huckel-Onsager relation should be used instead (Probstein, 1994). The present study only deals with the former case and the Helmholtz-Smoluchowski equation proves to be adequate. A comparison of the Debye length to the channel size is presented in a later section.

Traditionally, the Helmholtz-Smoluchowski equation was used to determine the velocity component given an electric potential. This, however, can prove to be inaccurate since a significant amount of heat can be generated at high electric potentials. The rise in temperature of the fluid from heating will cause the relative permittivity and viscosity to change and result in a non-linear increase in velocity. This gives rise to the importance of measuring temperature and velocity simultaneously with the MTV&T technique so that the changes in the fluid properties can be accounted for.

4.2.4 Time Response of Electroosmotic Flows

The inertia of fluid flows in response to an electric field is largely disregarded for equilibrium flows. However, a finite time is needed for the ions within the flow to response to the applied potential. For electroosmotic flows, the two characteristic time scales are polarization of the double layer and viscous diffusion. Double layer polarization is dependent on the ions present in the fluid while viscous diffusion is dependent on the size of the channel. The time scales involved in the polarization of the double layer, τ_{dl} is estimated to be on the order of

$$\tau_{dl} = O\left(\lambda_D^2 / D\right) \qquad 4\text{-}19$$

where λ_D is the Debye length, and D the diffusion coefficient of ions within the fluid (Minor et. al. (1997)). The viscous diffusion time scale, τ_{eo} on the other hand is on the order of

$$\tau_{eo} = O(D_h \rho / \mu) \qquad 4\text{-}20$$

where D_h is the hydraulic diameter or characteristic length, ρ is the density and μ is the viscosity of the fluid. The larger the characteristic length, the longer the time scale would be. In the present study, the time scales are all in the sub-microsecond scales and are not expected to cause issues with measurement of the uniform velocity profile. The time scales are only important if the start-up phenomena of electroosmotic flow is being investigated. It is presented here for completeness.

4.2.5 Surface Conduction Effects

The Helmholtz-Smoluchowski equation given in equation 4-18 is a simplification as only the bulk conductivity of the fluid is taken into account in its derivation. One other factor that affects electroosmotic velocity is surface conduction. Surface conductivity is an excess quantities and is a second order effect. This phenomenon occurs because of an excess of ions constituting the countercharge. To quantify this effect relative to the bulk conductivity, the applied potential, E, is related to the current, I as in equation 4-21 (Lyklema, 1995).

$$\frac{I}{E} = AK^L + SK^\sigma \qquad 4\text{-}21$$

where I represents current, E the electric potential, A the cross-sectional area of the channel, K^L the bulk conductivity S is the circumference of the channel and K^σ the surface conductivity. The bulk conductivity contribution, AK^L, is Ohm's law and is the leading term in the equation. Comparison of equations 4-18 and 4-21 and eliminating E reduces the equations to the following.

$$U = -\frac{\varepsilon_o \varepsilon_r \zeta}{\mu}\left(\frac{I}{AK^L + SK^\sigma}\right) \qquad 4\text{-}22$$

When $SK^\sigma << AK^L$, the equation reduces to the standard Helmholtz-Smoluchowski equation. Experimental values (Bikerman (1935)) have shown that surface

conductivities do not exceed 10^{-8} S (Siemens) while present experimental bulk conductivities are easily two orders of magnitude higher (152 x 10^{-6} S). A measure of the relative importance of surface conductivity in electroosmosis is given by the Dukhin number (*Du*).

$$Du = \frac{K^{\sigma}}{lK^{L}} \qquad 4\text{-}23$$

where l is the characteristic length (typically the height or radius of the channel). When the characteristic length is large, the Dukhin number becomes negligibly small as does the contribution from surface conduction to electroosmotic flow (Lyklema, 1995).

4.2.6 Factors Affecting Electroosmosis

The Helmholtz-Smoluchowski equation gives a relation for electroosmotic velocity that allows a simplified view of the factors that affect electroosmosis. The permittivity, ε, (dielectric constant) is the capability of the fluid to hold charge and is the product of the permittivity in vacuum, ε_o, and the relative permittivity, ε_r. The permittivity of free space or vacuum, ε_o, is a constant given by 8.854 x 10^{-12} $C^2N^{-1}m^{-2}$, where C is Coulomb and N is Newtons, while the relative permittivity of the fluid, ε_r, is taken to be that of water. The relative permittivity of the fluid is assumed to be the same as water as the concentration of the buffer and the added phosphorescent chemicals are low.

Figure 4-8 illustrates the temperature dependence of the relative permittivity of water. Its temperature dependence needs to be taken into account since the temperature of the fluid changes with time during the course of electroosmosis due to Joule heating. As the temperature increases, the permittivity decreases. This is due to the increased mean free path between water molecules which causes a reduced ability

to conduct electricity. For example, as water evaporates and transitions to the gas phase, the permittivity drastically drops to unity.

The viscosity of the electrolyte is also changing with temperature (Figure 4-8). Thus it is imperative that both the temperature dependence of viscosity and the relative permittivity is taken into account when using the Helmholtz-Smoluchowski equation to predict electroosmotic velocity.

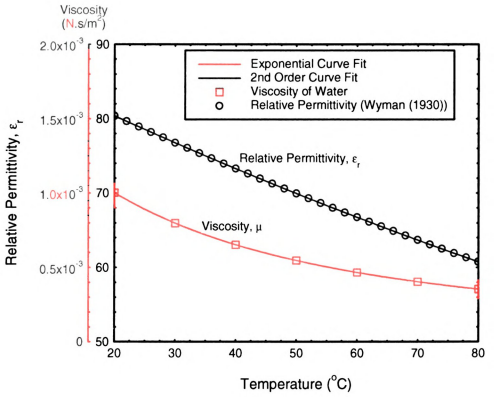

Figure 4-8. Plot of permittivity and viscosity of water vs. temperature (Wyman et.al, 1930, Handbook of Chemistry and Physics, 85th Ed.)

Joule heating is an integral part of electroosmosis as it is a by-product of fluid transport by an electric field. Factors that contribute to the significance of Joule heating include duration and magnitude of applied electric field, concentration and conductivity of electrolyte. As an electric field is applied for electroosmosis, a subsequent rise in temperature is observed. The power dissipated within the fluid due to the electric field is governed by the following equation.

$$P = IV \qquad 4\text{-}24$$

where P is the power in watts, I is the current and V, the applied voltage. A more detailed calculation of Joule heating is provided in Grushka et. al.(1989). The temperature rise within the channel is due to the inability of the setup to dissipate the amount of heat generated. For electroosmosis within a microchannel at low current and voltage, the heat is dissipated through conduction and convective currents outside the channel. At a higher applied voltage, the heat generated is not dissipated at a high enough rate and results in a temperature increase of the fluid within the microchannel. The increase in temperature is known to cause an increased amount of dispersion and results in band broadening in analyte separation analyses.

Another phenomenon that could occur during electroosmosis is electrophoresis. Electrophoresis is defined as movement of a charged surface or particle relative to a fluid (Probstein, 1994). When using the PIV technique, electrophoresis adds complexity to the technique as the electrophoretic velocity contribution of the particles need to be taken into account (i.e. measured particle velocity is due both to the fluid velocity and electrophoretic response of the particle). Figure 4-9 illustrates this.

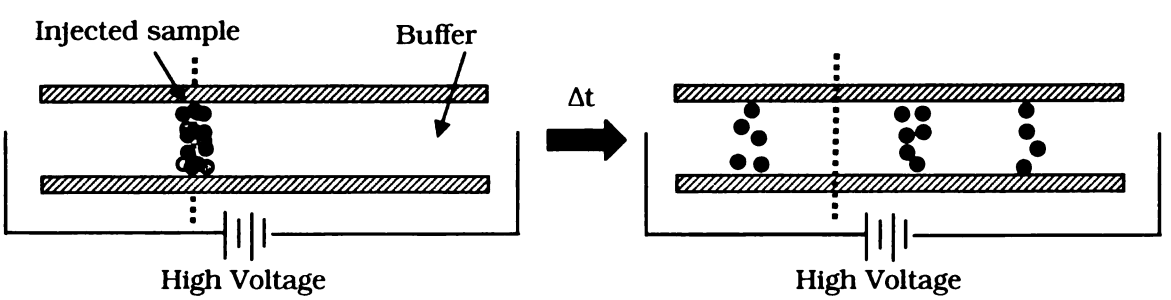

Figure 4-9. Electrophoresis

For example, imagine a slug of fluid with three different particles (each with a different surface charge and illustrated as different colors) is injected into a microchannel. Each particle has a different velocity as the charge characteristics are different. The yellow particles have an opposite charge compared to the red and blue particles and thus move in an opposite direction. The blue particles, on the other hand, have a higher surface charge and thus possess a higher electrophoretic velocity. To account for this, the measured velocity (through PIV) needs to be corrected for by the following equation.

$$U_{measured} = U_{electroosmosis} + U_{electrophoresis} \qquad 4\text{-}25$$

In the case of the MTV technique, a tracer molecule is added to the fluid and the electroosmotic mobility of the tracers also need to be taken into account. §4.3.3 detail the results on the electrophoretic mobility of the MTV triplex.

4.3 Results and Discussion for Electroosmotic Flows

4.3.1 Debye Length

From equation 4-7, the Debye length can be estimated to be 9.105nm for a buffer concentration of 1.12 milimolar (equation 4-26). In contrast, for pure water, the Debye length is several hundred nanometers thick.

$$\lambda_D = \sqrt{\frac{2\varepsilon RT}{F^2 z^2 c}} = \sqrt{\frac{2 * 78.3 \times 8.854 \times 10^{-12} C^2 N^{-1} m^{-2} * 8.314 JK^{-1} mol^{-1} * 300K}{\left(9.65 \times 10^4 C mol^{-1}\right)^2 (-2)^2 \left(1.12\ mol/m^3\right)}} \qquad 4\text{-}26$$

$$\lambda_D = 9.105nm$$

The Debye length of ~9nm is easily 4 orders of magnitude smaller than the characteristic length of 300μm for the microchannel used in this study. Thus the Helmholtz-Smoluchowski equation is applicable.

Other factors that may affect the Debye length are valency, temperature and permittivity. Recall that temperature plays a role in determining the Debye length (1/e decay of potential) as the thermal energy of the counter ions become higher as temperature increases. This increase in thermal motion increases the distance at which the 1/e decay is satisfied. However, this increase is countered by the lowering in permittivity as temperature rises. A 2% reduction in Debye length is estimated for a 20 degree change in temperature. This change in Debye length due to the temperature variance present in this study is considered negligible.

4.3.2 Conductivity of Solutions

For all electroosmotic flow measurements, an aqueous solution of sodium phosphate ($Na_2HPO_4.7H_2O$) with a concentration of 1.12 milimolar was used. At this concentration, the conductivity of the solution was measured to be 152 $\pm$ 5 μS. The conductivities were measured with an Oakton Con 110 conductivity meter. Plotted in Figure 4-10 is the change of conductivity with temperature for various solutions. For pure water (reverse osmosis, RO), pure water with the MTV Cyclohexanol mix and pure water with the MTV Neopenthanol mix, the measured conductivities are low ranging from 1-3 μS across a temperature change of 50 degrees. The rates of change of the three curves are also comparable. For the aqueous solution of sodium phosphate with the MTV Neopenthanol mix, the rate of change of conductivity is also comparable but the conductivity values are much higher. The values of conductivity are used to determine the rate of heat generation in the electroosmotic process. It was determined that the rate of change of conductivity with temperature is consistent with the increase in the measured current.

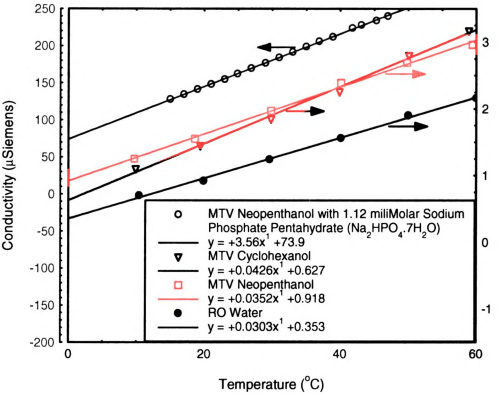

Figure 4-10. Change of conductivity of various solutions with temperature

4.3.3 Electrophoretic Mobility of MTV Triplex Solution

As mentioned in § 4.2.6, the MTV triplex may exhibit electrophoretic mobility. The term electrophoretic mobility applies to the movement of the tracer molecules relative to the electrolyte when under the influence of an electric field. This has the detrimental effect of causing the measured velocity to be a combination of the tracer and solvent velocity and not solely that of the solvent. To investigate this, the electrophoretic velocity of the MTV triplex was measured.

A capillary electrophoresis experiment was setup with a buffer concentration of 10 milimolar at a pH of 7. Figure 4-11 illustrates a typical capillary electrophoresis setup.

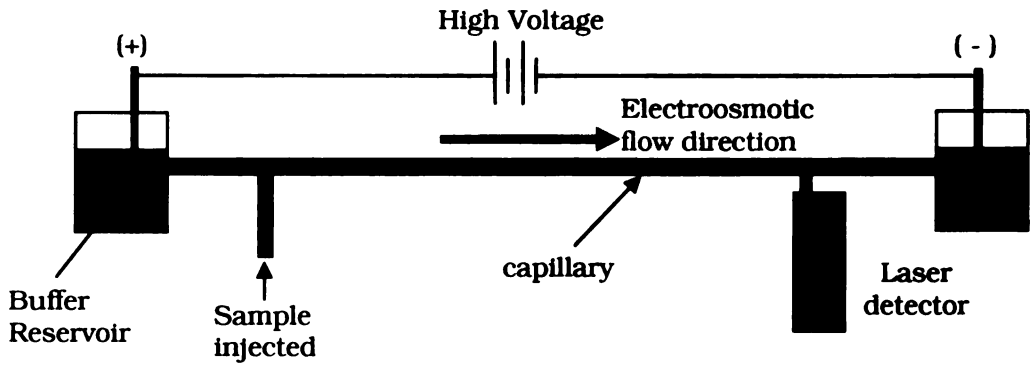

Figure 4-11. Typical Capillary Electrophoresis Experimental Setup

A sample of the MTV triplex is injected into the capillary initially and the elution time is tracked. The capillary used had a length of 34.1cm and the high voltage source was set at 15,000 V which is equivalent to 439.88 V/cm. For the given capillary length and applied voltage, the results are shown in Table 4-1.

Neopenthanol MTV - Detected at 212 nm - No Dilution			
	Retention Time (min)	Retention Time (s)	Apparent Mobility($cm^2/V/s$)
Run 1	2.096	125.76	4.700E-04
Run 2	2.014	120.84	4.891E-04
Run 3	2.116	126.96	4.656E-04
		Average	4.7E-04
		StDev	1E-05

Table 4-1. Elution time for MTV Triplex (Neopenthanol)

The apparent mobility of the MTV triplex is on average 4.7 x 10^{-4} $cm^2/(V.s)$. To determine the measurement accuracy of the technique, the elution time of mesityl oxide is measured. Mesityl oxide is a neutral marker that is regularly used as a reference neutral marker to determine electroosmotic mobility. The results are shown in Table 4-2.

Mesityl Oxide (Neutral Tracer Molecule) - Detected at 195 nm - 1 uL per 1 mL of Buffer			
	Retention Time (min)	Retention Time (s)	Apparent Mobility($cm^2/V/s$)
Run 1	1.951	117.06	5.049E-04
Run 2	1.915	114.9	5.144E-04
Run 3	1.949	116.94	5.054E-04
		Average	5.08E-04
		StDev	5E-06

Table 4-2. Elution time for Mesityl Oxide (neutral marker)

Note that the averaged electroosmotic mobility for mesityl oxide is larger than that for the MTV triplex which would indicate an apparent negative mobility. To investigate the validity of the results, the elution time for a standard MTV triplex with cyclohexanol was also measured. The electroosmotic mobility of this mixture should be of the same sign since both triplex have alcohol groups that should display similar pKa values. The results for the MTV triplex with cyclohexanol are shown in Table 4-3.

Cyclohexanol + MTV - Detected at 195 nm - Diluted 1:10 in Buffer			
	Retention Time (min)	Retention Time (s)	Apparent Mobility($cm^2/V/s$)
Run 1	1.864	111.84	5.28E-04
Run 2	1.877	112.62	5.25E-04
Run 3	1.861	111.66	5.29E-04
		Average	5.28E-04
		StDev	2E-06

Table 4-3. Elution time for MTV Triplex (cyclohexanol)

Contrary to what was expected, the elution time for the MTV triplex with cyclohexanol indicated a positive electroosmotic mobility. A last experiment was performed where all three solutions were mixed together to investigate if three separate peaks could be resolved. The capillary electrophoresis technique could not resolve three separate peaks

although the peak when all three chemicals were tested together appeared wider. This is shown in Figure 4-12.

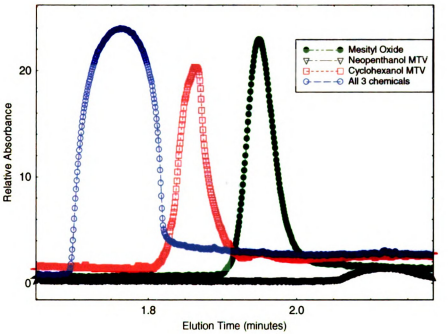

Figure 4-12. Detection peaks for the three chemicals separately tested and combined.

The fact that when all three chemicals were tested together that only a single peak was detected illustrates that the discrepancies from the individual testing are caused by errors in the measurement and the MTV triplex is essentially neutral with no electroosmotic mobility. The wider peak however allows the investigation of the measurement resolution. The resolution is defined as

$$Rs = \Delta t / (0.5 * (FWHM_1 + FWHM_2)) \qquad 4\text{-}27$$

where Δt is the time that separates two peaks and FWHM signifies the width of each peak (in time scale) at half maximum. It is commonly accepted that the resolution needs to be more than 1 in order for a peak to be resolved. Figure 4-13 illustrates a basic Gaussian curve displaced 0.45*FWHM to each side and superposed together.

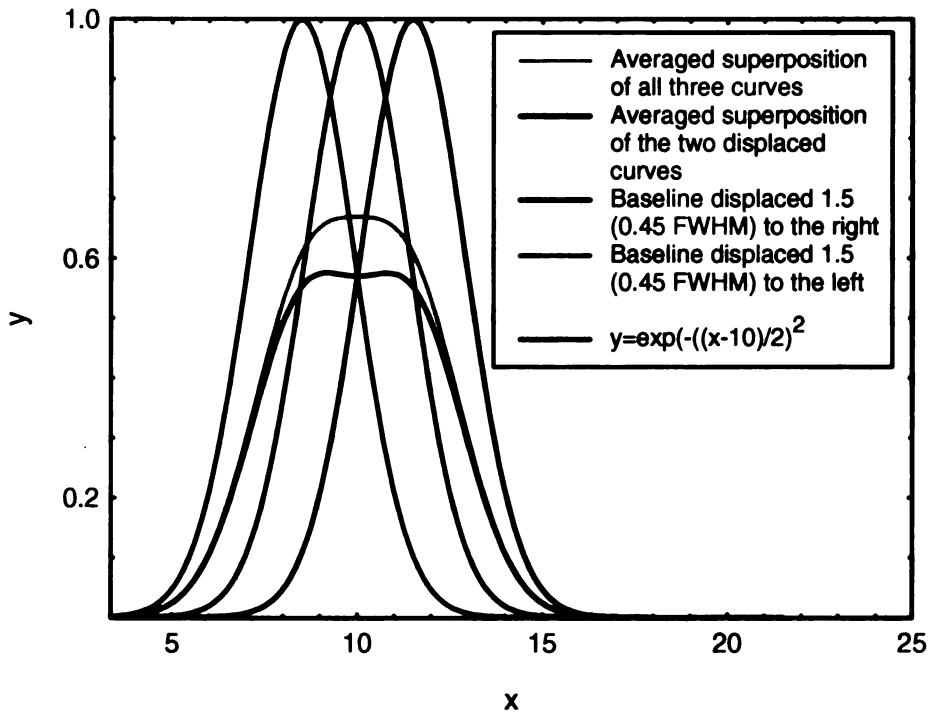

Figure 4-13. Plot of superposition of peaks

The superposed curve displays a noticeable dip in the center and is beginning to show separation between the two curves. When all three curves (basic and displaced curves) were superposed, a flatter peak is observed. The flatter peak has similar likeness to the peak observed in Figure 4-12 when all three chemicals were simultaneously measured. It can be concluded that although no peak separation is observed, an uncertainty due to the flatter peak of the combined measurement is present. This uncertainty is approximately 0.5* FWHM and in the case of the peak width of mesityl oxide in Figure 4-12, this corresponds to 1.38 seconds. Thus the electrophoretic mobility of the MTV triplex is $0 \pm 1.4135 * 10^{-5}$ cm²/(V.s) The uncertainties in determining the mobility is at least an order of magnitude better than the electrophoretic mobility of rhodamine B, fluorescein and other dyes. To put the uncertainty in determining the electrophoretic mobility in perspective, for a 200V/cm (typical for the experiments in this study) potential gradient, a velocity uncertainty of 28μm/s is present.

4.3.4 Experimental Results for Time Evolution of Electroosmotic Velocity with Joule Heating

Simultaneous velocity and temperature measurements were performed for different electric potential along the microchannel using the MTV&T technique. The velocity information obtained is useful in determining the evolution of electroosmotic velocity in time as Joule heating becomes more of an issue. The temperature information on the other hand, is used in analyzing the degree of Joule heating involved and decoupling the effects of temperature on the determination of electroosmotic velocity. The experiment was performed on three different surfaces; uncoated quartz, OTS-coated quartz and HEMA-coated quartz microchannels and the electric potential was varied from 560V-1963V (74.7V/cm – 234.9/cm) in increments of ~200V. Figure 4-14 illustrates the undelayed and delayed images for electroosmotic flow within uncoated quartz microchannels. Similar image pairs were also obtained for the other coated microchannels and are not shown here.

In Figure 4-14, the undelayed images are all arranged on the left side while the delayed images (5ms delay) are to the right. The images are averaged over 25 instantaneous images. The dashed line in each delayed image signifies the location of the undelayed tagged fluid before any displacement has occurred. As the applied potential increases, the separation between the tagged fluid and this dashed line increases denoting a higher electroosmotic velocity as potential increases.

Recall from § 4.3.1 that the Debye length is short (~9nm) relative to the characteristic height (300μm) of the microchannel. With reference to Figure 4-3, the velocity profile measured with the MTV technique will only reveal the velocity profile within the "neutral bulk flow" region which is uniform in nature. Inspection of the data set however, indicated a non-equilibrium starting condition for each experiment and the electroosmotic velocity profiles were contaminated by a pressure gradient.

74.7 V/cm
Undelayed Image

Delayed Image (5ms delay)

127.9 V/cm
Undelayed Image

Delayed Image (5ms delay)

181.6 V /cm
Delayed Image

Delayed Image (5ms delay)

234.9 V/cm
Undelayed Image

Delayed Image (5ms delay)

Figure 4-14. Image pairs at various potential gradients (74.7-234.9V/cm)

This is due to the heights of the two reservoirs in the experimental setup not being at equilibrium before the start of the experiment. This is illustrated in Figure 4-15. The pressure gradient was acting against the direction of flow for electroosmosis and had to be taken into consideration to accurately account for the velocity component. Note that this set of conditions were only apparent for the initial uncoated quartz microchannel dataset. More care was taken with subsequent results to avoid this pressure gradient contribution.

An example image pair of the presence of a pressure gradient is shown in Figure 4-15. The undelayed image,(a), in Figure 4-15 is an average of 25 images while the delayed image ((b), 5ms later) is an instantaneous realization.

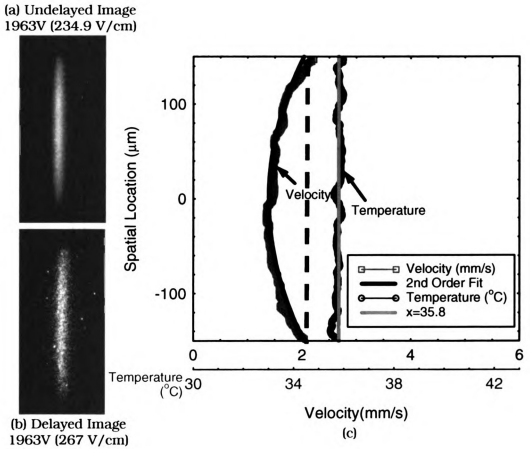

Figure 4-15. Typical electroosmotic flow and temperature profiles showing contamination of pressure gradient

Cross correlation of these images produced the red data points in (c). From Chapter 3, the velocity profile for pressure driven flows is necessarily a parabolic. Thus a 2nd order curve (green curve, symmetric) is fitted to the profile and the curve's intersection with the channel walls is taken to be the actual electroosmotic velocity (dashed line). For this case, an electroosmotic velocity of 2mm/s and an average temperature of 35.8°C is obtained. Note that the temperature profile is uniform along the height of the microchannel. This procedure was applied to the whole data set to correct for the added pressure gradient. The temperature results, as shown in (c) of Figure 4-15, are not affected because the correlation program tracks the correct region of fluid for calculation of temperature. The correlation program calculates the velocity (red data points) and simultaneously obtains the lifetime of the tagged fluid to give temperature information. In this case where pressure gradient contribution is present, post-processing of the data is needed to extract the electroosmotic velocity.

Figure 4-16 illustrates the electroosmotic velocity at different applied electric potentials and a non-linear increase in velocity is observed.

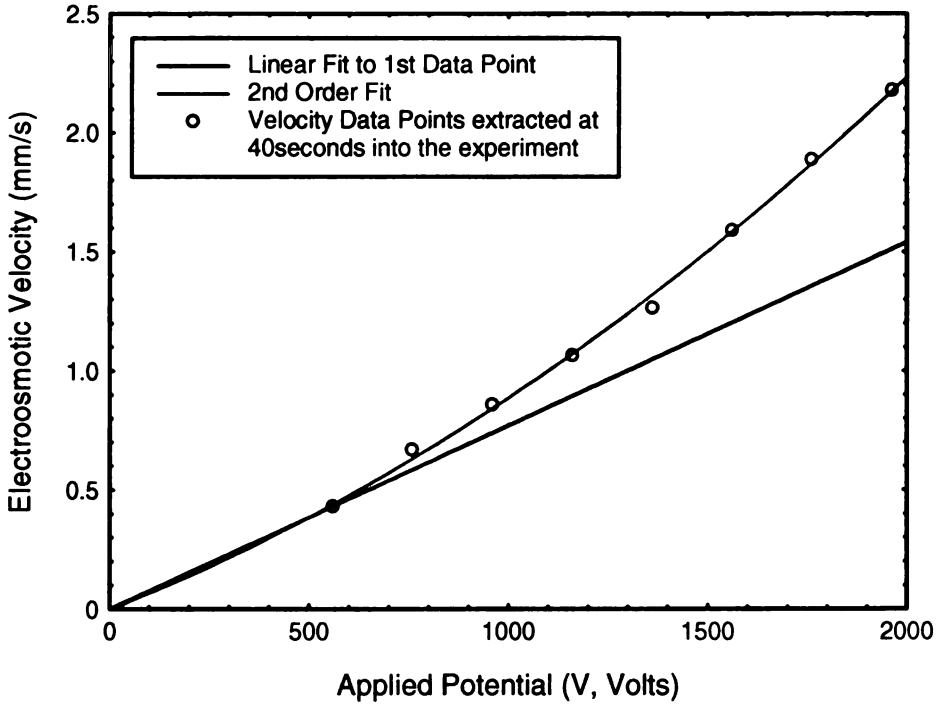

Figure 4-16. Non-linear increase in velocity at different electric potentials

These data points were taken 40 seconds after the electric potential was turned on. Recall from the Helmholtz-Smoluchowski equation (4-18) that the electroosmotic velocity is linearly dependent on the applied electric potential with all else being constant. This is shown by the black curve fitted to the first data point. A large discrepancy between the measured and calculated electroosmotic velocity is observed. When the electroosmotic velocity was plotted at the same temperature, the data points collapsed on a straight line as shown in Figure 4-17.

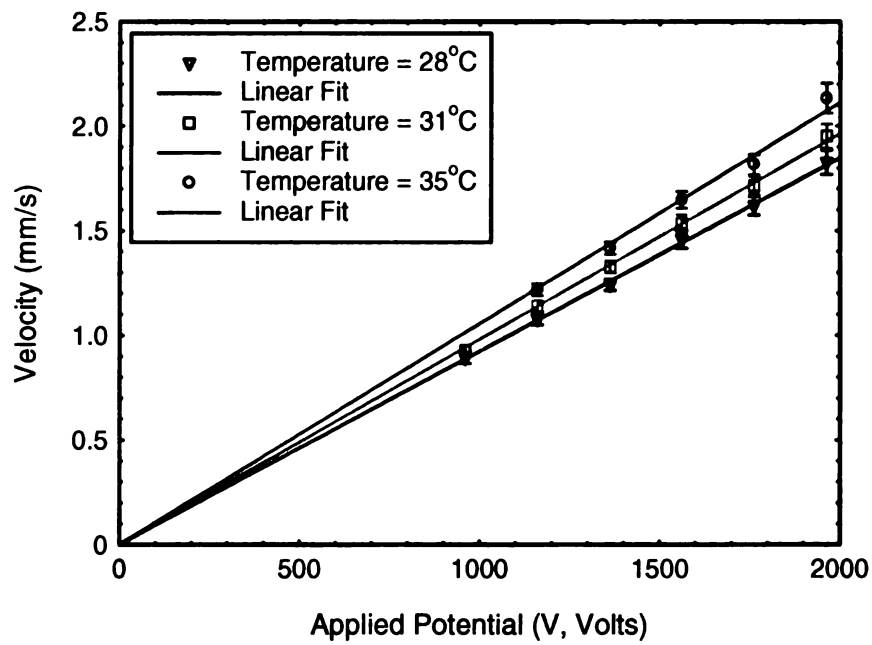

Figure 4-17. Electroosmotic velocity at different temperatures for uncoated quartz microchannels.

The non-linear increase in velocity is clearly caused by temperature affecting the other variables (viscosity, μ and relative permittivity, ε_r) in the equation. The different curves illustrate that the same linear dependence is observed at different fluid temperatures but with a slope that is temperature dependent. As the temperature of the fluid increases, the slope of the straight line increases due to the combined change of viscosity and permittivity with temperature. Similar experiments were also performed with microchannels coated with OTS and HEMA and the corresponding plot of

electroosmotic velocity against the applied electric potential are shown in Figure 4-18 and Figure 4-19.

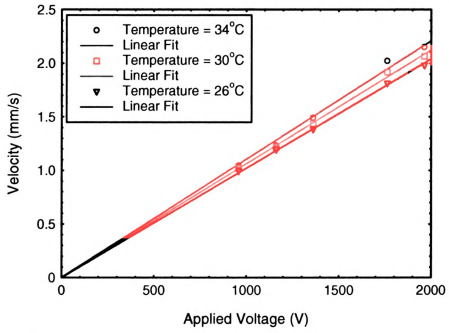

Figure 4-18. Electroosmotic velocity corrected at different temperatures for OTS coated microchannels

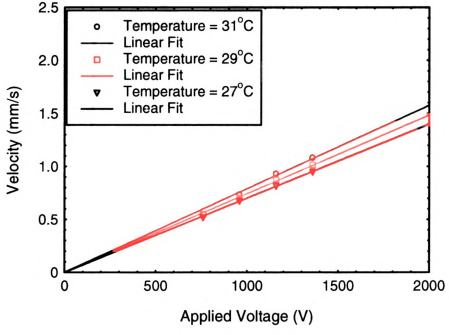

Figure 4-19. Electroosmotic velocity corrected at different temperatures for HEMA coated microchannels

The slopes for all three plots are different due to the differences in zeta potential. This will be discussed in further detail in the next section. Consequently, correct electroosmotic velocity measurements cannot be made without local temperature information or some temperature control mechanism to prevent Joule heating from being a problem. The MTV&T technique is advantageous in this respect to sort out the rise in temperature and its effect on increasing the electroosmotic velocity.

As the electroosmotic flow continues, the temperature of the fluid will rise and causes a rise in velocity due to a change in viscosity and permittivity of the fluid. The initial data set with no correction and the subsequent corrected data are shown in Figure 4-20. Every velocity profile at different times with no pressure correction as shown in Figure 4-15 (red data points) is averaged and is represented by a single data point (in pink) in Figure 4-20.

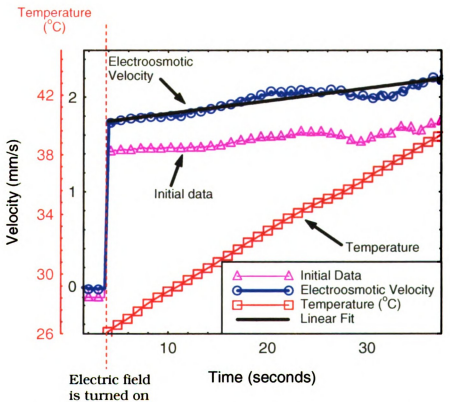

Figure 4-20. Initial data and corrected data for electroosmotic velocity.

Before the electric potential was turned on, the "initial data" set showed a negative averaged velocity indicating that a pressure gradient is present. As the data points are corrected, it is illustrated that the initial velocity correctly assumes a zero value. The sudden increase in velocity thereafter is due to the imposed electric potential. The velocity is seen to continually rise as Joule heating becomes prevalent.

All the electroosmotic velocity plots at different electric potentials were corrected for the added pressure gradient and plotted in Figure 4-21. Recall from Figure 4-8 that the dependence of viscosity and permittivity with temperature is non-linear. However, over the temperature range investigated in this study, a linear dependence can be assumed with minimal errors. Thus the velocity plots in Figure 4-21 were all fitted to a linear curve. Note that at lower applied potentials, the velocity is constant and does not vary with time. The heat generated at this applied voltage is dissipated and does not contribute to an increase in temperature of the fluid. As the applied electric potential increases, the velocity magnitude increases although the plot is seen to appear noisier. This increase in fluctuations in the velocity profile is mainly caused by the decrease in signal to noise of the experiments as temperature increases. Recall from Figure 2-24 that the lifetime decreases as the temperature rises.

The plot of temperature with time is shown in Figure 4-22. At an applied potential gradient of 74.67V/cm and 101.2V/cm, the increase of temperature with time is minimal resulting in a non-varying velocity plot in Figure 4-21. As the electric potential increases, the heating rate increases as well contributing to a higher temperature rise. The data set for different applied electric potentials is shown in Table 4-4. The first set of data illustrated in the table is the initial data where u_o is the electroosmotic velocity right after the application of the electric potential and u_f is the final velocity measured before the potential was turned off. These values for u_o and u_f were obtained from the linear fit to the curves in Figure 4-21. The corresponding temperature were obtained from Figure 4-22 and listed as T_o and T_f in the table.

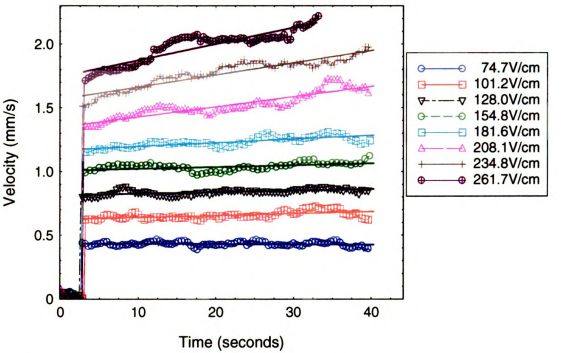

Figure 4-21. Plot of velocity increase with time for uncoated microchannels

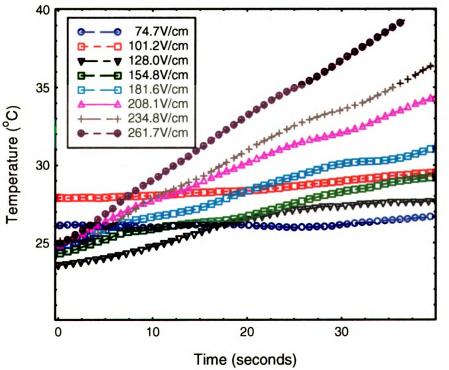

Figure 4-22. Plot of temperature increase with time for uncoated microchannels

Given the temperature rise during a particular experiment (for a given electric potential), the theoretical change in velocity was computed from the combined change of viscosity, μ, and relative permittivity, ε_r with temperature (refer to Figure 4-8 for dependence of viscosity and relative permittivity on temperature). The ratio, u_o/u_f, is a measure of the increase of electroosmotic velocity due to heating. Note that without any change in temperature, this ratio would be unity.

The initial data set included an opposing pressure contribution and thus yielded a lower ratio of u_o/u_f. When compared against the theoretical change in velocity, a higher discrepancy was observed. When a symmetric parabolic profile was fitted to account for the pressure gradient contribution, the experimental data matched well with theory and were within $\pm$ 3.5%. If velocity and temperature were not simultaneously measured, the determination of the electroosmotic velocity based only on the Helmholtz-Smoluchowski equation (4-18) at room temperature would be 24% lower. This is a significant underestimation of the velocity component.

	Velocity Data (pixels)						Temperature (°C)			% Disagreement with EOF Theory after Temperature Correction	
	Initial Data			Trend Subtracted - (Symmetric Parabolic)						Initial Data	Trend Subtracted - (Symmetric Parabolic)
Electric Potential Gradient (V/cm)	u_o	u_f	u_o/u_f	u_o	u_f	u_o/u_f	T_o (°C)	T_f (°C)	Theoretical Velocity Ratio, R_{th}	$(R_{exp}-R_{th})/R_{th}$ * 100	$(R_{exp}-R_{th})/R_{th}$ * 100
261.7	7.1	8.4	1.18	8.9	10.8	1.22	25.4	39.56	1.243	-4.718	-1.934
234.8	6.7	7.7	1.15	7.9	10.5	1.32	25.15	41.22	1.278	-9.688	2.983
208.1	6.0	7.1	1.17	7.1	8.5	1.18	25.38	38.6	1.227	-4.620	-3.433
181.6	5.0	5.7	1.15	5.8	7.4	1.28	25.04	40.51	1.265	-9.480	0.972
154.8	4.2	4.7	1.12	5.0	6.0	1.22	24.52	35.66	1.2	-6.829	1.274
128	3.6	3.8	1.04	4.1	4.6	1.10	24.98	33.21	1.142	-8.590	-3.551
101.2	3.3	3.2	0.98	3.2	3.7	1.15	26.12	32.97	1.128	-13.123	1.552
74.7	1.7	1.5	0.87	2.2	2.3	1.07	25.47	28.66	1.0537	-17.548	1.434

Table 4-4. Electroosmotic velocity corrected for temperature effects at different applied electric potential

4.3.5 Temperature Variation along Height (Z-axis) of Microchannel

Researchers (Ross et. al., 2001) have measured a large temperature gradient across the width (z-axis) of the microchannel. Ross et. al. measured a temperature gradient of 3°C in quartz capillaries and as large as 10°C in a prismatic acrylic microchannel using a fluorescent thermography method. These microchannels were approximately 50μm in size. Although these two microchannels were similar in size and were subjected to the same level of heating, a surprisingly large temperature gradient is present in the prismatic microchannel. Beam steering effects due to the high amount of curvature could be the cause of these discrepancies (The author did not detail the inaccuracies caused by the presence of curvature). The MTT technique was utilized in this study to measure the local temperature within a 300μm microchannel and no significant temperature gradient was observed along the height of the microchannel (z-axis, refer to Figure 3-2). The plot of temperature along the height of the microchannel with time is shown in Figure 4-23.

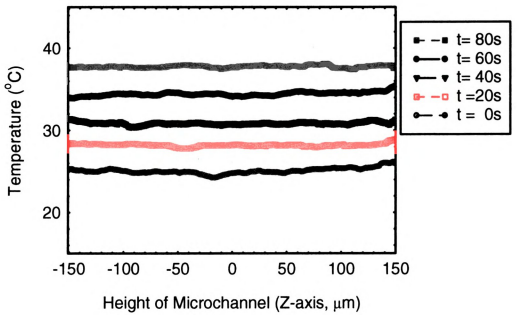

Figure 4-23. Time evolution of temperature profiles within the microchannel at 181.6V/cm

Note that the tagging laser and the viewing camera are perpendicular to each other and no beam steering effects are present due to the use of a rectangular channel. The temperature profile in the figure has an average RMS of 0.21°C. The error analysis is provided in Appendix K.

4.3.6 Computational Solution of Electroosmotic Flow in the Microchannel

The experimental setup for electroosmotic flow was illustrated in Figure 2-13. Optical access issues constraint the velocity and temperature measurements with the MTV&T technique to the central part of the microchannel (x-axis, $\pm$ 15mm). This constraint is caused by obstruction from the reservoirs and the physical size of the objective lens.

It is hypothesized that at the inlet of the microchannel, the temperature would be lower due to the intake of fluid from the reservoir with an ambient temperature. From § 4.3.4, the experimental results showed that the electroosmotic velocity is dependent on temperature. If the fluid at the inlet of the microchannel has a lower temperature, the resultant electroosmotic velocity at the inlet is necessarily lower. To compensate for the higher electroosmotic velocity in the center of the microchannel where the temperature should be higher (continuity), a pressure gradient should develop. To check this hypothesis, the heat diffusion characteristics of electroosmotic flow within a microchannel were computed numerically with FLUENT. The thermal development length and the temperature profile along the streamwise direction (x-axis) are of interest to better understand the flow characteristics of electroosmotic flow. Also, as mentioned in the previous section, some researchers have reported a high temperature gradient along the height of the microchannel (z-axis). The numerical solution would help in understanding if a temperature gradient exists.

The geometry of the microchannel is replicated in a grid generation package (GAMBIT) and solved numerically in a CFD software (FLUENT) with the boundary conditions of our experiments. The schematic of the microchannel reproduced in GAMBIT is shown in Figure 4-24. The middle of the channel is outlined in red and denotes the fluid within the microchannel. The volumes above and below the fluid depict the upper and lower walls of the microchannel while the inlet is defined at the positive end of the x-axis.

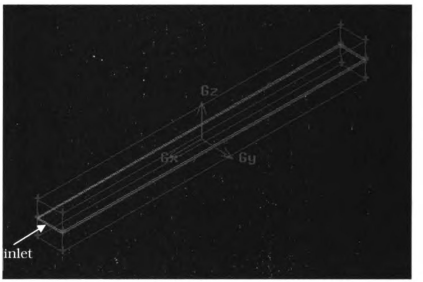

Figure 4-24. Schematic of microchannel in GAMBIT

The side walls (1mm) are not depicted in the schematic as GAMBIT allows for boundary conditions of wall thickness and thus the physical geometry does not have to be reproduced. This wall thickness boundary condition is applied on all side walls. Figure 4-25 illustrates the wall thickness boundary condition superposed on the end-view of the microchannel. In GAMBIT, the type of boundary conditions is defined for the inlet, outlet and walls of the microchannel. A "VELOCITY_INLET" boundary condition was specified at the inlet while an "OUTFLOW" condition was specified for the outlet.

Outflow boundary conditions are used when the flow velocity and pressure are not known prior to solution of the problem. (FLUENT Manual)

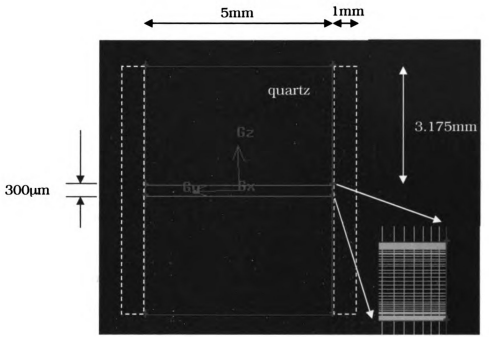

Figure 4-25. Schematic of end-view of microchannel with superposed wall thickness

The mesh needed to compute the solution was created in GAMBIT. For the fluid, a fine grid was employed along the 300μm height (z-axis) of the microchannel to resolve the temperature gradients that may exist. An "successive ratio" condition was set for the grid size where a higher density of grids are present near the interface of the fluid and the quartz walls. A minimum grid interval of 7.5μm was used. For the walls of the microchannel, a coarse grid interval was used to minimize computation time while maintaining grid independence of the solution.

The mesh from GAMBIT was imported into FLUENT to compute the solution. Within FLUENT, the properties of the fluid and quartz, and the specific boundary conditions were assigned to each face or volume in the geometry. The properties of

water were used for the fluid and is provided from the built-in database within FLUENT. The properties of quartz are detailed in Table 4-5.

Properties	Values
Density, ρ	2201kg/m^3
Specific Heat, C_p	770J/(kg.K)
Thermal conductivity, k	1.3W/(m.K)

Table 4-5. Properties of Quartz

The boundary conditions imposed on the geometry are illustrated in Figure 4-26. The heat transfer coefficient, h_{avg}, used here is a typical value used for free convection in external flows (Incropera, 1996). This boundary condition was applied to all external surfaces except the inlet and outlet faces of the microchannel which are exposed to the fluid in the reservoir. The walls at these locations were subjected to a constant temperature of 300K.

One of the difficulties encountered while specifying the boundary conditions was that FLUENT did not have provisions for computations of electroosmotic flows.

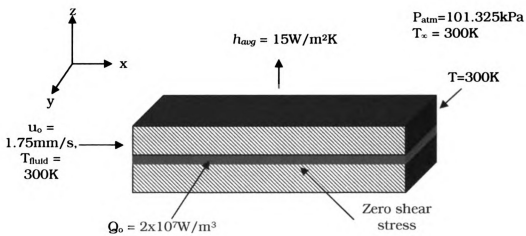

Figure 4-26. Boundary conditions applied to the geometry

This resulted in an ad-hoc modification of the inlet velocity, u_o, and heating rate, Q, based on the experimental results to simulate the effects of electroosmotic flows.

The initial velocity, u_o, was set at 1.75mm/s, similar to the initial electroosmotic velocity measured within the microchannel at an applied electric potential of 261.7V/cm (refer to Figure 4-21). The experimental data from this particular applied electric potential was used as it represents the highest heating rate measured by the experiments. Any temperature gradient that may develop within the microchannel should manifest itself under these conditions. The rate of increase of velocity measured through the experiments was also incorporated into the increase of the inlet velocity. The user-defined function (UDF) used to modify this property is detailed in Appendix P. To create a uniform velocity profile within the microchannel, a zero shear stress condition was set for all internal walls.

During electroosmosis, a constant voltage was applied along the length of the microchannel. From measurements of the current required to maintain this voltage, a linear increase in current was observed (Figure 4-27).

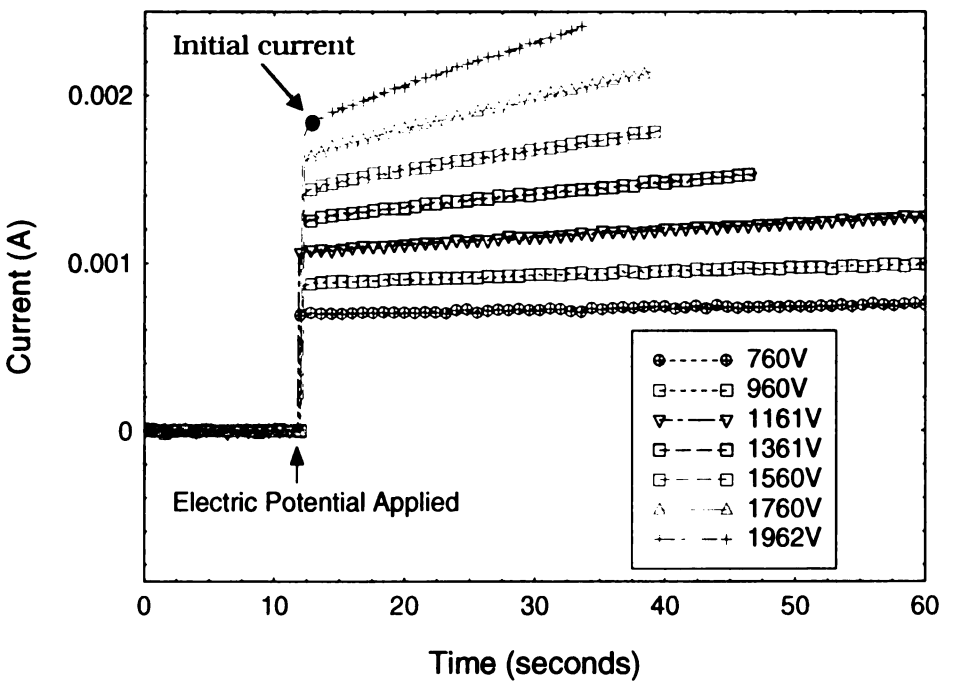

Figure 4-27. Plot of current rise with time at different applied voltage.

The rate of increase is consistent with the change of conductivity with temperature as shown in Figure 4-10. This indicates that the rise in current is solely caused by the change in conductivity with temperature. The slope of the current measurements at 261.7V/cm was used to obtain the rate of increase of the heating rate. The initial heating rate, Q_o, is computed in Equation 4-28 from the initial measured current (red circle in Figure 4-27. The UDF for specification of this property is provided in Appendix P.

$$P = IV = 1.7695x10^{-3}A * 1962V = 3.472\,uvatts$$
$$A = (5x10^{-3}\ x\ 300x10^{-6}\ x\ 63.5x10^{-3})m^3 = 9.5x10^{-8}m^3 \qquad 4\text{-}28$$
$$Q_o = \frac{3.472\,uvatts}{9.5x10^{-8}m^3} = 3.6451x10^7\ uvatts/m^3$$

This heating rate, however, caused a higher rise in temperature in the numerical simulations compared to the temperature measurements performed with MTT (Figure 4-22). An approximate factor of 3 lower heating rate was observed in the experiments. Notice that in Equation 4-28 that the fluid volume used represents only the internal volume of the microchannel. Since the electrodes were not placed directly at the inlet and outlet of the microchannel, the actual volume is difficult to measure. Thus a heating rate that resulted in a temperature increase consistent to the MTT measurements was selected for the computation instead.

For the aforementioned boundary conditions, Figure 4-28 illustrates the temperature contours of the fluid. The figure is scaled independently on each axis and is not shown in correct proportions. The width (Y-axis) is 5mm, the height (Z-axis) is 300μm and the length (X-axis) is 60mm. From the computation, at the inlet of the microchannel, the fluid has a temperature of 300K which steadily increases as it moves along the channel culminating in a region of high temperature in the center. The outlet of the microchannel sees a reduction in temperature as it is cooled by the other end of

the reservoir. A plot of the temperature profiles along the X-axis in the center of the channel is shown in Figure 4-29 at different times during electroosmosis.

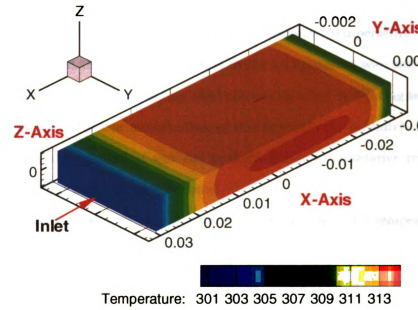

Figure 4-28. Temperature contour of the fluid at 30 seconds after application of the potential

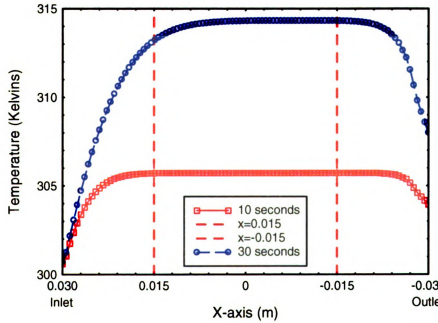

Figure 4-29. Temperature profile along X-axis at different times during electroosmosis.

Comparison of the temperature evolution for an electric potential gradient of 261.7V/cm in Figure 4-22 to the temperature profile in Figure 4-29 shows that the peak velocity at 30 seconds do not match. The peak velocity from the numerical simulation yielded a value of 41.3°C while the measured temperature was 36.7°C. It should be noted that the heating rate used in the computation was selected to give an approximate solution since the actual fluid volume affected by heating is not known. A trial and error and iterative modification of the heating rate to match the exact peak temperature could be done but was not performed as the qualitative results from the computation were deemed more important.

One key observation from Figure 4-29 is the presence of a temperature gradient along the length of the microchannel. Since electroosmosis is dependent on temperature, as detailed in § 4.3.4, each section of the microchannel would essentially have a different uniform velocity although the volume flow rate would still be constant. For capillary electrophoresis or other techniques utilizing the measurement of averaged flow rates to determine zeta potential, significant errors could result based purely on the assumption that the electroosmotic velocity is constant. To accurately measure the zeta potential in these setups, careful control of Joule heating is needed to minimize the differences in temperature gradient or an in-situ technique like the one applied in this study is required.

Another observation from the temperature profiles in Figure 4-29 is the thermal development length. As the temperature gradient along the length of the microchannel increases, the thermal development length increases accordingly. The vertical lines in this plot indicate the range of interrogation locations that were physically possible with the current experimental setup due to space constraints. If the MTT technique was used to measure the temperature profile within this range, no temperature gradient along the length of the microchannel would be measured for experimental times of < 30 seconds at this particular applied electric potential.

Temperature profiles along the z-axis were also obtained from the computation to investigate the temperature gradients along the 300μm height of the channel. Figure 4-30 illustrates the temperature profile along the z-axis at 30 seconds in time. Within the fluid (z = ±150μm), a parabolic temperature profile is observed with a maximum temperature gradient of only 0.32°C. For the measurement resolution of the MTT technique, a 0.32°C temperature gradient is at the threshold of its measurement limits and may not be detectable in the measurements. This is in contrast to the large measured gradients reported by other researchers (Ross et. al., 2001).

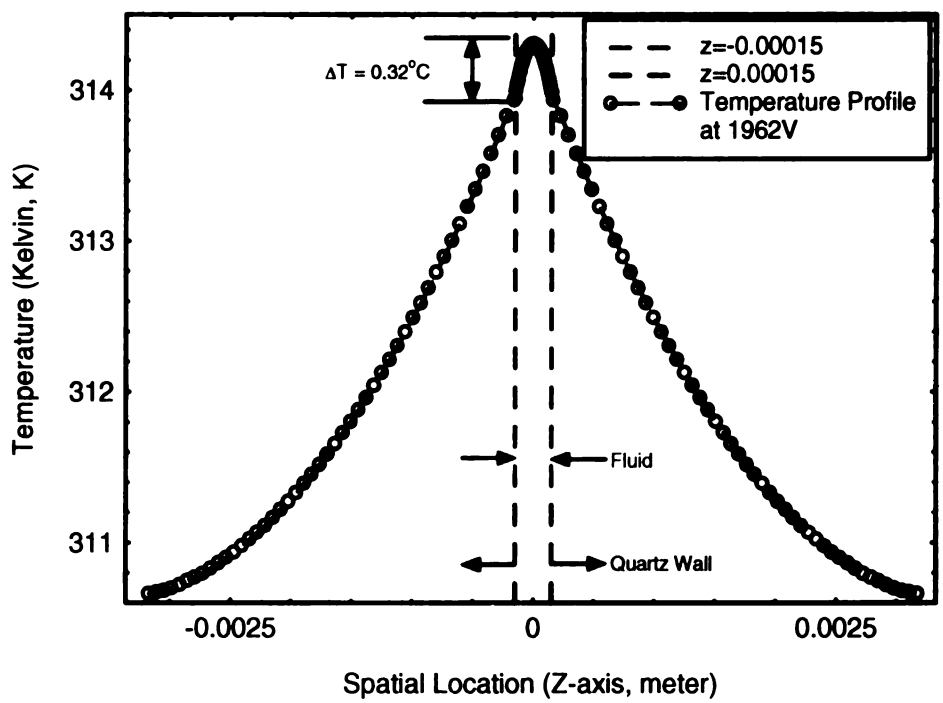

Figure 4-30. Temperature gradient along the Z-axis of the microchannel at X, Y = 0

4.3.7 Zeta Potential Measurements

The zeta potential of surfaces is usually measured with streaming potential, electroosmosis or electrophoresis experiments (Hunter (1981), Overbeek (1952), Erickson, et. al. (2000)). The streaming potential method measures the potential drop between two ends of the measuring region. This potential drop is caused by the transport of ions within the double layer due to the flow field created with a pressure gradient. The relationship between the imposed pressure gradient and the resultant potential measured is used to calculate the zeta potential. In electroosmosis, a potential gradient is applied along the length of the channel and the resultant flow rate is measured. The flow rate can be used to indirectly calculate zeta potential. Electrophoresis techniques are similar in approach.

The need to fully characterize the geometric size of the microchannel, the conductivity characteristics of the fluid and possible surface conduction effects and hydrodynamic considerations, however, complicates the use of these bulk measurement techniques. Surface conduction effects, although second order in nature, can significantly affect zeta potential measurements for capillary sizes on the order of the Debye length. All the measurement techniques described are useful but the measurements are averaged along the length of the measurement region and does not provide local zeta potential measurements. Although averaged measurements of zeta potential are important in obtaining general properties of materials, local measurements of zeta potential is critical for analysis of microchannels or labs-on-a-chip devices with non-uniform coatings. The different coatings can be utilized to induce better mixing characteristics within microchannels. (Stroock, et. al., 2000; Biddiss, et. al., 2004))

The molecular tagging velocimetry technique applied in this study is unique in that it provides a measure of the local electroosmotic velocity. When the contamination of the velocity profile (if any) is corrected for any pressure driven flow contribution and

temperature changes, the Helmholtz-Smoluchowski equation can be used to calculate the zeta potential. The zeta potentials for uncoated, OTS-coated and HEMA-coated quartz microchannels were measured and are shown in Figure 4-31. The zeta potential of HEMA was the lowest at -65.3mV while that of OTS is highest at -93.6mV and the value for an uncoated quartz microchannel is in between at -84.5mV. These values were averaged over multiple electric potentials.

Some researchers have documented a zeta potential in the -125 mV range (Ohshima et. al., 1998) for quartz although it should be kept in mind that the value of the zeta potential is dependent upon the concentration of the electrolyte and the non-uniformity of the surface charge may cause differing results. Thus it is usually difficult to match the exact zeta potential for different experiments, even for the same type of surface. In microchannels with non-uniform coatings (to induce additional mixing), the use of a predetermined zeta potential for a particular coating may wrongly predict the local zeta potential. This is an additional reason why in-situ measurements are advantageous. The measurements shown in Figure 4-31 were obtained with a 1.12mM buffer solution. Recall that the higher the concentration, the lower the zeta potential as more ions are available within the Stern layer to neutralize the surface charge. The plot illustrates velocity vs. volts at a given temperature (28°C).

Since the MTV&T measurement technique measures velocity and temperature simultaneously, it is now possible to prepare plots similar to Figure 4-31 at different temperatures to yield zeta potential information as a function of temperature. An example of this capability is shown in Figure 4-34. The red dashed line plotted in the figure illustrates the zeta potential of HEMA at 28°C while the other data points illustrate the measured zeta potential at different applied voltages along the length of the channel. A buffer maintains the pH levels within the microchannel and this slight variation in zeta potential may be due to the inadequacy of the buffer to maintain a stable pH as temperature rises. Nevertheless, this illustrated a measurement technique for obtaining zeta potential variance with temperature for different surfaces.

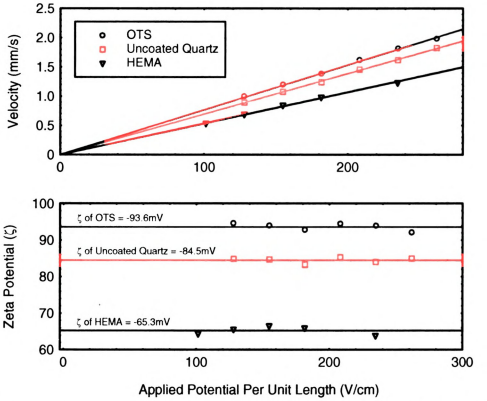

Figure 4-31. Zeta potential calculation from velocity vs. voltage plot at 28°C

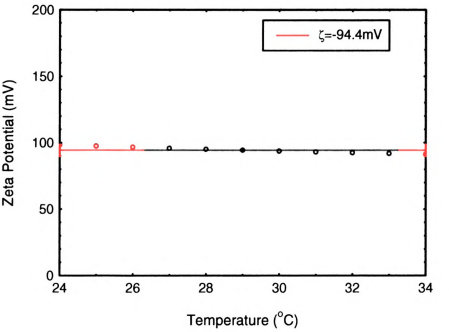

Figure 4-32. Plot of zeta potential of OTS vs. Temperature

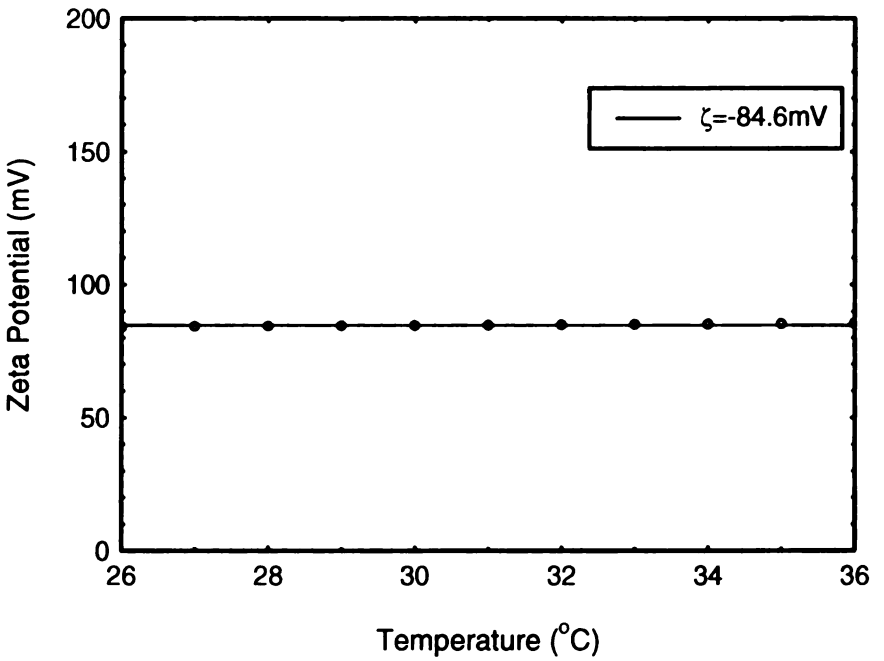

Figure 4-33. Plot of zeta potential of uncoated quartz vs. Temperature.

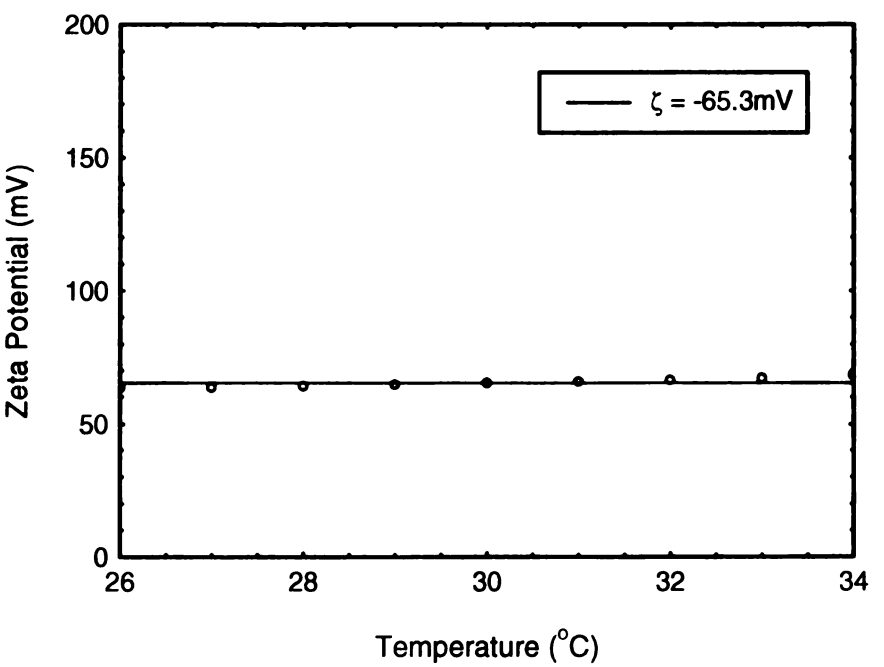

Figure 4-34. Plot of zeta potential of HEMA vs. Temperature

4.3.8 Contribution and Conclusions

This study has demonstrated that simultaneous measurements of electroosmotic velocity and temperature of the fluid is crucial in understanding the physics involved in such a flow. Without temperature compensation, the measured electroosmotic velocity can deviate significantly from the Helmholtz-Smoluchowski equation. When the in-situ temperature of the fluid is measured through experiments, the change of relative permittivity and viscosity with temperature can be taken into account to reveal the actual increase in electroosmotic velocity with increasing potential.

From the computational solution, Joule heating was found to cause temperature gradients along the length of the microchannel but the layout of the test section did not allow validation of the results with in-situ measurements of the temperature field at the inlet and outlet of the microchannel. The MTT technique measured temperature profiles along the z-axis and did not yield any temperature gradients but the numerical simulations showed that a temperature difference of 0.32°C exists. This small difference in temperature, however, is at the threshold of the MTT capability. Nevertheless, the results presented here showed a much lower temperature difference compared to the measurements performed by Ross et. al., 2001.

An indirect method for measuring zeta potential is from the measurement of electroosmotic velocity. The in-situ measurement of zeta potentials of three different surfaces was presented. For microchannels with a non-uniform surface coating (possibly to induce improved mixing), this technique allows the determination of the local zeta potential at multiple locations and not as an averaged value measured along the whole length of the microchannel. Since the simultaneous velocity and temperature within the microchannel was measured at different applied potentials and temperature, the temperature dependence of zeta potential can also be measured. The experiments in this study, however, were conducted with a buffer solution and this limited the change

of zeta potential with temperature. The buffer solution essentially maintains the pH levels within the test section.

4.3.9 Future Work

The temperature gradient along the length of the microchannel is mainly concentrated near the inlet and outlet. Due to the way the microchannel was mounted to the reservoirs and accessibility of the imaging system, only the central region of the microchannel was accessible to the imaging system. Thus the temperature variations along the length could not be measured here. To be able to measure these temperature gradients, the microchannel needs to be mounted differently. These measurements would provide further validation of the Fluent simulations and would provide a better understanding of electroosmotic flow in microchannels. Also, with the MTV&T technique, the velocity at these locations can be measured. Since the simulations showed that the inlet and outlet of the microchannel is at a lower temperature, the electroosmotic velocity is correspondingly lower compared to the center of the channel where a higher fluid temperature exists. From continuity, in order to maintain the flow rate, a pressure gradient is naturally present at the inlet and outlet. Unfortunately, the numerical simulations used a uniform inlet velocity. It would thus be of interest to study the velocity profile at different locations along the microchannel through experimental measurements and investigate the pressure gradient distribution.

The in-situ techniques of MTV and MTT were utilized to provide simultaneous velocity and temperature data. The velocity measurements indirectly provide zeta potential measurements. Without the use of a buffer to control the pH, the zeta potential can be systematically studied for variation with temperature and concentration.

Appendices

Appendix A: Lens Setup for Imaging

The lens setup used for all the imaging in this study is shown in the figure. Since a microscope was not utilized, due to space constraints and access limitations, an objective needs to be arranged in the following manner for use with the intensified cameras. The infinity-corrected objective (10X) was connected to the tube lens which directs the image to the image plane of the CCD. The working distance for the particular objective used in this study has a working distance of 33.5mm. The distance between the end of the tube lens and the CCD imaging plane is nominally 170mm. Within the camera body itself, various optical elements are present which causes the actual magnification to vary. The magnification calibration is provided in Appendix B.

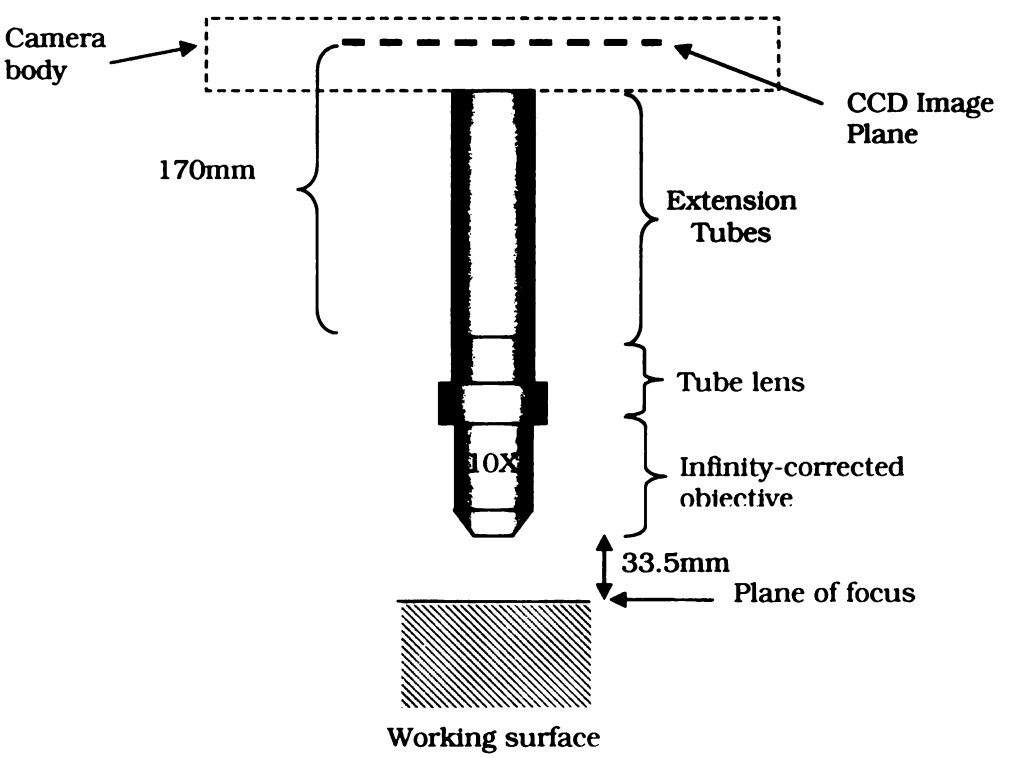

Figure A-1. Setup of Imaging Lens

Appendix B: Effective Magnification of Cameras

Optical elements in each of the intensified cameras used in this study caused a lower magnification when used with a 10X objective. This appendix details the calibration of the two camera.

Xybion ICCD Camera:

An image of a high-resolution target (Max Levy Autograph Inc.) was imaged with the camera using the 10X objective. Every line division in Figure B-1 is 50μm. A 1mm physical length translated to 512 pixels on the CCD.

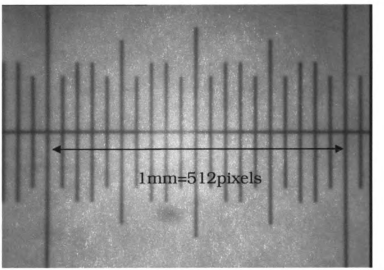

Figure B-1. High resolution target acquired with the Xybion ICCD (10X objective).

To convert this value to an effective magnification, the following calculation was done.

$$\begin{aligned} &Width\ of\ CCD\ chip(physical\ units) = scaling * width\ in\ pixels \\ &Width\ of\ CCD\ chip(physical\ units) = \frac{1mm}{512\ pixels} * 756 pixels = 1.47mm \end{aligned} \quad (1)$$

The camera manual indicates that the physical size of the CCD chip is 8.8mm (width) x 6.6mm (height). Dividing the actual width with that of equation (1) results in a magnification value of

$$Magnification = \frac{8.8mm}{1.47mm} = 5.96X \tag{2}$$

Dicam Pro Camera:

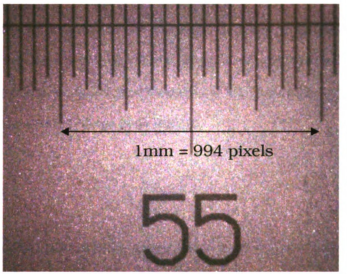

Figure B-2. High resolution target acquired with the Dicam Pro camera (10x objective)

Similarly, every line division in Figure B-2 is 50μm. A 1mm physical length translated to 994 pixels on the CCD.

$$\begin{aligned} &Width\ of\ CCD\ chip(physical\ units) = scaling * width\ in\ pixels \\ &Width\ of\ CCD\ chip(physical\ units) = \frac{1mm}{994\ pixels} * 1280\,pixels = 1.288mm \end{aligned} \tag{3}$$

For a CCD width of 8.52mm, the magnification is

$$Magnification = \frac{8.52mm}{1.288mm} = 6.6X \tag{4}$$

Appendix C: Intensifier Characteristics of Dicam Pro

An intensified camera has an added intensifier to the CCD and typically exhibits a non-linear gain response. This is especially a concern for the MTT technique where the intensity decay of the image is used to infer temperature information. Thus, characterization of the intensifier is important. The gain linearity and fast charge capability of the intensifier are two aspects of the intensifier that were studied. Gain linearity pertains to the response of the intensifier to a linear increase in incident light and non-linearity results when a non-linear response is measured. In the double-shot mode, images are taken in quick succession and the capability of the intensifier to charge rapidly for the second image is a concern.

Gain Linearity:

To measure gain linearity, the camera was setup to look at an intensity gradient as shown in Figure 1. An intensity gradient allows a wide dynamic range of intensity levels to be simultaneously imaged.

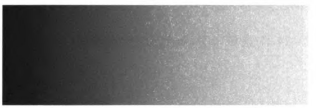

Figure C-1. Intensity Gradient

To fill the whole dynamic range of the camera, the exposure time was also increased with the assumption that the exposure time increases linearly with incident light. Figure 2 illustrates a plot of the linearity of gain. The abscissa is the theoretical intensity counts at a given exposure time while the ordinate is the measured intensity

from the camera. At low intensities, <1500 counts, the response of the camera is linearly varying with incident light and a noticeable decrease in response in seen at higher intensity counts. For the experiments performed in this study, all images were obtained at an intensity level of <1000 to avoid this non-linearity. However, it should be noted that as long as this non-linearity is characterized, the intensity levels in the images can always be corrected to measure the right temperature.

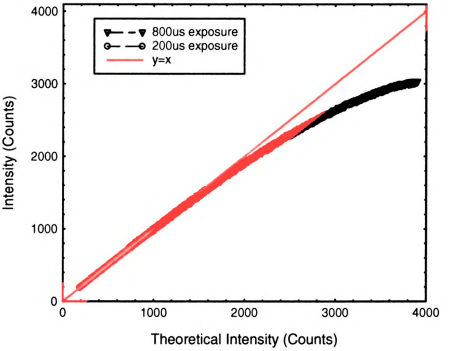

Figure C-2. Gain Linearity at Gain Setting of 99%.

Fast Charge Capability:

Measuring the fast charge capability of the intensifier requires the use of the same gradient shown in Figure 1. The exposure time is set so that the gradient covers a wide range of intensity levels. Figure 3 illustrates the intensity ratios of the first and second images. At 4ms delay and an initial intensity of 1000 counts in the first image, the ratio shows a 1.5% decrease in intensity in the second image while at 8ms, the

differences are negligible. This is factored into the measurement accuracy of the MTT technique.

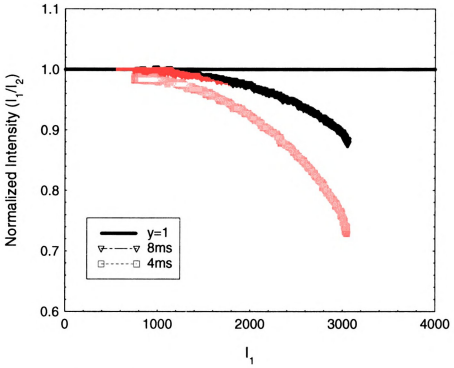

Figure C-3. Intensity ratios in double-shot mode

Appendix D: Laser and Camera Synchronization Setup

Xybion ICCD Camera:

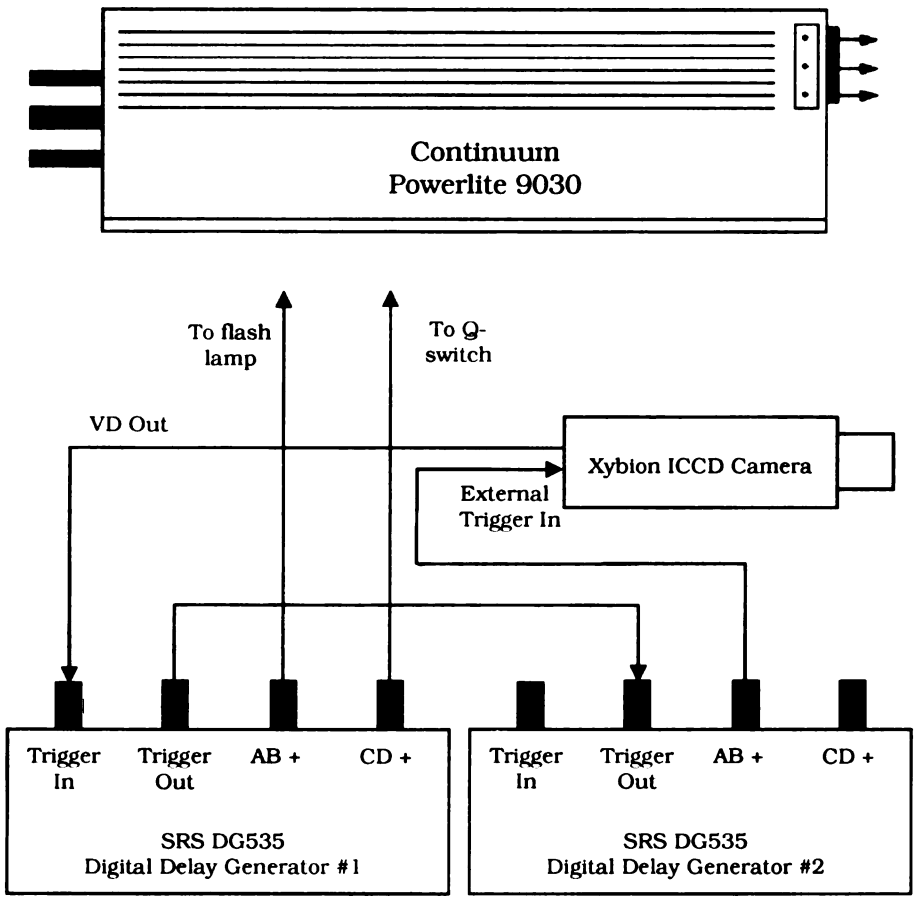

Delay Generator #1 Settings

Trigger: External
Trigger Threshold: +2V
Trigger Slope: (+)
Trigger Termination: High Z
All output loads: High Z
All output voltages: TTL/Normal
Delay A: T0+0.022seconds
Delay B: A + 10μs
Delay C: A + 385μs
Delay D: C + 10μs

Delay Generator #2 Settings

Trigger: External
Trigger Threshold: +2V
Trigger Slope: (+)
Trigger Termination: High Z
All output loads: High Z
All output voltages: TTL/Normal
Delay A: T0+0.022seconds
Delay B: A + 1ms

Dicam Pro Camera:

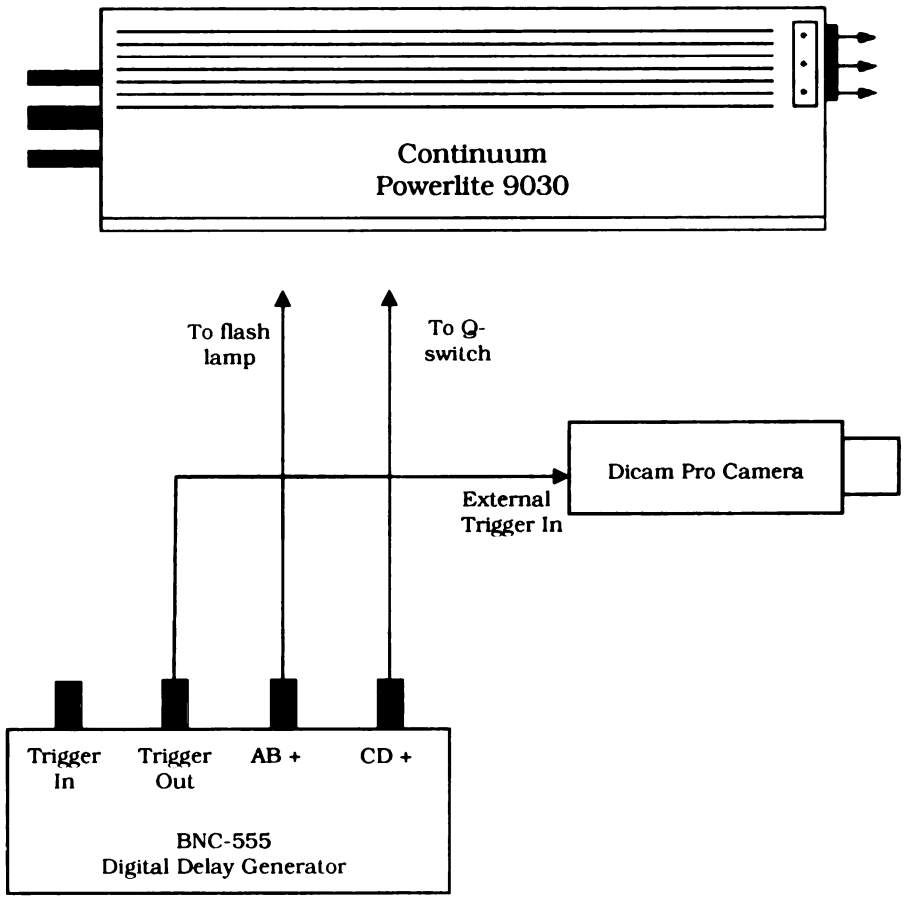

Delay Generator Settings

Trigger: Internal

All output voltages: TTL/Normal

Channel A: 10μs width, 0 delay

Channel B: 10μs width, 0.13384 secs delay

Appendix E: Pressure Drop within Microchannel

This section describes the pressure drop within a microchannel and the height difference in the reservoir for the electroosmotic velocity setup as illustrates in Figure 2.42 to cause a noticeable velocity within the microchannel. Figure 1 illustrates the electroosmotic flow setup while Equation 1 describes the factors that affect the pressure drop within the microchannel.

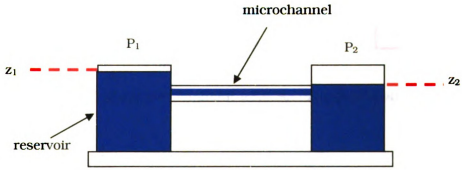

Figure 1. Electroosmotic flow setup

$$P_1 - P_2 = \gamma(z_2 - z_1) + f\frac{l}{d}\rho\frac{V^2}{2} + K_L\frac{1}{2}\rho V^2 \tag{1}$$

where P_1 and P_2 are the pressure above the reservoirs respectively (both are exposed to atmospheric pressure), γ is the product of density, ρ, and gravity, f is the friction factor, l is the length of the channel, d is the hydraulic diameter of the channel, V is the velocity within the channel and K_L is the loss coefficient. Since there are no external pressure induced forces, the term on the left goes to zero.

$$\begin{aligned}\gamma(z_1 - z_2) &= f\frac{l}{d}\rho\frac{V^2}{2} + K_L\frac{1}{2}\rho V^2 \\ \gamma(z_1 - z_2) &= \frac{96}{\mathrm{Re}}\frac{l}{d}\rho\frac{V^2}{2} + K_L\frac{1}{2}\rho V^2\end{aligned} \tag{2}$$

$$\gamma(z_1 - z_2) = \frac{96\mu}{\rho VD}\frac{l}{D}\rho\frac{V^2}{2} + K_L\frac{1}{2}\rho V^2$$
$$\gamma(z_1 - z_2) = \frac{96\mu l}{D^2}\frac{V}{2} + K_L\frac{1}{2}\rho V^2 \qquad (3)$$

For a rectangular channel with the dimensions 25.4mm X 0.3mm, the friction factor is defined as 96/Re (note that for round capillaries, the friction factor is 64/Re).

$$\gamma(z_1 - z_2) = \frac{96 * 1.12x10^{-3}N.s/m^2 * 0.05m * 0.01x10^{-3}m/s}{2*\left(0.5x10^{-3}m\right)^2} + \frac{0.4 * 999\frac{kg}{m^3} * \left(0.01x10^{-3}m/s\right)^2}{2} \qquad (4)$$

Nominally this value

$$\gamma(z_1 - z_2) = 0.10752\frac{N}{m^2} + 3.99x10^{-8}\frac{N}{m^2}$$

The first term on the right is the dominant term. As an approximation, we only keep the first term.

$$\gamma(z_1 - z_2) \approx 0.10752\frac{N}{m^2}$$
$$z_1 - z_2 \approx \frac{0.10752N/m^2}{999kg/m^3 * 9.81m/s^2} = 1.097x10^{-5}m = 0.01097mm\ @V = 0.01mm/s \qquad (5)$$

From the analysis above, a head difference of ~11μm is all that is needed for a velocity change of 0.01mm/s. From a constant head adjustment standpoint, a 11μm head adjustment is almost impossible to achieve as the fluctuation of the reservoir surface is easily more than 11μm. If the electroosmotic velocity that is induced is 2mm/s, the volume flow rate is estimated to be 2mm/s*5mm*0.3mm = 3mm^3/s. If we restrict the height change at the reservoir to be 0.01097mm, this translates to an area of 3mm^3/s/0.01097mm =273.5mm^2/s. For a 50mm diameter reservoir, the time for a 0.01097mm change in height at the reservoir is: π(25mm)^2/273.5mm^2/s=7.2seconds. By relaxing the criteria, a height change of 50μm is probably the best a constant head reservoir can achieve. This translates to a velocity of 0.05mm/s. The rate of change of area is then 3mm^3/s/0.05485=54.7mm^2/s. For a 50mm diameter reservoir, the time we

can run the experiment for is increased to $\pi(25mm)^2/54.7mm^2/s$ = 36 seconds. If the velocity is 1mm/s, we can run the test for 72 seconds.

Appendix F: Spatial Resolution of Measurements

With a 10X magnification objective, the Dicam Pro camera has a magnification of 6.6X while the Xybion ICCD exhibited a magnification of 5.96X. The line width coupled with the total displacement of the tagged molecules between the "undelayed" and "delayed" images determined the spatial resolution of the measurements. In the worst case scenario where the image pairs have a signal to noise ratio of 4 (instantaneous images), the correlation software in Labview results in an RMS (95% confidence) of 0.2 pixel.

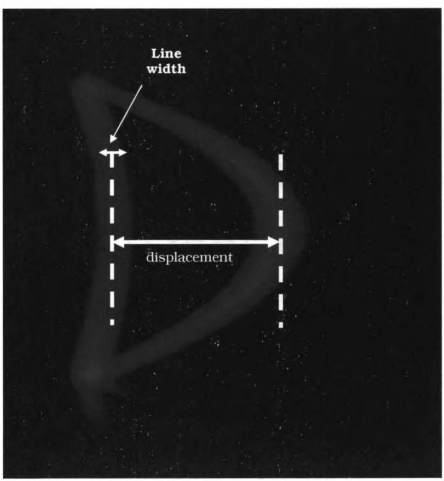

Figure E-1. Superposition of undelayed and delayed images

With reference to the largest (87 pixels) and smallest displacements (1 pixels) in this study, the corresponding spatial resolutions are calculated.

$$(\text{Spatial Resolution})_{\text{large}} = \textit{displacement}(\textit{pixels}) * \textit{scaling factor} = 87 * 1.95\mu m = 169.7\mu m \quad (1)$$

$$(\text{Spatial Resolution})_{\text{small}} = \textit{displacement}(\textit{pixels}) * \textit{scaling factor} = 1 * 1.95\mu m = 1.95\mu m \quad (1)$$

This result is applicable to both pressure driven and electroosmotic flows.

Appendix G: Velocity Profiles within commercial microchannels

Commercial quartz microchannels (Starna Cells) were initially used in the experiments. Figure 1(a) below illustrates a cross-sectional view of the microchannel. The height of the microchannel is 300μm. Notice that the internal geometry of the microchannel does not have square edges which would hinder viewing from the side. A slight curvature is also present on the exterior. The combination of these anomalies contributed to a spurious velocity profile at different tilt angles relative to the imaging system. Within a high aspect ratio rectangular microchannel, the velocity profile should resemble a parabola. This is exhibited in Figure 1(b).

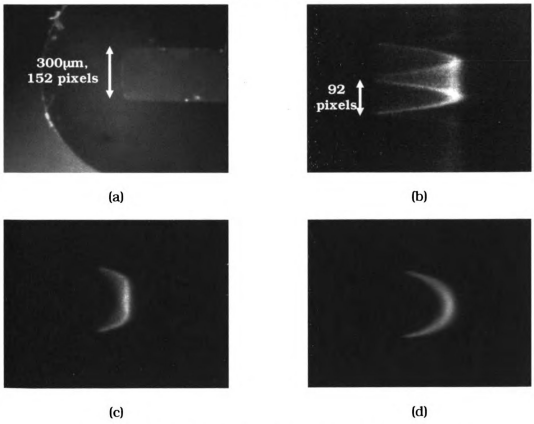

Figure 1. Velocity profile within commercial microchannels

However, the velocity profile is narrower (92 pixels) than the actual height of the channel (152 pixels). Another artifact is the double velocity profile seen in the image. At different angles, Figure 1(c) and (d) illustrates a completely different profile. When the microchannel was tilted to different angles, at no point did a single velocity profile match the dimensions of the microchannel while maintaining a parabolic semblance. This was not investigated further. This difficulty resulted in the making of our own rectangular channels from quartz flats.

Appendix H: Description of Single Line Velocity Profile Labview Program

This describes the working principle of the Labview program designed to give simultaneous velocity and temperature profiles. Figure 1 illustrates the graphical user interface (GUI) of the program. For temperature measurements, the calibration constants of the MTV chemical have to be provided along with the lifetime of the normalization point.

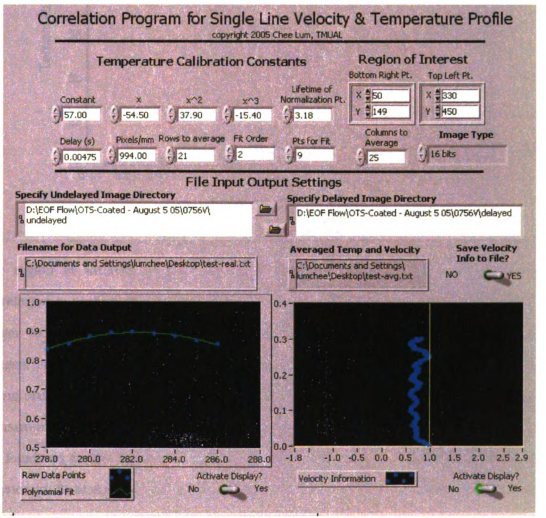

Figure 1. Graphical User Interface for Correlation Program.

The normalized calibration constants are shown in Figure 2. It was determined that the MTV chemicals prepared on different days may differ in lifetime values but the normalized lifetime always collapsed on a single curve. Thus a normalized calibration curve was used in the program.

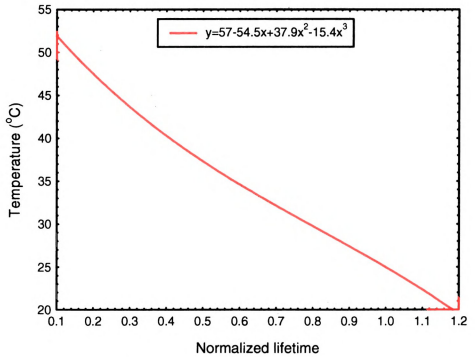

Figure 2. Plot of normalized lifetime

The region of interest in the GUI pertains to the region within the images that correlation is performed. The whole image can be selected but the correlation will take longer to perform. Other input boxes include specifications for delay time between images, scaling factor (pixels/mm), rows to average (temperature measurement only), fitting order for correlation, points for polynomial fit, columns to average (temperature measurement only) and image bit levels. Additional inputs are also needed to specify the locations for file input output. The graphical display on the left illustrates the local polynomial fit along each line of pixel and its corresponding correlation coefficient while the display on the right illustrates the velocity profile measured.

The following illustrations detail the inner workings of the program and are self explanatory by reading the captions.

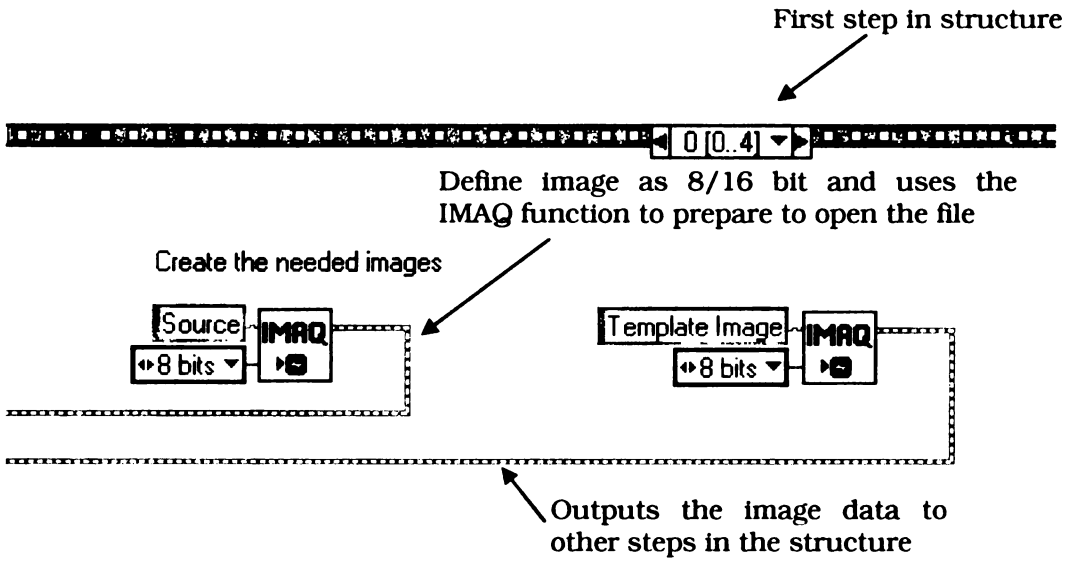

Figure 3. First step in program is to open the images for correlation.

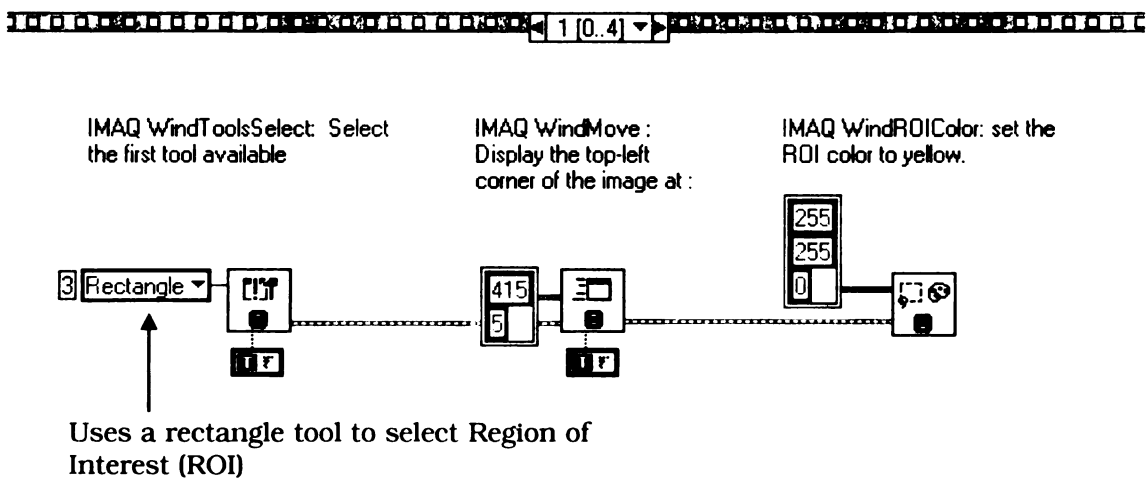

Figure 4. Setup the ROI operator

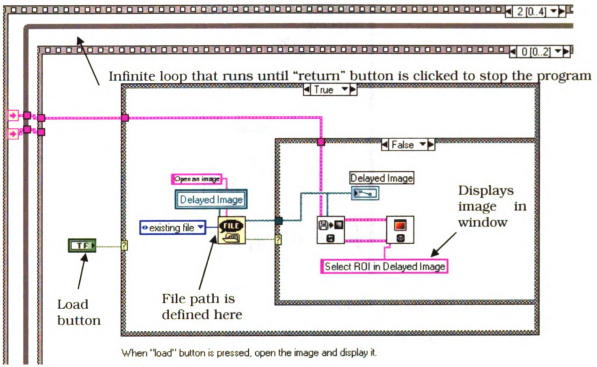

Figure 5. Loading of images and displaying it in window

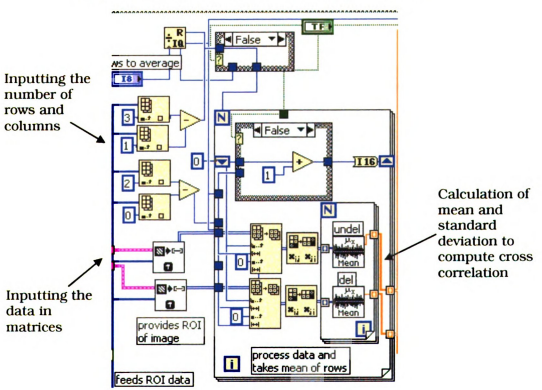

Figure 6. Preparation of the data set and obtain mean of each row

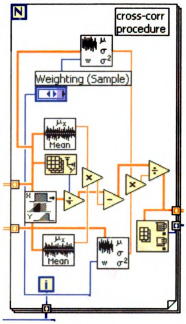

Figure 7. Performs the cross correlation of the data

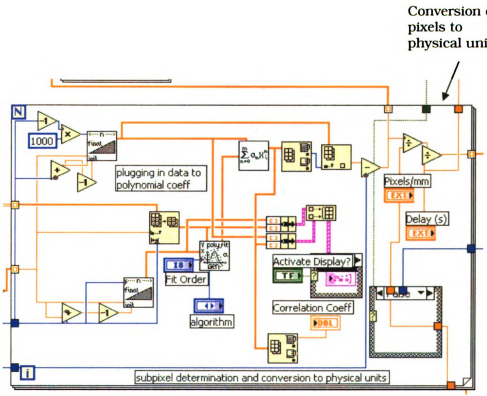

Figure 8. Fits a polynomial around the peak of the cross correlation to obtain sub-pixel accuracy

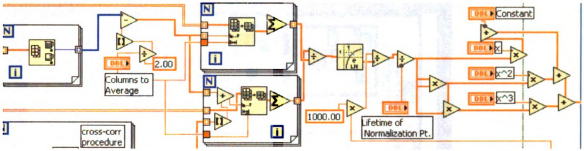

Figure 9.Calculation of temperature profiles

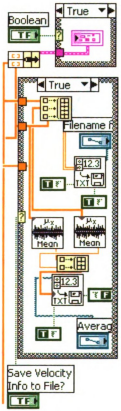

Figure 10. Saves the dataset into text files

Each of the previous figures illustrates a core section of the program without going into details the function of each icon. For completeness, the entire program is illustrated in Figure 11.

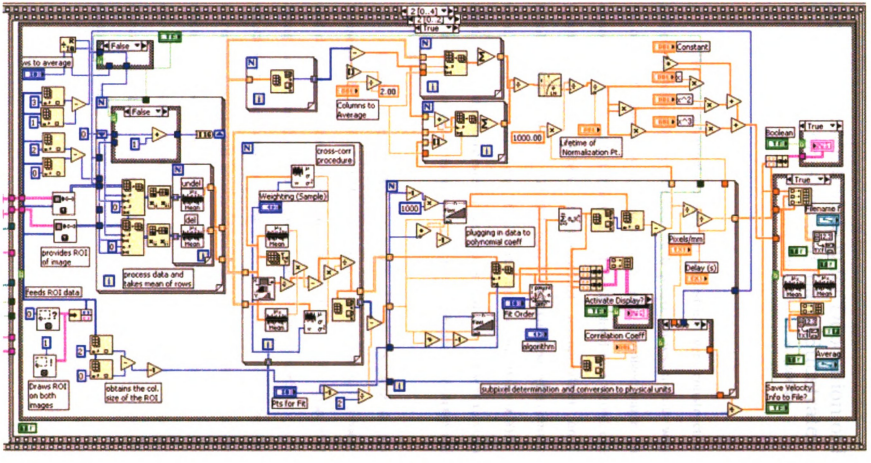

Figure 11. Coding diagram of Single Line Velocity and Temperature Correlation Program

Appendix I: Methodology for Deposition of Polymer-brushes on Quartz Substrates

(adapted from Miller et. al. (2004))

The microchannels utilized in this study were constructed out of quartz flats and coated with polymer brushes. Each quartz flat was initially washed for 1 hour with 1M of NaOH followed by a 5 minute rinse with deionized water. The substrate is then rinsed for 1 hour with 1M of HCl and finally dried in a 110°C oven overnight. Before polymerizing the HEMA (2-hydroxyethyl methacrylate) on the substrate, a trichlorosilane initiator, (11-(2-bromo-2-methyl)propionyloxy)undecyltrichlorosilane is used. A solution containing 10μL of the initiator in 10mL of THF (2μM initiator) was used to rinse the substrate for 5 minutes and then allowed to stand for 18 hours. The substrates were then rinsed with THF for 10 minutes and dried with a flow of nitrogen for 10 minutes.

Before using HEMA, it needs to be prepurified with basic alumina. Subsequently, 10mL of HEMA was added to 10mL of deionized water in a Schlenk flask and degassed via three freeze-pump-thaw cycles. Next, 55mg (0.055milimol) of CuCl, 36mg (0.16milimol) of $CuBr_2$ and 244mg (1.56milimol) of bpy were added to the solution. The flask was then sealed with a septum, purged with nitrogen for 2 minutes to remove oxygen, and sonicated for 5 minutes to yield a homogeneous, dark brown mixture. The substrate is allowed to stand in this mixture for 1 to 12 hours depending on the coating thickness needed and eventually flushed with DMF (2,3-dichlorophenol,*N*,*N*-dimethylformamide) for 2 hours. The figure below illustrates the chemical structure of HEMA

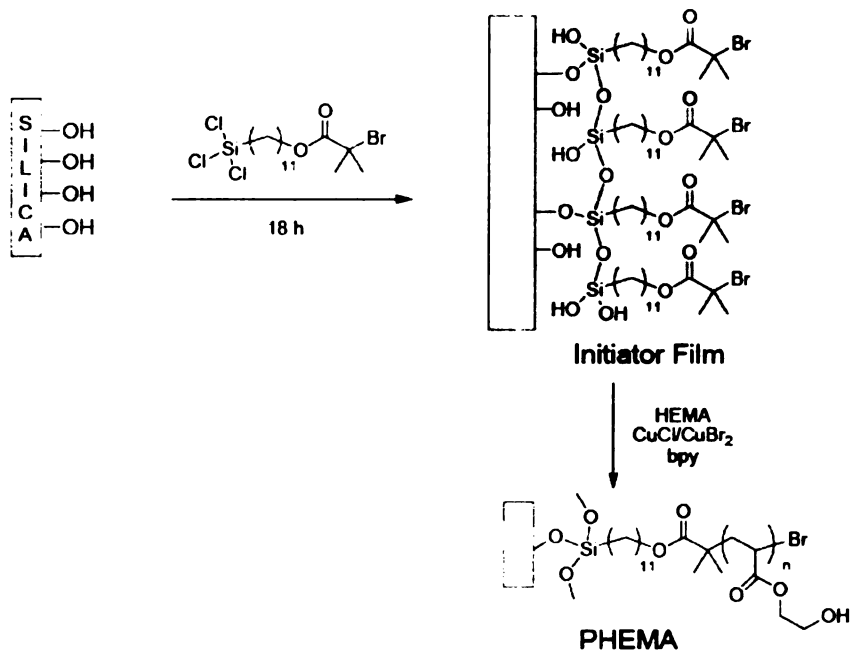

Figure 1. Schematic of the substrate surface initially, after treatment with the initiator and HEMA

Appendix J: Calibration of Phosphorescent Chemicals for Temperature Measurements

Before the phosphorescent chemicals are used to measure the temperature of the fluid, it needs to be calibrated. The calibration relates the lifetime of the chemicals to the temperature of the fluid. To obtain the lifetime of the chemicals, the phosphorescence emission of the chemicals at different times after the laser has fired is imaged. After background subtraction the averaged phosphorescence intensity is plotted. A typical plot of the emission decay is shown in Figure I-1.

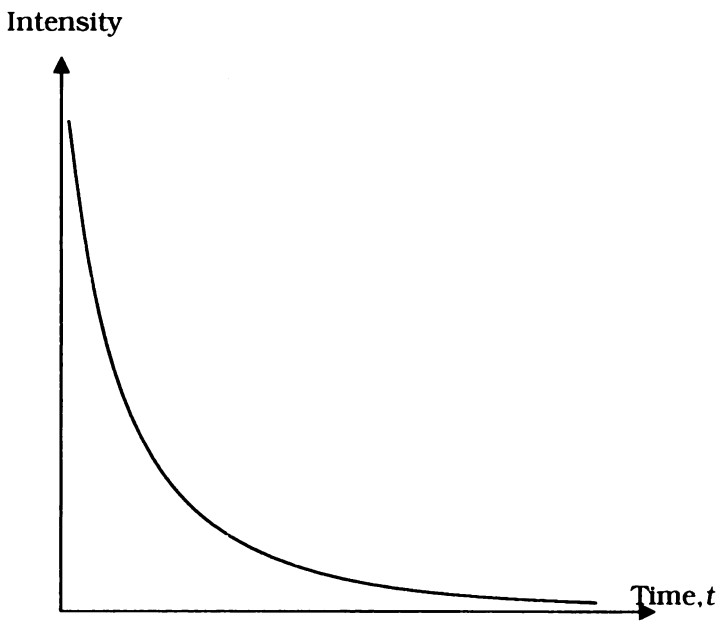

Figure I-1. Typical emission decay of phosphorescent chemicals.

This procedure of obtaining lifetime is repeated across the temperature range of interest and plotted below. The coefficients of the third order fit to the data points are then plugged into the image correlation program for calculation of the temperature.

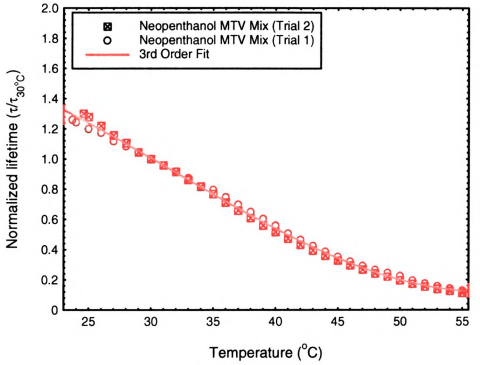

Figure I-2. Normalized lifetime at different temperature for the phosphorescent chemicals

Appendix K: Accuracy in the Temperature Measurements with the MTT technique

The analysis of the accuracy of the temperature measurements with the MTT technique was previously described in Hu and Koochesfahani (2005). The accuracy of the technique is directly influenced by noise in the two phosphorescence signals S_1 and S_2 (refer to Figure 2-23). The actual image noise at each pixel, characterized by the standard deviation of the signal, is much higher and is in the 3% range. This noise level is connected to the CCD depth of well and the intensifier stage of the CCD. The accuracy in calculating the phosphorescence lifetime can be estimated by the following equation.

$$\frac{\sigma_t}{\tau} = \frac{1}{\ln(S_1/S_2)}\sqrt{\left(\frac{\sigma_{S_1}}{S_1}\right)^2 + \left(\frac{\sigma_{S_2}}{S_2}\right)^2}, \qquad (1)$$

This was suggested by Ballew and Demas (1999), where σ_{S_1}, σ_{S_2} *and* σ_τ are the standard deviations of S_1, S_2, and τ, respectively. The 3% phosphorescence signal at each pixel will, therefore, result in a lifetime measurement accuracy of about 4% and an instantaneous temperature error of 0.8°C (using the lifetime temperature sensitivity of 5% per °C at 20°C for reference). Since this error is unbiased, it can be substantially reduced by average over neighboring pixels. Assuming statistical independence, the error can be reduced by the factor $1/\sqrt{N}$, where N is the number of pixels in the interrogation window. For the results given in the present study based on 32x32 pixel interrogation windows, the instantaneous measurement error due to the noise in the phosphorescence images is estimated to be less than 0.1°C.

Appendix L: Equations of Motion with Slip Derivation

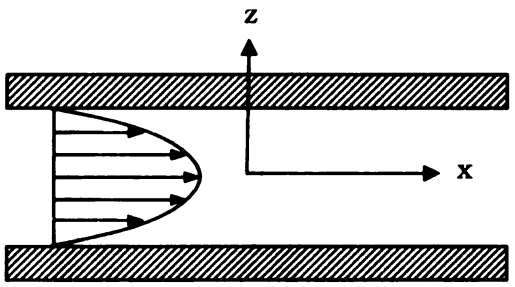

Figure J-1. Coordinate system

The velocity profile with slip in a 2-D geometry is derived. The slip boundary conditions for this flow are:

$$U_{y=h} = -\beta_1 \frac{\partial u}{\partial y}_{y=h}, \; U_{y=-h} = -\beta_2 \frac{\partial u}{\partial y}_{y=-h} \tag{1}$$

$$\begin{aligned} &@\, y = h \\ &-\beta_1 \frac{\partial u}{\partial y}_{y=h} = \frac{1}{2\mu}\frac{\partial p}{\partial x}h^2 + C_1 h + C_2 \\ &@\, y = -h \\ &\beta_2 \frac{\partial u}{\partial y}_{y=-h} = \frac{1}{2\mu}\frac{\partial p}{\partial x}h^2 - C_1 h + C_2 \end{aligned} \tag{2}$$

where β_1 and β_2 are defined as the slip lengths at the walls

Subtracting the two equations above,

$$\begin{aligned} &\beta_2 \frac{\partial u}{\partial y}_{y=-h} + \beta_1 \frac{\partial u}{\partial y}_{y=h} = 2C_1 h \\ &C_1 = -\frac{\beta_2}{2h}\frac{\partial u}{\partial y}_{y=-h} - \frac{\beta_1}{2h}\frac{\partial u}{\partial y}_{y=h} \end{aligned} \tag{3}$$

Adding the two equations together,

$$C_2 = \frac{\beta_2}{2}\frac{\partial u}{\partial y}_{y=-h} - \frac{\beta_1}{2}\frac{\partial u}{\partial y}_{y=h} - \frac{h^2}{2\mu}\frac{\partial p}{\partial x} \tag{4}$$

Again as in the case of a single slip length derivation, the slope needs to be substituted. We know that the slope has the following general expression:

$$\frac{\partial u}{\partial y} = \frac{1}{\mu}\frac{\partial p}{\partial x}y + C_1 \tag{5}$$

substituting the results from above, we obtain

$$\begin{aligned}
\frac{\partial u}{\partial y} &= \frac{1}{\mu}\frac{\partial p}{\partial x}y - \frac{\beta_2}{2h}\frac{\partial u}{\partial y}_{y=-h} - \frac{\beta_1}{2h}\frac{\partial u}{\partial y}_{y=h} \\
\frac{\partial u}{\partial y}_{y=h} &= \frac{1}{\mu}\frac{\partial p}{\partial x}h - \frac{\beta_2}{2h}\frac{\partial u}{\partial y}_{y=-h} - \frac{\beta_1}{2h}\frac{\partial u}{\partial y}_{y=h}
\end{aligned} \tag{6}$$

consolidating the terms,

$$\begin{aligned}
\left(1+\frac{\beta_1}{2h}\right)\frac{\partial u}{\partial y}_{y=h} &= \frac{h}{\mu}\frac{\partial p}{\partial x} - \frac{\beta_2}{2h}\frac{\partial u}{\partial y}_{y=-h} \\
\frac{\partial u}{\partial y}_{y=h} &= \frac{2h^2}{\mu(2h+\beta_1)}\frac{\partial p}{\partial x} - \frac{\beta_2}{2h+\beta_1}\frac{\partial u}{\partial y}_{y=-h} \\
\left(1+\frac{\beta_2}{2h}\right)\frac{\partial u}{\partial y}_{y=-h} &= -\frac{h}{\mu}\frac{\partial p}{\partial x} - \frac{\beta_1}{2h}\frac{\partial u}{\partial y}_{y=h} \\
\frac{\partial u}{\partial y}_{y=-h} &= \frac{2h^2}{\mu(2h+\beta_2)}\frac{\partial p}{\partial x} - \frac{\beta_1}{2h+\beta_2}\frac{\partial u}{\partial y}_{y=h}
\end{aligned} \tag{7}$$

substituting into the equation for slope at y=h with the equation for slope at y=-h, the following expression results:

$$\begin{aligned}
\frac{\partial u}{\partial y}_{y=h} &= \frac{2h^2}{(2h+\beta_1)}\frac{\partial p}{\partial x} - \frac{\beta_2}{2h+\beta_1}\left[\frac{-2h^2}{(2h+2\beta_2)\mu}\frac{\partial p}{\partial x} - \frac{\beta_1}{2h+\beta_2}\frac{\partial u}{\partial y}_{y=h}\right] \\
\left[1-\frac{\beta_1\beta_2}{(2h+\beta_1)(2h+\beta_2)}\right]\frac{\partial u}{\partial y}_{y=h} &= \frac{2h^2}{(2h+\beta_1)\mu}\frac{\partial p}{\partial x} + \frac{\beta_2}{2h+\beta_1}\left(\frac{2h^2}{(2h+\beta_2)\mu}\frac{\partial p}{\partial x}\right) \\
\frac{4h^2+2h\beta_2+2h\beta_1}{(2h+\beta_1)(2h+\beta_2)}\left(\frac{\partial u}{\partial y}\right)_{y=h} &= \frac{2h^2}{(2h+\beta_1)\mu}\frac{\partial p}{\partial x}\left[1+\frac{\beta_2}{2h+\beta_2}\right] \\
\left(\frac{\partial u}{\partial y}\right)_{y=h} &= \frac{2h^2(2h+\beta_2)}{\mu\left(4h^2+2h\beta_2+2h\beta_1\right)}\left(\frac{\partial p}{\partial x}\right) - \frac{2h^2\beta_2}{4h^2+2h\beta_2+2h\beta_1}\left(\frac{\partial p}{\partial x}\right) \\
\left(\frac{\partial u}{\partial y}\right)_{y=h} &= \frac{2h^2(2h+\beta_2)}{\mu\left(4h^2+2h\beta_2+2h\beta_1\right)}\left(\frac{\partial p}{\partial x}\right)\left[1+\frac{\beta_2}{2h+\beta_2}\right]
\end{aligned} \tag{8}$$

similarly, the slope at y=-h needs to be expressed in terms of the pressure gradient:

$$\frac{\partial u}{\partial y}_{y=-h} = \frac{-2h^2}{(2h+\beta_2)\mu}\frac{\partial p}{\partial x} - \frac{\beta_1}{2h+\beta_2}\left(\frac{2h^2(2h+\beta_2)}{\mu\left(4h^2+2h\beta_2+2h\beta_1\right)}\left(\frac{\partial p}{\partial x}\right)\left[1+\frac{\beta_2}{2h+\beta_2}\right]\right)$$

$$\frac{\partial u}{\partial y}_{y=-h} = \frac{-2h^2}{(2h+\beta_2)\mu}\frac{\partial p}{\partial x}\left[1+\frac{\beta_1(2h+2\beta_2)}{4h^2+2h\beta_2+2h\beta_1}\right] \qquad (9)$$

$$\frac{\partial u}{\partial y}_{y=-h} = \frac{-2h^2(2h+2\beta_1)}{\mu\left(4h^2+2h\beta_2+2h\beta_1\right)}\frac{\partial p}{\partial x}$$

substituting the values for slope at the walls into the general equation describing the flow velocity, U,

$$U(y) = \frac{1}{2\mu}\frac{\partial p}{\partial x}y^2 - \frac{\beta_2 y}{2h}\frac{\partial u}{\partial y}_{y=-h} - \frac{\beta_1 y}{2h}\frac{\partial u}{\partial y}_{y=h} + \frac{\beta_2}{2}\frac{\partial u}{\partial y}_{y=-h} - \frac{\beta_1}{2}\frac{\partial u}{\partial y}_{y=h} - \frac{h^2}{2\mu}\frac{\partial p}{\partial x}$$

$$U(y) = \frac{y^2}{2\mu}\frac{\partial p}{\partial x} - \frac{\beta_2 y}{2h}\left[\frac{-2h^2(2h+2\beta_1)}{\mu\left(4h^2+2h\beta_2+2h\beta_1\right)}\frac{\partial p}{\partial x}\right] - \frac{\beta_1 y}{2h}\left[\frac{2h^2(2h+\beta_2)}{\mu\left(4h^2+2h\beta_2+2h\beta_1\right)}\frac{\partial p}{\partial x}\left(1+\frac{\beta_2}{2h+\beta_2}\right)\right] \qquad (10)$$

$$-\frac{\beta_1}{2}\left[\frac{2h^2(2h+\beta_2)}{\mu\left(4h^2+2h\beta_2+2h\beta_1\right)}\frac{\partial p}{\partial x}\left(1+\frac{\beta_2}{2h+\beta_2}\right)\right] + \frac{\beta_2}{2}\left[\frac{-2h^2(2h+2\beta_1)}{\mu\left(4h^2+2h\beta_2+2h\beta_1\right)}\frac{\partial p}{\partial x}\right] - \frac{h^2}{2\mu}\frac{\partial p}{\partial x}$$

simplifying, the following expression results:

$$U(y) = \frac{y^2}{2\mu}\frac{\partial p}{\partial x} + \frac{2h^2}{\mu\left(4h^2+2h\beta_2+2h\beta_1\right)}\frac{\partial p}{\partial x}\left[(\beta_2-\beta_1)y - h(\beta_1+\beta_2) - 2\beta_1\beta_2\right] - \frac{h^2}{2\mu}\frac{\partial p}{\partial x} \qquad (11)$$

For verification, we test the equation above for the conditions when the slip length is zero or if the slip lengths are the same. For zero slip length, it is obvious that the following expression results:

$$U(y) = \frac{y^2}{2\mu}\frac{\partial p}{\partial x} - \frac{h^2}{2\mu}\frac{\partial p}{\partial x} \qquad (12)$$

for same slip lengths,

$$U(y) = \frac{y^2}{2\mu}\frac{\partial p}{\partial x} + \frac{2h^2}{\mu\left(4h^2 + 4h\beta\right)}\frac{\partial p}{\partial x}\left[-2h\beta - 2\beta^2\right] - \frac{h^2}{2\mu}\frac{\partial p}{\partial x} \tag{13}$$

$$U(y) = \frac{h^2}{2\mu}\frac{\partial p}{\partial x}\left(\frac{y^2}{h^2} - 1 - \frac{2\beta}{h}\right)$$

$$U(y) = \underbrace{\frac{h^2}{2\mu}\left(-\frac{\partial p}{\partial x}\right)\left(1 - \left(\frac{y}{h}\right)^2\right.}_{\text{Standard solution within 2-D channel}} \underbrace{\left. + \frac{2\beta}{h}\right)}_{\text{Slip velocity}} \tag{14}$$

Appendix M: Error Analysis for Pressure Driven Flows

This section of the appendix detail the uncertainties associated with determination of the friction factor. The equation used to calculate the normalized friction factor is repeated here

$$\frac{C_{f,\exp}}{C_{f,theory}} = \frac{2\bar{u}_{theory}}{\bar{u}^2_{\exp}}\left(\frac{\partial u}{\partial z}\right)_{\exp}\left[\frac{\sum_{i=1,3,5..}^{\infty}(-1)^{(i-1)/2}\left(b-\frac{2a\sinh(i\pi b/2a)}{i\pi}\right)\frac{\cos(i\pi y/2a)}{i^3}}{\left(\sum_{i=1,3,5...}^{\infty}(-1)^{(i-1)/2}\left[\tanh(i\pi b/2a)*\frac{i\pi}{2a}\right]\frac{\cos(i\pi y/2a)}{i^3}\right)}\right] \quad (1)$$

The terms within the square brackets in equation (1) only depend on the half height, b, the half width, a, and the particular location along the y-axis, y. The determination of the half height, b, will be discussed later when the uncertainties in the slope $\partial u/\partial z$ is discussed. For the half width, a, the relative error (compared to the width dimension) in determining its dimensions is small due to the use of a high aspect ratio microchannel and is neglected in this analysis. The uncertainties in determining the interrogation location along the y-axis is also neglected as **Error! Reference source not found.** and **Error! Reference source not found.** demonstrated that the changes in velocity and the velocity gradient at the wall is minimal in the center of the channel. All the experiments in this study were conducted away from the wall so that this applies. Thus the errors in determining the normalized friction factor reduce to the errors in measuring the mean velocity and the velocity gradient at the wall.

The uncertainty in the mean velocity propagates from the uncertainty in determining the velocity from the correlation program. **Error! Reference source not found.** illustrates the uncertainty (95% confidence, 2σ). For the typical image pairs used for correlation in this study, a 0.1pixel uncertainty in the velocity is assumed. The determination of the errors in the slope, however, is more involved. The uncertainty in the fit and the determination of the wall location both contribute to it. Figure 1 illustrates the velocity data points

obtained from the correlation of typical image pair. The 2nd order fit to the velocity data points is illustrated as a red continuous curve. The errors in this fit is analyzed below.

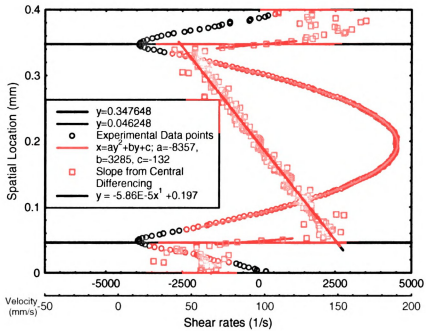

Figure 1. Central-differencing procedure for determining slope at the wall

The method used here for determining the uncertainty in the fit is described in the book "Data Reduction and Error Analysis for The Physical Sciences", by Bevington and Robinson (2nd Ed.) on page 125. The 2nd order fit equation is described in equation (2).

$$u_x = ax^2 + bx + c \qquad (2)$$

The uncertainty in the calculated value of u_x results from the uncertainty in the coefficients of the fit. This is given by the following equation.

$$\sigma_{u_x}^2 = \left(\frac{\partial u_x}{\partial a}\sigma_a\right)^2 + \left(\frac{\partial u_x}{\partial b}\sigma_b\right)^2 + \left(\frac{\partial u_x}{\partial c}\sigma_c\right)^2 + 2\left(\frac{\partial u_x}{\partial a}\frac{\partial u_x}{\partial b}\sigma_{ab}\right)^2$$
$$+ 2\left(\frac{\partial u_x}{\partial a}\frac{\partial u_x}{\partial c}\sigma_{ac}\right)^2 + 2\left(\frac{\partial u_x}{\partial c}\frac{\partial u_x}{\partial b}\sigma_{cb}\right)^2 \qquad (3)$$
$$\sigma_{u_x}^2 = \varepsilon_{11} + x^2\varepsilon_{22} + x^4\varepsilon_{33} + 2(x\varepsilon_{12} + x^2\varepsilon_{13} + x^3\varepsilon_{23})$$

where $\sigma_{u_x}, \sigma_a, \sigma_b, \sigma_c$ are the uncertainties in determining the velocity and the parameters *a*, *b* and *c* respectively. The ε terms in the equation are the terms in the error matrix. The error matrix was obtained from the matrix inverse of the symmetric matrix, *a* which is defined as follow

$$\alpha_{lk} = \sum\left[\frac{1}{\sigma_l^2} f_l(x_l) f_k(x_l)\right] \qquad (4)$$

for a quadratic fit to the data set, we have 3 terms. The *f* terms in the above equation resolves to the following:

$$f_1(x_l) = 1$$
$$f_2(x_l) = x_l \qquad (5)$$
$$f_3(x_l) = x_l^2$$

and the *a* matrix was computed for a typical data set.

$$\alpha_{11} = \sum\frac{1}{(0.1)^2} = 15500$$
$$\alpha_{12} = \sum\left(\frac{x_l}{\sigma_l^2}\right) = 2831.4 = \alpha_{21}$$
$$\alpha_{13} = \sum\left(\frac{x_l^2}{\sigma_l^2}\right) = 635.7728 = \alpha_{31} = \alpha_{22} \qquad (6)$$
$$\alpha_{33} = \sum\left(\frac{x_l^4}{\sigma_l^2}\right) = 42.51779$$

by taking the inverse of this matrix, we obtain the error matrix. The error matrix is shown below:

ε	1	2	3
1	0.0012	-0.0138	0.0336
2	-0.0138	0.1834	-0.4810
3	0.0336	-0.4810	1.3224

These values are plugged into the equation for σ_{u_x} and the uncertainty of the 2nd order fit is obtained. The other contribution to the uncertainty is the error in the determination of the wall locations. From Figure 1, a blue curve was fitted to the central-differenced data points near the walls. A linear curve fit was used to determine the intersection of the data points with the location of zero shear rate. This would yield the location of the wall. The uncertainty in fitting this linear fit would contribute to the uncertainties in the measurement of the friction factor. A similar analysis as was performed before for the 2nd order fit was done here to determine the uncertainties of the linear fit. The combination of the three uncertainties adds up to give the overall uncertainty associated with the determination of the friction factor, C_f. σ_{2nd}, σ_{1st} and $\sigma_{\bar{u}}$ are the uncertainties associated with the 2nd order fit, the linear fit and the determination of the mean velocity respectively.

$$\sigma_C = \sqrt{\sigma_{2nd} + \sigma_{1st} + \sigma_{\bar{u}}} \tag{7}$$

The errors for all the friction factor measurements were calculated and shown in the last column of the tables of results (Table 3-1Table 3-2, Table **3-3**Table 3-4).

Appendix N: Determination of the Slip Detection Limit

The friction factor analysis shown in the main body of this thesis showed an excellent agreement with classical theory. In this section of the appendices, the average difference between the experimental friction factor and theory is used to investigate the possibility of determining the slip length. This is done by attributing the average uncertainty to be solely caused by the errors in the fit to the data points in Figure L-1.

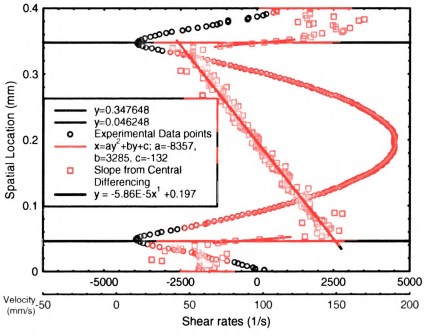

Figure L-1. Central differencing procedure for determining friction factor.

The linear fit to the central-differenced data points (red) is investigated. The equation for linear curve fit is

$$y = -5.86 * 10^{-5} x + 0.197 \tag{1}$$

by plugging in the upper wall location, the slope at the wall is determined.

$$x = \frac{0.34765mm - 0.197}{-5.86 * 10^{-5}} = -2570.819 \tag{2}$$

If the ± 0.5% uncertainty in friction factor is attributed entirely to the determination of the slope, 0.5% of the slope determined at the wall would be 12.85. At a slope of (-2570.819+12.85), the spatial location is determined to be 346.9μm.

$$y = -5.86 * 10^{-5} * (-2557.965) + 0.197 = 346.9\mu m \tag{3}$$

The wall is located at 347.7μm. By substituting the two spatial locations into the parabolic curve fit equation, the corresponding velocity can be determined. For the 0.347648mm spatial location, the calculated velocity is identically zero. The velocity at the second spatial location is calculated as follows

$$x = -8357(0.346897)^2 + 3285\,(0.346897) - 132 = 1.8973 mm/s \tag{4}$$

Thus the 0.5% uncertainty in friction factor translates to a 1.8973mm/s velocity uncertainty at the wall for this particular case. To determine the slip length, the following equation is used.

$$U(y) = \frac{h^2}{2\mu}\left(-\frac{\partial p}{\partial x}\right)\left(1 - \left(\frac{y}{h}\right)^2 + \frac{2\beta}{h}\right) \tag{5}$$

At the wall, y = h and the first two terms cancel out. This results in the following equation.

$$U(h) = \frac{\beta h}{\mu}\left(-\frac{\partial p}{\partial x}\right) \tag{6}$$

From the numerical simulation of pressure driven flow within a 301.4μm X 25.4mm microchannel, the pressure drop would be 14,747.49 N/m^3. Substituting this into the equation,

$$\beta = \frac{U(h)\mu}{h\left(-\frac{\partial p}{\partial x}\right)} = \frac{1.8973 * 10^{-3} * 0.00088}{0.1507 * 10^{-3}(14{,}747.49)} = 752nm \tag{7}$$

Thus, the slip length has to be more than 752nm to be detected.

Appendix O: Derivation of Equations for Molecular Tagging Thermometry

The basis of the Molecular Tagging Thermometry technique is the dependence of the decay rate of phosphorescence emission of photoluminescent chemicals on temperature. The total phosphorescence emission is generally described by the following equation.

$$I_p = I_i C \varepsilon \Phi_p \tag{1}$$

where I_p is the total phosphorescence intensity, I_i is the total incident intensity (which in this case would be the laser excitation), C is the concentration of the photoluminescent chemical, ε is the absorption coefficient and Φ_p is the phosphorescence quantum efficiency. For all practical purposes, however, the concentration, absorption coefficient and phosphorescence quantum efficiency is unknown. To circumvent this problem of unknowns, a ratiometric method is developed to avoid the use of these unknowns to determine the lifetime of the chemicals.

Lifetime, τ, which is defined as the 1/e decay rate of phosphorescence emission can be expressed with regards to the initial intensity, I_i by the following equation.

$$I_{em} = I_i e^{-t/\tau} \tag{2}$$

where I_{em} refers to the intensity emission at a particular instance of time, t, after initial excitation of the photoluminescent molecules. To physically image this emission, a gated intensified camera is used. Since the camera is exposed to the phosphorescence emission for a finite time, equation2 can be integrated over a gate period, δt, to yield equation 3.

$$I_{em,\delta t} = \int_{t_o}^{t_o+\delta t} I_i e^{-t/\tau} dt \tag{3}$$

The equations presented so far can be shown to yield equation E.4.

$$I_{em,\delta t} = I_i C \varepsilon \Phi p\left(1 - e^{-\delta t/\tau}\right) e^{-t/\tau} \tag{4}$$

The ratiometric method involves the ratio of the integrated intensity at two time periods as per equation 4. For the same gate or exposure time, the ratio of the two intensities reduce to equation 5 since the initial excitation intensity, I_i, concentration, C, absorption coefficient, ε, and the quantum efficiency, Φ all remains the same.

$$\frac{I_{em,1}}{I_{em,2}} = e^{-\frac{\Delta t}{\tau}} \tag{5}$$

This illustrates that by dividing the intensity of the first image with the intensity from the second image on a pixel by pixel basis, the lifetime of the phosphorescence emission can be obtained as long as the time delay (Δt) between the two images is known.

However, the phosphorescence emission in the second image is usually much lower and the constraint of the same exposure time with the initial image is sometimes not met. The equation is rederived for the case where the exposure times are different.

$$\frac{I_{em,1}}{I_{em,2}} = \frac{\left(1 - e^{-\delta t_1/\tau}\right) e^{-t_1/\tau}}{\left(1 - e^{-\delta t_2/\tau}\right) e^{-t_2/\tau}} = \frac{\left(1 - e^{-\delta t_1/\tau}\right)}{\left(1 - e^{-\delta t_2/\tau}\right)} e^{-\frac{\Delta t}{\tau}} \tag{6}$$

To relate lifetime to temperature, a calibration is initially performed on the photoluminescent chemicals in a range of temperature to obtain the respective lifetimes at different temperatures. Normalized at room temperature, the dataset proved

consistently reproducible thus enabling the calibration to be done only once for each type of photoluminescent chemical.

Appendix P: User Defined Functions (UDF)

The following UDFs were written to specify a varying inlet velocity and a transient heat source in FLUENT. The inlet velocity is varying with time due to the increase in conductivity of the fluid as temperature rises. The rising heat source is also a direct consequence of a change in conductivity.

(a) Transient Velocity Magnitude:

```
DEFINE_PROFILE (ramp_velocity, thread, position)
{
face_t f;
real t = CURRENT_TIME;
begin_f_loop(f, thread)
        {
        F_PROFILE(f, thread, position) = 0.00175 + (0.00453614/30)*t;
        }
end_f_loop(f, thread)
```

(b) Transient Heat Source:

```
DEFINE_SOURCE (q_source, cell, thread, dS, eqn)
{
real source;
real t = CURRENT_TIME;
source = 2*10^7 + (0.44395*10^7/30)*t;
dS [eqn] = (0.44395*10^7/30);
return source;
}
```

Bibliography

Adamson, A., Gast, A., "Physical chemistry of surfaces," *Wiley*, 1997.

Ballew, R., and Demas, J., "An error analysis of the rapid lifetime determination method for the evaluation of single exponential decay," *Anal. Chem.*, 61, pp. 30-33, 1999.

Bohl, D., and Koochesfahani, M., and Olson, B., "Development of stereoscopic Molecular Tagging Velocimetry," *Experiments in Fluids*, 30, pp. 302-308, 2001.

Biddiss, E., Erickson, D., Li, D., "Heterogeneous surface charge enhanced micromixing for electrokinetic flows," *Anal. Chem.*, 76, pp. 3208-3212, 2004.

Bikerman, J., *Z. Physik. Chem.* A163, (1933) 378; Kolloid-Z. 72 (1935) 100.

Brutin, D., and Tadrist, L., "Experimental friction factor of a liquid flow in microtubes," *Physics of Fluids*, 15 (3), 2003.

Choi, S.B., Barron, R.F., and Warrington, R.O. (1991) "Fluid flow and heat transfer in microtubes," in DSC-Vol 32, *Micromechanical Sensors, Actuators and Systems*, ASME Winter Annual Meeting, Atlanta, GA, pp. 123-134.

Dabek-Zlotorzynska, E., Piechowski, M., Mcgrath, M., Lai, E., "Determination of low-molecular-mass carboxylic acids in atmospheric aerosol and vehicle emission samples by capillary electrophoresis," *Journal of Chromatography A*, 910, pp. 331-345, 2001.

Erickson, D., Li, D., Werner, C., "An improved method of determining the ζ-potential and surface conductance," Journal of Colloid and Interface Science, 232, pp. 186-197, 2000.

Faller, T., Engelhardt, H., "How to achieve higher repeatability and reproducibility in capillary electrophoresis," *Journal of Chromatography A*, 853, pp. 83-94, 1999.

Furusawa, K., Sasaki, H., Nashima, T., "Electroosmosis and streaming potential measurements," *Surfactant Science Series: Electrical Phenomena at Interfaces*, 76, pp. 225-243, Marcel-Dekker, 1998.

Gendrich, C. P., "Dynamic stall of rapidly pitching airfoils: MTV experiments and Navier Stokes simulations," *phD. Thesis* (1998).

Gendrich, C.P., and Koochesfahani, M.M., "A Spatial Correlation Technique for Estimating Velocity Fields Using Molecular Tagging Velocimetry (MTV)", *Experiments in Fluids*, 22, pp. 67-77, 1996.

Gendrich, C.P., Koochesfahani, M.M., and Nocera, D.G., "Molecular Tagging Velocimetry and Other Novel Applications of a New Phosphorescent Supramolecule", *Experiments in Fluids*, 23, pp. 361-372, 1997.

Grossman, P. D., and D. S. Soane, " Orientation effects on the electrophoretic mobility of rod-shaped molecules in free solution," *Anal. Chem.* **62:**1592-1596, 1990.

Grushka, E., McCormick, R., Kirkland, J., "Effects of temperature gradients on the efficiency of capillary zone electrophoresis separations," *Anal. Chem.* 61 pp. 241-246,

1989.

Hau, W., Trau, D., Sucher, N., Wong, M., Zohar, Y., "Surface chemistry technology for microfluidics", *Journal of Micromechanics and Microengineering*, 13, pp. 272-278, 2003.

Herr, A., Molho, J., Santiago, J., Mungal, M., Kenny, T., "Electroosmotic capillary flow with non uniform zeta potential," *Anal. Chem.*, 72, pp. 1053-1057, 2000.

Hu, H., Koochesfahani, M., "A novel technique for quantitative temperature mapping in liquid by measuring lifetime of laser induced phosphorescence," *Journal of Visualization*, 6(2), pp. 143-153, 2003.

Hu, H., Koochesfahani, M., "Molecular Tagging Velocimetry and Thermometry and its Application to the Wake of a Heated Circular Cylinder," *Meas. Sci. Technol.*, 2005 (accepted for publication).

Huang, W., Kim, J., Bruening, M., Baker, G., "Functionalization of surfaces by water-accelerated atom-transfer radical polymerization of hydroxyethyl methacrylate and subsequent derivation," *Macromolecules*, 35, pp. 1175-1179, 2002.

Hunter, R.J., "Zeta Potential in Colloidal Science," Academic, New York, 1981.

Incropera, F., Dewitt, D., "Introduction to Heat Transfer," Wiley Publishing, New York, 1996.

Ivkov, R., Butler, P., Satija, S., "Effect of solvent flow on a polymer brush: a neutron reflectivity study of the brush height and chain density profile," *Langmuir*, 17, pp. 2999-3005, 2001.

Jabbarzadeh, A., Atkinson, J., Tanner, R. "Wall slip in the molecular dynamics simulation of thin films of hexadecane," *The Journal of Chemical Physics*, 110 (5), pp. 2612-2620.

Jiang, X., Zhou, Z., Yao, J., Li, Y., and Ye, X., "Micro fluid flow in microchannel," in *Transducers* '95: Eurosensor IX, 8th Int. Conf. on Solid state sensors and actuators and eurosensors IX, Sweden, pp. 317-320, 1995.

Kim, J., Bruening, M., Baker, G., "Surface-initiated atom transfer radical polymerization on gold at ambient temperature," *J., Am. Chem. Soc.*, 122, pp. 7616-7617, 2000.

Koochesfahani, M.M., Cohn, R.K., Gendrich, C.P., Nocera, D.G., "Molecular Tagging Diagnostics for the Study of Kinematics and Mixing in Liquid Phase Flows", *Proceeding of the Eight International Symposium on Applications of Laser techniques in Fluid Mechanics*, Lisbon, Portugal, July 8-11, 1996.

Lauer, H. H., and D. McManigill. 1986. Capillary zone electrophoresis of proteins in untreated fused silica tubing. Anal. Chem. 58:166

Lum, C., Koochesfahani, M., and McGrath, J., "Measurements of the velocity field with MTV during the solidification of an alloy analog with mushy region," ASME/IMECE2001 Paper No. HTD-24222, 2001.

Lyklema, J., "Fundamentals of Interface and Colloid Science, Volume II: Solid-Liquid Interfaces," Academic Press, 1995.

Maynes, D., Webb, A., "Velocity profile characterization in sub-millimeter diameter tubes using molecular tagging velocimetry," *Experiments in Fluids*, 32, pp. 3-15, 2002.

Miles, R., Grinstead, J., Kohl, R., Diskin, G., "The RELIEF Flow Tagging Technique and its Application in Engine Testing Facilities and for Helium-air Mixing Studies," *Meas. Sci. Technol.*, 2000, 11, 1272.

Minor, M., van der Linde, A., van Leeuwen, H., Lyklema, "Dynamic Aspects of Electrophoresis and Electroosmosis: A New Fast Method for Measuring Particle Mobilities," J., Journal of Colloid Interface Science, 189, 1997, 370-375.

Navier, C.L.M.H., *Mem. Acad. R. Sci. Inst. France* 1, 414, 1823.

Ohshima & Furusawa, "Electrical Phenomena at Interfaces: Fundamentals, Measurements and Applications", *Surfactant Science Series*, 76 Second Edition, Marcel Dekker AG, 1998.

Overbeek, J. T. G., "Colloid Science," Elsevier, Amsterdam, 1952.
Pfahler, J., Harley, J., Bau, H., and Zemel, J., "Liquid transport in micron and submicron channels", *Sensors and Actuators A*, 21-A23, pp. 431-434, 1990a.

Phares, D., and Smedley, G., "A study of laminar flow of polar fluids through circular microtubes," *Physics of Fluids*, 16(5), pp. 1267-1272.

Pit, R., Hervet, H. Léger, "Direct Experimental Evidence of Slip in Hexadecane: Solid Interfaces" *Phys. Rev. Letters*, 85(5) pp. 980-983, 2000.

Probstein, R., "Physicochemical Hydrodynamics: An Introduction", Second Edition, *Wile Interscience Publication*, 1994.

Raber, G., Greschonig, "New preconditioning strategy for the determination of inorganic anions with capillary zone electrophoresis using indirect UV detection," *Journal of Chromatography A*, 890, pp. 355-361, 2000.

Ren, L., Qu, W., Li, D., "Interfacial electrokinetic effects on liquid flow in microchannels," *Int. Journal of Heat and Mass Transfer*, 44, pp. 3125-3134.

Rice, C.L., Whitehead, R., "Electrokinetic flow in a narrow cylindrical capillary," *J. Phys. Chem*, 69, p. 4017, 1965.

Ross, D., Gaitan, M., Locascio, L., "Temperature measurement in microfluidic system using a temperature-dependent fluorescent dye," *Anal. Chem.*, **73**, pp. 4117-4123, 2001.

Shah, R. K. and London, A. L., "Laminar Flow Forced Convection in Ducts: a Source Book for Compact Heat Exchanger Analytical Data", 1978, Academic Press, New York.

Sharp, K., Adrian, R., Santiago, J., Molho, J., "Liquid Flows in Microchannels", *MEMS Handbook*, CRC Press, 2002.

Sharp, K., Adrian, R., Beebe, D., "Anomalous transition to turbulence in microtubes," *Proc. Int. Mech. Eng. Cong. Expo, 5th Micro-Fluidic Symp., Nov 5-10 2000.*

Sze, A., Erickson, D., Ren, L., Li, R., "Zeta potential measurement using the Smoluchowski equation and the slope of the current-time relationship in electroosmotic

flow," *Journal of Colloid and Interface Science*, 261, pp. 402-410, 2003.

Skoog, D., West, D., and Holler, F., "Fundamentals of Analytical Chemistry," 7th Edition, Saunders College Publishing, 1997.

Stroock, A., Weck, M., Chiu, D., Huck, W., Kenis, P., Ismagilov, R. and Whitesides, G., "Patterning electroosmotic flow with patterned surface charge," *Physical Review Letters*, 84, 15, pp. 3314-3317, 2000.

Thomson, S., Maynes, D., "Spatially resolved temperature measurement in a liquid using laser induced phosphorescence," *Journal of Fluid Engineering*, 123 pp. 293-302, 2001.

Tretheway, D., Meinhart, C., "Apparent fluid slip at hydrophobic microchannel walls", *Physics of Fluids*, **14**(3), 2002.

White, F. "Viscous Fluid Flow", *Mcgraw-Hill*, 2nd Edition, 1991.

Wilding, P., Pfahler, J., Bau, H., Zemel, J., and Kricka, L., "Manipulation and flow of biological fluids in straight channels micromachined in silicon," *Clin. Chem.* 40, pp. 43-47, 1994.

Wu, P. and Little, W.A., "Measurement of friction factors for the flow of gasses in very fine channels used for micro miniature Joule-Thompson refrigerators", *Cryogenics* 23, pp. 273-277, 1983.

Wyman, J., "Measurement of the dielectric constants of conducting media," *Phys. Rev.*, **35**, pp. 623-634, 1930.

Yu, D., Warrington, R., Barron, R., and Ameel, T., "An experimental and theoretical investigation of fluid flow and heat transfer in microtubes," in Proc. Of ASME/JSME Thermal Engineering Joint Conf., March 19-24, Maui, HI, pp. 523-530, 1995.